Enhancing Heat Transfer in the Developing Thermal Field in a Fluid Saturated Porous Filled Duct with Local Thermal Non-equilibrium

A THESIS SUBMITTED TO
NATIONAL INSTITUTE OF TECHNOLOGY WARANGAL, (T.S.)
FOR THE AWARD OF THE DEGREE OF

DOCTOR OF PHILOSOPHY

IN

MATHEMATICS

BY

NITISH GUPTA

(ROLL NO: 719094)

UNDER THE SUPERVISION OF

Dr. D. BHARGAVI

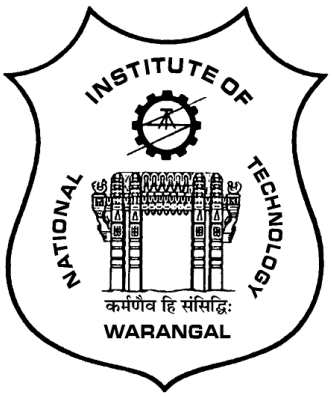

DEPARTMENT OF MATHEMATICS

NATIONAL INSTITUTE OF TECHNOLOGY

WARANGAL - 506004 INDIA

JANUARY, 2024

CERTIFICATE

This is to certify that the thesis entitled "**Enhancing Heat Transfer in the Developing Thermal Field in a Fluid Saturated Porous Filled Duct with Local Thermal Non-equilibrium**", submitted to the National Institute of Technology Warangal, India, for the award of the degree of ***Doctor of Philosophy***, is the bonafide research work done by **Mr. NITISH GUPTA** (ROLL NO: 719094) under my supervision. The contents of this thesis have not been submitted elsewhere for the award of any degree.

Dr. D. Bhargavi
(Supervisor)
Associate Professor
Department of Mathematics
National Institute of Technology, Warangal
Telangana State, INDIA - 506004.

Date: 22-01-2024
Place: NIT Warangal

DECLARATION

This is to certify that the work presented in the thesis entitled "**Enhancing Heat Transfer in the Developing Thermal Field in a Fluid Saturated Porous Filled Duct with Local Thermal Non-equilibrium**", is a bonafide work done by me under the supervision of **Dr. D. Bhargavi** and has not been submitted elsewhere for the award of any degree.

I declare that this written submission represents my ideas in my own words, and where others' ideas or words have been included, I have adequately cited and referenced the original sources. I also declare that I have adhered to all principles of academic honesty and integrity and have not misrepresented, fabricated, or falsified any idea/data/fact/source in my submission. I understand that any violation of the above will be a cause for disciplinary action by the Institute and can also evoke penal action from the sources that have thus not been appropriately cited or from whom proper permission has not been taken when needed.

Nitish Gupta
(Roll No: 719094)
Date: 22-01-2024
Place: NIT Warangal

Dedicated to

My grandparents, parents, and teachers

ACKNOWLEDGEMENTS

The work presented in this thesis has been possible with my close association with several people. I would like to express my heartfelt gratitude and appreciation towards all who made this Ph.D. thesis possible.

First and foremost, I would like to express my most profound appreciation and thanks to my thesis supervisor, **Dr. D. Bhargavi**, Associate Professor of Mathematics, National Institute of Technology, Warangal, India, who has been a remarkable mentor to me. Her continuous support, enthusiasm, inspiration, encouragement, and never-give-up attitude have deeply impressed me. During my interaction for the last four and half years at NIT Warangal, I have learnt a lot from her, including how to approach a problem systematically. I cherish the kind support of my supervisor, philosopher, and guide in all the ways. Her constant and critical evaluation during this period is thankfully acknowledged. I deem it a privilege to have worked under her amiable guidance. I am pleased to be associated with a mentor like Dr. D. Bhargavi.

I am also thankful to **Prof. J. V. Ramana Murthy (chairman), Prof. D. Srinivasacharya, Prof. KNS Kasi Viswanadham** Department of Mathematics and **Prof. V. Rajesh Khana Raju**, Department of Mechanical Engineering for their careful review and suggestions in their capacity as doctoral committee members. I am also grateful to past and present departmental heads of the department **Prof. P. Muthu, Prof. H. P. Rani, and Prof. A. Benerji Babu,** for providing me with enough facilities during my Ph.D. program.

It is a pleasure to express my thanks to **Prof. Y. N. Reddy, Prof. Debashis Dutta, Dr. R. S. Selvaraj, Dr. J. Pranitha, Dr. Ch. Ram Reddy, Dr. E. Satyanarayana, Dr. Y. Sreenivasa Rao, Dr. K. Kaladhar, Dr. Deepika Neela, Dr. Triveni Prasad Shukla, Dr. Srinivas Jangili, Dr. Jagannath Roy**, and non-teaching staff of the Department for their valuable suggestions, support, and timely help.

My profound gratitude goes out to **Prof. Ch. Sudhakar**, Associate Professor in the Department of Computer Science Engineering, for kindly providing the computing resources required to enable me to complete my doctoral research successfully.

I would like to sincerely thank **Dr. M. Raja Vishwanathan** of the Department of Humanities & Social Science for all his help and encouragement as I completed my doctorate.

The financial support provided by the Ministry of Education, Government of India, for research work at NIT Warangal is gratefully acknowledged.

I express my deepest gratitude to my mother, Smt. Poonam Gupta, father Sri Ajay Kumar Gupta, brother Dr. Abhay Gupta, and my friends Ajay Singh Rathore and Ashish Kumar, for their constant love, support, guidance, and encouragement towards my research work.

Finally, I would be grateful to my fellows of co-research scholars and my juniors Bikash, Naresh, Subhabrata, Nidhi, Anil, Suryakant, Brijesh, Ajay, Mrittika, and Rishav for their continuous sleepless, unfatigued, energetic, and fruitful discussions.

Above all, I am thankful to the Almighty God.

Place: NIT Warangal
Date: 22-01-2024 (Nitish Gupta)

ABSTRACT

This thesis introduces the local thermal non-equilibrium (LTNE) model as a framework for analyzing the forced convection heat transfer in the context of laminar flow within a thermally developing region within a parallel plate channel filled with porous media. Additionally, a transverse application of the magnetic field is imposed along the channel walls. Specific well-known parameters define the system, these being the Darcy number (*Da*), thermal conductivity ratio (κ), Forchheimer number (*F*), Hartmann number (*M*), Biot number (*Bi*), Peclet number (*Pe*), and Brinkman number (*Br*). Numerical solutions have been obtained by applying a successive accelerated replacement (SAR) scheme.

The numerical solutions have been obtained for the following values of the parameters characterizing the different problems studied. Darcy number: $0.001 \leq Da \leq 1.0$. Forchheimer number: $1 \leq F \leq 100$. Hartmann number: $0.5 \leq M \leq 65$. Biot number: $10 \leq Bi \leq 100$. When axial conduction is considered, Peclet number: $5 \leq Pe \leq 100$. When axial conduction is neglected, designated by $A_c = 0$, *Pe* is absorbed in $\ddot{\xi}^*$ and does not appear explicitly. When viscous dissipation is included, the Brinkman number: is $0.8 \leq Br \leq 100$.

The effect of Darcy number, Hartmann number, Biot number, and thermal conductivity ratio is discussed for the thermally developing region. The study presents outcomes concerning dimensionless temperature profiles in both the fluid and porous phases, the wall temperature and the local Nusselt number within the parallel plate channel. Notably, the local Nusselt number is influenced by a magnetic field and variations in the thermal conductivity ratio. A fully developed condition is validated when LTNE is used. It serves the purpose of the downstream boundary condition when axial conduction is used (elliptic PDE).

The influence of axial conduction on the forced convective heat transfer characteristics in a duct filled with porous material at a thermally developing zone under LTNE is discussed. The axial conduction effect is more at the low Peclet number, *Pe,* for all the Biot numbers, *Bi*. For large *Pe*, the axial conduction effect is negligible. The

validation of fully developed conditions for the local thermal non-equilibrium (LTNE) model is conducted.

The effect of two viscous dissipation models, the form drag (FD) model and the clear fluid compatible (CFC) model, is employed at the thermal entrance. The results include the effects of viscous dissipation on temperature profiles and local Nusselt numbers. The increment in the Brinkman number, Biot number, and thermal conductivity ratio improves the temperature distribution. The parametric structure of this study permitted mapping LTNE and local thermal equilibrium (LTE) areas across a wide range of these dimensionless parameters. Enhancement in the local Nusselt number is obtained in the CFC model compared to the value in the FD model.

Synergistic impact of axial conduction and viscous dissipation combined in the thermal-developing zone under LTNE framework in a duct packed with saturated porous medium. It explores the thermal characteristics of fluid flow through a porous medium confined within a channel defined by parallel plates. The channel walls are subject to a boundary condition with a constant wall heat flux. Enhancements in the Peclet number, Brinkman number, Biot number, and thermal conductivity ratio lead to improved temperature distribution. The parametric approach in this study enables the mapping of LTNE and local thermal equilibrium (LTE) regions across a broad spectrum of these dimensionless parameters.

N O M E N C L A T U R E

A_c	Axial conduction	K	Permeability, m^2
A_i	Constants are given in the appendix.	k_1	The ratio between the fluid thermal conductivity to fluid thermal conductivity
$\bar{B}$	Magnetic induction vector, $\left\|\bar{B}\right\| = B_0$, $Kgs^{-2}A^{-1}$	k_2	The ratio between fluid thermal conductivity to porous thermal conductivity
Bi	Biot number, $Bi = \frac{a_{sf} h_{sf} H^2}{k_{se}}$	k_f	Thermal conductivity in the fluid region, W/(m. K)
Br	Brinkman number, $Br = \frac{u_{ref}^2 \mu H}{q_w K}$	k_{fe}	Effective thermal conductivity in the fluid phase, W/(m. K)
C_p	Specific heat, J / g °C	k_p	Thermal conductivity of the porous, W/(m. K)
C_{fp}	Skin friction coefficient	k_{pe}	Effective thermal conductivity in porous phase, W/(m. K)
Da	Darcy number, $Da = K / H^2$	M	Hartmann number (Magnetic field parameter), $M = \sqrt{\frac{\sigma B_0{}^2 H^2}{\mu_f}}$
F	Forchheimer number, $F = \frac{\rho c_F}{\sqrt{K}} \frac{H^4}{\mu^2} \left(-\frac{dp}{dx^*} \right)$	NI	Number of iterations
F_L	Lorentz forces, $F_L = \bar{J} \times \bar{B}$	NI	Number of iterations
h_ξ	Local heat transfer coefficient, at the porous wall, W/m^2K	Nu_ξ	Local Nusselt number
H	Width of the channel, m	$Nu_{\xi,\, CFC}$	Nusselt number due to clear fluid-compatible model
$\bar{J}$	Electric current density, A/m^2	$Nu_{\xi,\, FD}$	Nusselt number due to form drag model

$\left(Nu_{fd}\right)_{DBM}$	Fully developed Nusselt number for Darcy Brinkman number	T_b	Bulk mean temperature, K
P	Dimensionless pressure	T_e	Inlet temperature, K
p	Pressure, kg $m^{-1}s^{-2}$	T_i	Interfacial temperature, K
PD	Number of divisions in the axial (ξ) direction	T_f	The temperature in the fluid phase, K
Pe	Peclet number, $Pe = u_{ref} H / \alpha_f$	T_p	The temperature in the porous phase, K
q_w	Constant wall heat flux, W/m^2	T_{wf}	Fluid phase temperature at the upper wall (at $y^* = H/2$), K
$q^S_{f,p}$	Internal heat generation term in fluid and porous region, W/m^3	T_{wp}	Porous phase temperature at the upper wall (at $y^* = H/2$), K
Q	Number of grids in the normal (η) direction	U	Dimensionless velocity
QD	Number of divisions in the normal (η) direction	x^*	Axial distance, m
Re	Reynolds number, $Re = \rho u_{ref} H / \mu_f$	y^*	Normal distance, m
s	Constant less than unity		

Greek symbols

ε	The ratio of the viscosity to the effective viscosity	ξ^*	The normalized dimensionless axial distance
ε_t	Error tolerance limit	$\Delta\xi^*$	Uniform cell width
η	Dimensionless normal distance, m	φ_f	The dimensionless temperature in the fluid phase
κ	The ratio of the effective porous thermal conductivity to the effective fluid thermal conductivity	φ_p	The dimensionless temperature in the porous phase
μ	Fluid viscosity, kg $m^{-1}s^{-1}$	φ_{wf}	Wall temperatures in the fluid phase
μ_e	Effective viscosity in Brinkman term, kg.$m^{-1}s^{-1}$	φ_{wp}	Wall temperatures in the porous phase

ξ	Dimensionless axial distance, m		

Abbreviations

CFC model	Clear fluid-compatible model	LTE	Local thermal equilibrium
DB	Darcy Brinkman	LTNE	Local thermal non-equilibrium
FD model	Form Drag model		

Subscript

e	Effective	*p*	Porous
f	Fluid	*w*	Wall

Contents

Chapter 1
INTRODUCTION

1.1 Introduction

Multiple applications for porous media are found in science, technology, and engineering. In recent years, scientists and engineers have been more interested in studying fluid flow and heat transfer in porous materials due to their relevance to many relevant physical processes. As of right now, there are a number of topics being actively researched and considered, including methods for carbon storage, enhancing heat transfer, solid matrix or microporous heat exchangers, subsurface water resources, fuel cells, solar absorbers, compact heat exchangers in general, and geological research.

Heat transfer is exchanging thermal energy between various parts of a system or distinct systems. A number of methods, including conduction, convection, and radiation, can cause this exchange. One of the three primary forms of heat transport, along with conduction and radiation, is convection. It deals with the transmission of heat from a moving fluid (gas or liquid) to a solid surface. Fluid movement, which transfers thermal energy from one location to another, propels convection. The fundamentals of heat transmission have been thoroughly examined by Shah and London [1], Kays and Crawford [2], and Whitaker [3] in their respective works.

In porous media, convection heat transfer is the term used to describe the transport of heat inside a material that has interconnected spaces or pores. Soils, rocks, ceramics, foams, and biological tissues are examples of materials that can be considered porous media. Via the voids in the material, fluids (gas or liquid) can pass through, and convection in the fluid-filled pores and conduction in the porous matrix both affect heat transmission in these media (ref., Nield and Bejan [4], Bejan [5], and Kaviany [6]).

Assuming that the porous matrix and fluid phase are in thermal equilibrium or thermal non-equilibrium, it is possible to describe the transport processes via porous media. Therefore, the local thermal equilibrium (LTE) model and the local thermal non-equilibrium (LTNE) model have been used as two distinct modelling approaches. When the fluid and porous phases temperature differences are disregarded, the LTE model based on the one-equation model is valid. This model has been utilized in several investigations of heat transport in porous materials, including high-temperature thermal energy systems, catalytic reactors, solar absorbers, enhanced recovery of oil by thermal methods, anomalous heat diffusion, microchannel heat sinks, plasma spectroscopy, energy storage systems, risk assessment of nuclear waste disposal systems, cooling of electronic components, and proton exchange membrane (PEM) fuel cells [7–16].

Usually, a porous material is involved in convective flow problems. In these problems, the porous skeleton temperature (T_p) may be distinct from the fluid temperature (T_f), and this framework is popularly named LTNE. These problems have been a keen interest for researchers due to the endless and exciting possibilities for implementing such equations in real-time applications. So, curiosity increases about the LTNE flows in porous media. For instance, LTNE is used in tube refrigerators employed in space, in flows that assume nanofluid order, in fuel cells, in flows involving resin, which is indispensable while processing composite materials, in the upkeep of reactors generating nuclear power, in exchangers where heat flow is typical, in flows where microchannels operate, in flows in metallic foams that are porous, and in the transport of textile materials, including solar energy storage systems, cooling rods, and nuclear reactors [17-29].

1.2 Brief Review on Flow and Heat Transfer in Parallel Plate Channels Filled with Porous Media under the LTNE model

In recent years, the cooling of electronic equipment employing materials including hyperporous media or microchannels has brought up the classic problem of forced convection in a channel created by two parallel plates. The overview discusses the

parallel plates under the LTE and the LTNE, along with typical advancements and contemporary investigations. Nield and Bejan [4] and Vafai [30] discussed convection in porous media. Pati et al. [31] recently highlighted the applicability of LTE and LTNE techniques in a critical review of LTE and LTNE.

Amiri and Vafai [32] addressed the impact of varying porosity and thermal dispersion, which were also analyzed under LTNE for various types of constant heat flux boundary conditions. In a channel filled with a fluid-saturated porous medium under LTNE with a constant wall heat flux condition, Bai and Nakayama [33] constructed an integral solution to describe the complete evolution of the thermal boundary layer. For the first time, an entire region map illustrating the points at which one area transitions to another is revealed by this analytical approach. These locations depend intricately on the thermal conductivity ratio and the Biot number.

Nield et al. [34] discussed how LTNE affected the thermal growth of forced convection in a saturated porous medium. LTNE involves the thermal expansion of forced convection in a saturated porous medium in a channel between parallel plates at a constant temperature. Further, Khashan et al. [35] demonstrated the LTNE effect for a tube geometry with constant wall temperature conditions. The findings showed that the LTE validity was expanded over the LTNE region as a result of the Peclet number declining and the Biot number rising.

Dehghan et al. [36] solved the coupled system equation of LTNE model using perturbation analysis for the parallel plate channel with constant heat flux boundary conditions and established a relation for the intensity of LTNE condition that is straightforward and essential for determining the significance of LTNE condition and validating numerical simulation results.

The Darcy number significantly affects the heat transfer rate in the developing area, according to Yi et al. [37], which discussed constant heat flux boundaries and a numerical and analytical investigation on thermally developing forced convective flow in a channel filled with a fluid-saturated porous medium under LTNE.

1.3 Porous Medium

The topic of porous media is well-known to everybody. These materials are all around us and impact our daily lives. There are many kinds of porous media and practically endless applications. The characteristics of the many different types of porous media that are accessible and the ability to use them effectively are the driving forces behind porous media theory.

A solid with holes connected in continuous channels across several directions is called a porous material. A solid matrix joined to create a network resembling a web comprised of porous media. The solids are placed in the medium's network to make pores between them. These pores are responsible for the flow through porous media. An essential characteristic of the porous medium's physical makeup is the size of its pores. Porous materials include fibrous aggregates, porous or fissured rocks, glass wool, human body organs, limestone, and fibreglass. The study of the flow of fluids through porous media has lately attracted much attention due to the recovery of crude oil from the pores of reservoir rocks. Other disciplines interested in the flow through porous media include biophysics, chemical engineering, solid physics, hydrology, and geophysics. Porous media must be studied because of all the applications, including heat exchangers, solar energy collectors, combustion processes, building insulation, nuclear waste disposal, sound absorption, alloy solidification, energy storage, chemical reactors, and petroleum recovery processes.

Fig. 1.1: Natural aggregate. Photograph taken on Seaham beach, March 2014

Fig. 1.2: Natural honeycomb

Effective porosity, ϕ, and permeability, K, are two characteristics that define the porous matrix in general. The effective porosity, or a portion of the medium that is occupied by the fluid, is made up of pores. An extra characteristic word, permeability, is required to distinguish between two porous mediums with the same porosity. Concerning Darcy's law, permeability is essentially the hydraulic conductance of the medium. The porosity of the medium and the corresponding particle diameter determine permeability.

1.3.1 Characterization and Governing Equations for Momentum

Darcy's Law

Darcy's law states that the volumetric flow rate (Q) in a porous medium has an inverse connection with the length (L) of the porous column and a direct association with the cross-sectional area (A) and hydraulic head differential (h_d). Darcy's law can be expressed as:

$$Q \propto \frac{h_d A}{L} \tag{1.1}$$

The hydraulic head difference, h_d, can be obtained from the equation below:

$$h_d = z + \frac{p}{\rho g} \tag{1.2}$$

In Eq. (1.2), z denotes elevation, p, pressure, ρ, density of the fluid, and g acceleration due to gravity. The Darcian velocity, v, is related to the volumetric flow rate by,

$$v = \frac{Q}{A} \tag{1.3}$$

The Darcy law can be expressed in a differential form as:

$$v = -\frac{K}{\mu}\left(\frac{dp}{dx^*} - \rho g\right) \tag{1.4}$$

In Eq. (1.4), K is the medium's permeability, and μ is the fluid's viscosity.

For a three-dimensional flow, Eq. (1.4), as given in Stanek and Szekely [38], takes the following form,

$$\vec{V} = -\frac{K}{\mu}\left(\nabla p - \rho\vec{g}\right) \tag{1.5}$$

In Eq. (1.5), $\vec{V}$ is the Darcian velocity vector and $\vec{g}$ is the gravity vector. From Eq. (1.5), it may be noted that the Darcy flow does not satisfy the no-slip condition at solid boundaries. In general, modifications to the Darcy description become necessary when the flow Reynolds number, based on the local velocity and pore diameter, is high.

Non-Darcy Extensions

Extensions of the Darcy law, including classical convective terms, non-linear inertia terms, and viscous factors, have been proposed to account for the flow inertia effects and boundary effects. The vector version of Catton's [39] governing equation for momentum conservation is as follows:

$$\frac{\mu}{K}\vec{V} + \rho\left(\frac{\mu_e}{\mu}\right)^2[\vec{V}.\nabla]\vec{V} + \rho\frac{K'}{K}\left|\vec{V}\right|\vec{V} = -\nabla p + \vec{B} + \mu_e\nabla^2\vec{V} \tag{1.6}$$

In Eq. (1.6), $K^{'}$ is the Forchheimer coefficient, and μ_e is an effective viscosity that considers the difference in the resistance offered for the fluid flow, though permeability may remain the same. For high-permeability foam, the effective viscosity can differ from the fluid viscosity by a factor of ten, as demonstrated by Givler and Altobellis [40]. $\vec{B}$ is the body force vector. In addition, the dimensionless of Eq. (1.6) leads to the parameters *Da*, the Darcy number and *F*, the Forchheimer number, defined by the equation below:

$$Da = \frac{K}{H^2} \tag{1.7}$$

$$F = \frac{K^{'}}{H} \tag{1.8}$$

The modified convective component, the second term on the left side of Eq. (1.6), includes the medium's permeability and porosity. The kinetic energy associated with turbulent motion is accounted for by the third component, also known as the Forchheimer non-linear inertial term. The second term on the right-hand side accounts for the boundary effects attributed to Brinkman. Brinkman friction terms are necessary to satisfy the no-slip velocity boundary condition. Generally, the literature dealing with the flow in porous media uses Eq. (1.6) or simplified forms. A brief literature survey of fluid flow in porous media and its applications is discussed in many kinds of literature [41–49].

1.4 Forced Convection in Ducts Filled with Porous Material

The subject of forced convection heat transfer in porous media is intriguing and has practical implications in several engineering domains; for example, refer to Bejan et al.'s work [7]. Both analytical and numerical treatment of various configurations of fluid flow and heat transfer has been done; see Nield and Bejan [4], Bejan [5], Kaviany [6], and Vafai [30]. Applications for forced convection include heat sink modelling, thermal optimization, heat sensitivity investigations, heat removal simulation of an electric fan, cooling of computer cases, fan-cooled central possessing units, water-cooled central

possessing units, cooling system design, heating system design, simulating printed circuit boards, etc. Heaters for automobiles, ceiling fans, convection ovens, pumps, suction devices, and hot air balloons are examples of forced convection.

1.4.1 Governing Equations for Thermal Energy Equation

In the majority of cases examined in the literature, it is commonly assumed that the porous matrix and the fluid flowing through it are in a state of LTE, implying that $T_f = T_p = T$, where T_f and T_p represent the temperatures of the fluid and porous phases, respectively. The LTE assumption suggests that the disparity between the volume-averaged temperatures of the fluid and porous phases is negligible. However, at the microscopic level, it is crucial to acknowledge that the temperature and heat flux rate at the interface between porous and fluid phases must be identical. Nevertheless, when considering the average value over a representative elementary volume, locally equal temperatures for the two phases may not be obtained.

In this instance, both phases are in the condition of LTNE. Investigations conducted by Vafai and Sozen [50], Vadasz [51], Stoner and Maris [52], and Intravaia et al. [53] demonstrated that a significant portion of applications fail to meet the LTE assumption. One such failure region associated with a rapidly fluctuating surface heat flow has been identified by Minkowycz et al. [54]. Moreover, Al-Sumaily et al. [55] have conducted an extensive review, summarizing the viability of the LTE theory. It leads to the conclusion that, in an LTNE scenario, there are always a variety of drives. As a result, the LTE thermal equilibrium approximation is no longer valid.

Following Nield and Bejan [4], the simplest way to model the LTNE is to use two thermal balance equations, one for the fluid and the other for porous phases. Taking the average over an elementary volume of the medium, the energy equation for fluid and porous phases is:

Energy equation in fluid phase:

$$\phi\left(\rho C_P\right)_f \frac{\partial T_f}{\partial t}+\left(\rho C_P\right)\vec{V}.\nabla T_f=\phi\ \nabla\left(k_f\ \nabla T_f\right)+h_{pf}a_{pf}\left(T_p-T_f\right)+\left(1-\phi\right)q_f^S \tag{1.9}$$

Energy equation in porous phase:

$$\left(1-\phi\right)\left(\rho C\right)_p \frac{\partial T_p}{\partial t}=\left(1-\phi\right)\nabla.\left(k_p\ \nabla T_p\right)+h_{pf}a_{pf}\left(T_p-T_f\right)+\left(1-\phi\right)q_p^S \tag{1.10}$$

In Eqs. (1.9) and (1.10), T_f and T_p are the temperatures in the fluid and porous phases. Here, f and p are the subscripts that refer to the fluid and porous phases, respectively. ϕ is the porosity, C_P is the specific heat at constant fluid pressure, C is the specific heat of the porous, and k is the thermal conductivity. The last term in both equations is the internal heating source term ($q_{f,p}^S$). Aditionally, a_{pf} is the interfacial area per unit volume of the porous media and h_{pf} is the porous-to-fluid heat transfer coefficient.

1.4.2 Porous Material Filled Duct under LTE

Numerous theoretical and experimental investigations into convective heat transport within porous media have been carried out, as documented by Hwang and Chao [56] and Jiang et al. [57]. These studies employed two distinct approaches, LTNE and LTE, considering the temperature at the interface between the porous and fluid zones. These approaches were utilized to estimate thermal transport phenomena in porous media.

The model of LTE posits that the temperature disparity between the fluid and porous phases in a porous system is negligible at any point within the bulk porous medium or that both phases maintain identical temperatures at all locations. This model has found widespread application in examining fundamental transport phenomena in porous media and has been extensively explored in literature dedicated to convection in such environments. The premise of the porous-matrix and fluid phases being in a state of LTE has fueled significant research on convective transport within porous media.

The LTE model has been utilized in several investigations of heat transport in porous materials (Mahjoob and Vafai [58] and Hooman and Merrikh [59]). Although the LTE model simplifies heat transfer computations, this is only sometimes the case when there is a significant temperature difference between the two phases. In these conditions, it is challenging to discount the effects of several behaviours that enhance internal heat exchange between the two phases. Because of this, the interstitial heat transfer coefficient and the interfacial surface, linked to the internal heat exchange between the porous and fluid phases, are crucial factors affecting heat transfer amplification in porous media (Marafie and Vafai [60]). Also, radiation and convection play essential roles in transferring heat in high-temperature thermal energy systems.

Table 1.1: An overview of related literature on flow and heat transfer in ducts filled with porous material under LTE

Sl. No.	**Geometry, Flow Field, Thermal Field and other Features in Brief**	**Boundary Conditions**	**Reference**
1	Two parallel porous plates, fully developed thermal and flow field, Brinkman-extended Darcy model.	Constant wall heat flux and constant wall temperature	Poulikakos and Kazmierczak [61]
2	Channels with parallel plates partially filled with porous medium, fully developed flow, and thermal field supposed to be fully developed. Darcy-Brinkman-Forchheimer flow model.	Constant wall temperature	Jang and Chen [62]
3	Channel with parallel plate partially filled with porous medium, fully developed thermal and flow field. Darcy-Brinkman-Forchheimer flow model.	Constant wall temperature	Vafai and Thiyagaraja [63]
4	Channel or pipe partially filled with porous medium, developing and fully developed flow conditions, Darcy-Brinkman-Forchheimer flow model.	Constant wall temperature	Mohamad [64]

Contd. on the next page

Table 1.1 - Contd.

Sl. No.	Geometry, Flow Field, Thermal Field and other Features in Brief	Boundary Conditions	Reference
5	External flow past a plate with alternate porous cavity-block obstacles was studied with a two-dimensional developing flow with a developing thermal field-Darcy-Brinkman-Forchheimer flow model and Navier-Stokes equations in porous and fluid regions, respectively. Axial conduction was included. Numerical solutions.	Constant wall temperature	Huang and Vafai [65]
6	Flow over intermittently emplaced porous cavities, flow, and a thermal field were developing. Darcy-Brinkman-Forchheimer model and Navier-Stokes equations in porous and fluid regions, respectively. Axial conduction was included. Stream-function vorticity formulation Numerical solutions.	Constant wall temperature	Vafai and Huang [66]
7	A porous layer was connected to the bottom wall of a parallel plate channel. A field was undergoing both hydrodynamic and thermal development. The Darcy-Brinkman-Forchheimer flow model. The flow and heat fields had boundary-layer approximations.	Constant wall temperature	Alkam et al. [67]
8	Porous substrates affixed to both walls of a vertical parallel plate channel, hydrodynamically developing two-dimensional mixed convection flow. Employing Navier-Stokes equations and the Darcy-Brinkman-Forchheimer flow model. In developing a thermal field, axial conduction was included. Numerical solution.	Constant wall temperature	Chang and Chang [68]

Contd. on the next page

Table 1.1 - Contd.

Sl. No.	Geometry, Flow Field, Thermal Field and other Features in Brief	Boundary Conditions	Reference
9	Circular pipe with a porous layer attached to the inside of the pipe. Fully developed thermal and flow field. Darcy Brinkman-Forchheimer model. Numerical solution.	Constant wall heat flux	Sayehvand and Shokouhmand [69]
10	Two parallel plates filled with porous material. Developing thermal field and fully developed flow field. Thermal asymmetry. Darcy model was applied. Analytical and numerical study.	Constant but unequal wall temperatures	Mitrovic and Maletic [70]
11	Two-dimensional flow in a horizontal pipe partially or fully filled with porous material. Developing thermal field and fully developed flow field. Darcy-Brinkman-Forchheimer model. Numerical Study.	Constant wall temperature	Teamah et al. [71]
12	A channel with a parallel plate partially filled with porous medium. A porous insert at the centre of the channel. Darcy-Brinkman-Forchheimer equation. Thermal and hydrodynamic fields dealt with fully developed. Analytical and numerical solutions.	Constant wall heat flux	Cekmer et al. [72]
13	Parallel plate channel geometry with an asymmetrically heated channel. Developing thermal field and fully developed flow field. Numerical Study.	Unequal wall temperatures	Repaka and Satyamurty [73]
14	A channel with a parallel plate partially filled with porous medium. Brinkman extended the non-Darcy model. Developing thermal field and fully developed flow field. Numerical Study.	Constant wall temperature	Satyamurty and Bhargavi [74]

Contd. On the next page

Table 1.1 - Contd.

Sl. No.	Geometry, Flow Field, Thermal Field and other Features in Brief	Boundary Conditions	Reference
15	A channel with a parallel plate partially filled with porous medium. Darcy-Brinkman model. Developing thermal field and fully developed flow field. Numerical Study.	Constant wall heat flux	Bhargavi and Reddy [75]
16	A channel with a parallel plate partially filled with porous medium. The Brinkman-extended Darcy equation. Fully developed flow field. Analytical Study.	Stress jump boundary condition	Kuznetsov [76]
17	Channel partially filled with a porous medium. The effects of axial conduction are included. The Darcy-Brinkman model. Developing thermal field and fully developed flow field. Numerical Study.	Constant wall heat flux	Reddy and Bhargavi [77]
18	Pulsating flows through a circular pipe with a porous layer attached to the inside of the pipe. Navier-Stokes equation and Darcy-Brinkman-Forchheimer flow model, respectively.	Constant wall heat flux	Guo, Kim and Sung [78]
19	Circular duct with a porous substrate attached at the wall. Thermal and hydrodynamic fields were supposed to be fully developed. Darcy-Brinkman-Forchheimer flow model.	Constant wall heat flux, constant wall temperature	Kuznetsov and Xiong [79]
20	A uniformly moving impermeable plate above and a porous layer of limited thickness below define the boundaries of a parallel plate channel. Hydrodynamics of fully developed flow. Poiseuille-Couette flow. Darcy Brinkman. It was analytically studied.	There was no slip condition at one wall, and the other moved with constant velocity.	Rudraiah [80]

1.4.3 Porous Material Filled Duct under LTNE

Many researchers have disputed the accuracy and assessment of LTE assumptions. The convective and radiative modes of heat transfer between different phases in the porous media, which are anticipated to represent a significant obstacle to the transmission of heat in the system, are sometimes ignored by LTE assumption in engineering problems. Indeed, the phase temperatures may differ depending on the type of transient process and the thermo-physical characteristics of the various phases. The performance of the device is dependent on the degree of non-equilibrium between the two phases in several thermal applications, including the cooling of nuclear fuel rods in coolant fluid baths and the storage of thermal energy in underground reservoirs. The temperature difference between the local fluid and porous phases is crucial in these thermal applications. Thus, instead of the LTE model, Nield and Bejan [4] discussed the LTNE model for the porous matrix and fluid phase in the temperature equation, which allows the separation in temperature between the porous and fluid phases with interphase temperature difference.

The LTNE model provides a more precise prediction of temperature fields in porous media, and therefore, researchers have paid significant attention to these issues. Many investigators (Phanikumar and Mahajan [81] and Jiang et al. [82]) have studied forced convection in ducts partially and fully filled with porous material in various conditions under the LTNE model. Because of its increased precision, the LTNE approach has been extensively utilised to examine heat transfer characteristics in a channel filled with porous media. Both models (LTNE and LTE) were employed by Phanikumar and Mahajan [81], who concluded that the LTNE model is more precise than the LTE model in projecting heat transport in metal foams by numerical simulation. Recently several authors (Alsabery et al. [83], Alhadhrami et al. [84], Barman and Rao [85], Prasannakumara [86], Xu et al. [87], Mansour et al. [88], Tayebi and Chamkha [89], Alsedais et al. [90]) employed a creatively presented paper with a variety of physical geometries that looks at a variety of causes and applications where LTNE is used.

In a series of inquiries, Rees [91] delved into the impact of LTNE on free convective fluxes within porous media. Baytas and Pop [92], utilizing an LTNE model, explored free convection within a porous square cavity. Additionally, Baytas [93] contributed a discussion on LTNE, free convection within a cavity filled with non-Darcy porous media. Saeid [94] investigated the same issue in a vertical porous layer, employing the LTNE model to study steady mixed convection in a two-dimensional computational setting. Furthermore, Malashetty et al. [95] scrutinized the influence of LTNE on the onset of convection in a porous layer, incorporating thermal diffusivity in a densely packed porous medium and anisotropy in permeability, along with the Lapwood-Brinkman model. Since these problems have been a subject of keen interest for researchers, it may be due to endless and exciting possibilities for implementing such equations in real-time applications. So, curiosity about LTNE flows in porous media has always attracted researches.

1.4.4 Thermal Boundary Condition under the LTNE Model

Under conditions of LTNE in porous media, a suitable set of boundary conditions involves a parallel plate channel geometry subjected to a constant heat flux boundary condition. Specifically, for the conditions at the heated wall with constant heat flux, two models introduced by Amiri and Vafai [96] were considered. These models were formulated based on distinct assumptions.

Model A: According to this model, the heat flux (q_w) is apportioned between two phases based on their effective thermal conductivities and the respective temperature gradients they exhibit.

$$\left.\begin{aligned} &\text{Upper wall:} \quad k_{fe}\frac{\partial T_f}{\partial y^*}+k_{pe}\frac{\partial T_p}{\partial y^*}=q_w \\ &\text{Lower wall:} \quad -k_{fe}\frac{\partial T_f}{\partial y^*}-k_{pe}\frac{\partial T_p}{\partial y^*}=q_w \end{aligned}\right\} \tag{1.11}$$

Model B: This model suggests that each phase receives an equal share of the heat flux, q_w.

$$\left.\begin{aligned} &\text{Upper wall:} \quad k_{fe}\frac{\partial T_f}{\partial y^*} = q_w \ \text{ and } \ k_{pe}\frac{\partial T_p}{\partial y^*} = q_w \\ &\text{Lower wall:} \ -k_{fe}\frac{\partial T_f}{\partial y^*} = q_w \ \text{ and } \ -k_{pe}\frac{\partial T_p}{\partial y^*} = q_w \end{aligned}\right\} \tag{1.12}$$

In the above Eqs. (1.11) and (1.12), T_f is the fluid phase temperature, T_p is the porous phase temperature, k_{fe} is the effective fluid thermal conductivity, k_{pe} is the effective porous thermal conductivity.

A comprehensive review of literature pertaining to flow and heat transfer in ducts filled with porous material under LTNE conditions reveals several key studies and findings. Researchers have extensively explored the complex interactions between fluid flow and heat transfer within porous media, considering the impact of LTNE phenomena. The noteworthy contributions of the LTNE model are summarized in the works authored by Kaviany [6], Straughan [28], and Nield and Bejan [4]. A survey of pertinent literature concerning the phenomena of flow and heat transfer in ducts containing porous material under the influence of the LTNE condition is given in Table 1.2.

Table 1.2: An overview of related literature on flow and heat transfer in ducts filled with porous material under LTNE

Sl. No.	Geometry, Flow Field, Thermal Field and other Features in Brief	Boundary Conditions	Reference
1	A fully filled channel was created via porous material with internal heat generation. Darcian flow model. Thermal and flow fields were supposed to be fully developed. Exact solutions and numerical study.	Constant wall heat flux with models A and B	Yang and Vafai [97]

Contd. on the next page

Table 1.2 - Contd.

Sl. No.	Geometry, Flow Field, Thermal Field and other Features in Brief	Boundary Conditions	Reference
2	A channel was filled with a porous medium. Thermal and flow fields dealt with fully developed conditions. The Darcy flow model. Analytical study.	Constant wall heat flux with model A	Lee and Vafai [98]
3	Metal foam-filled channel. Modified Brinkman-Forchheimer extended Darcy model. Developing flow and thermal fields, respectively. Numerical study.	Constant wall temperature	Sellar et al. [99]
4	Fully filled channel via porous material. Hydrodynamically fully developed Newtonian gas flow and developing thermal field. Darcy-Brinkman-Forchheimer model. Numerical study.	At the wall, temperature jumps and velocity slip	Haddad et al. [100]
5	Parallel plates were porous micro-channels filled with porous material. Brinkman-Darcy model. Thermal and flow fields were fully developed. Entropy generation analysis is performed. Analytical study.	At the wall, temperature jump and velocity slip at the wall, temperature jump and velocity slip	Buonomo et al. [101]
6	Parallel plates were porous micro-channels occupied with porous material. The Brinkman-Darcy model. Thermal and flow fields took up fully developed. Numerical study.	At the wall, temperature jumps and velocity slip	Buonomo et al. [102]
7	The channel was partially occupied with a porous medium. Fully developed flow and thermal field. The Darcy-Brinkman equation flow model. Entropy generation analysis was performed. Analytical study.	Constant wall heat flux with models A and B	Mahmoudi and Maerefat [103]

Contd. on the next page

Table 1.2 - Contd.

Sl. No.	Geometry, Flow Field, Thermal Field and other Features in Brief	Boundary Conditions	Reference
8	A porous medium partially occupies the channel, serving as the middle of the channel. Fully developed Thermal and flow fields. The Darcy-Brinkman-Forchheimer flow model. Analytical study. The exact solution had been determined.	Constant wall heat flux with models A and B	Karimi et al. [104]
9	A filled channel is created via porous material with internal heat generation. Fully developed thermal and flow fields. Biot number varies across the channel. Darcy model. Analytical study.	Constant wall heat flux with models A and B	Parhizi et al. [105]
10	Partially filled channel via porous material with internal heat generation. Thermal and flow fields were fully developed. The Biot number was varied across the channel. Darcy flow model. Analytical study.	Constant wall heat flux with models A, B and C	Krishnan et al. [106]
11	A channel with porous material with internal heat generation. Fully developed flow and thermal fields. Unsteady, pulsating fluid flows in the channel. Darcy-Brinkman flow model. Analytical study.	Constant wall heat flux with model A	Fathi-Kelestani et al. [107]
12	Partially filled channel via porous material with internal heat generation. Fully developed flow and thermal fields. Brinkman-extended Darcy flow model. Analytical study.	Constant wall heat flux with models A, B and C	Li et al. [108]
13	Partially filled channel via porous material with internal heat generation. Fully developed flow and thermal fields. Brinkman-extended Darcy flow model. Analytical study.	Constant wall heat flux with model A	Hu and Li [109]
14	Partially filled channel via porous material. Thermal and flow fields were fully developed. Darcy flow model. Analytical study.	Constant wall heat flux with models A, B, and C	Ouyang et al. [110]

Contd. on the next page

Table 1.2 - Contd.

Sl. No.	Geometry, Flow Field, Thermal Field and other Features in Brief	Boundary Conditions	Reference
15	Partially filled channel via porous material. Fully developed flow and thermal fields. Brinkman-extended Darcy model. Analytical study.	Constant wall heat flux with model A and stress jump interface conditions	Li and Hu [111]
16	Partially filled channel via porous material with internal heat generation. Fully developed flow and thermal fields. Darcy-Brinkman model. Analytical study.	Constant wall heat flux with models A and B	Dehghan [112]
17	Partially porous medium-filled channel with internal heat generation. Thermal and flow fields were fully developed. Darcy flow model. Analytical study.	Constant wall heat flux with model B	Dehghan et al. [113]
18	The channel contains a highly porous medium of open-celled metallic foam, with symmetrical sintered foam layers on the upper and lower plates. Thermal and flow fields were fully developed. The porous region was governed by the Brinkman-Darcy model. Analytical study.	Constant heat flux at a wall with model A	Xu et al. [114]
19	The channel was occupied by a highly porous medium with high porosity. Thermal and flow fields were fully developed. Brinkman–Forchheimer-extended model employed. Analytical study.	Constant heat flux at a wall with model A	Yi et al. [115]
20	A channel was occupied by a porous medium experiencing thermal radiation. Developing thermal field and fully developed flow field. Darcy-Brinkman-Forchheimer flow model. Numerical study.	Constant heat flux with models A and B	Mahmoudi [116]

Contd. on the next page

Table 1.2 - Contd.

Sl. No.	Geometry, Flow Field, Thermal Field and other Features in Brief	Boundary Conditions	Reference
21	The channel-filled, partially filled, open-celled porous layer was symmetrically sintered on the upper and bottom plates. Thermal and flow fields were assumed to be fully developed. The Brinkman-Darcy equation flow model. Entropy generations in endothermic and exothermic channels were discussed. Analytical study.	Constant heat flux at a wall with model A	Torabi et al. [117]
22	Partially filled cylinder via porous material. Thermal and flow fields were fully developed. The Brinkman-extended Darcy flow model. Analytical study.	Constant heat flux at the wall with model A	Dukhan, and Hooman [118]
23	The channel was occupied by porous material, featuring thick walls with internal heat generation. Thermal and flow fields were fully developed. Darcy-Brinkman flow model. Two variations of asymmetric boundary conditions were taken into consideration. Analytical study.	Case1: Constant but unequal wall temperature. Case2: Constant wall heat flux with models A and convective boundary conditions at walls	Elliott et al. [119]
24	Study of a two-dimensional channel partially occupied by a porous insert; this scenario incorporates consumption (endothermicity) and internal heat generation (exothermicity). Thermal and flow fields were fully developed. Darcy Brinkman model flow model. Numerical study.	Constant heat flux at a wall with models A and C	Karimi et al. [120]
25	In the slip-flow regime, a micro-channel was filled with porous material with internal heat generation. Thermal and flow fields were fully developed. Darcy flow model. Analytical and numerical study.	Constant wall heat flux with models A and B	Dehghan et al. [121]

Contd. on the next page

Table 1.2 - Contd.

Sl. No.	Geometry, Flow Field, Thermal Field and other Features in Brief	Boundary Conditions	Reference
26	The channel was partially filled with an asymmetric porous material. Thermal and flow fields were fully developed. The Darcy-Brinkman flow model. Analytical study.	The upper wall was at constant wall heat flux with model A, and the lower wall was isolated.	Tajik Jamal-Abad [122]
27	A highly porous medium composed of open-celled metallic foam featuring symmetrically sintered foam layers on the upper and bottom plates occupied a portion of the channel. The flow was steady and pulsatile. Thermal and flow fields were fully developed. Brinkman-Forchheimer flow model. Numerical study.	Constant wall heat flux with model B	Forooghi et al. [123]
28	A portion of the channel was occupied by a highly porous medium comprising open-celled metallic foam featuring symmetrically sintered foam layers on both the upper and bottom plates. Developing thermal field and fully developed flow field. The Brinkman-Forchheimer flow model. Numerical study.	Constant wall temperature	Abkar et al. [124]
29	Fully partially filled channel via porous material. Developing thermal field and fully developed flow field. Darcy-Brinkman flow model. Numerical study	Constant wall heat flux with model B	Baig et al. [125]
30	Fully filled channel via porous material. Thermal and flow fields were fully developed. Brinkman-Forchheimer-extended Darcy flow model. Perturbation Analysis.	Constant wall temperature	Dehghan et al. [126]
31	Tube filled with metal foam. The Darcian average was considered for the flow in porous media. Thermal and flow fields were fully developed. Analytical study.	Constant wall heat flux with model A	Yang et al. [127]

Contd. on the next page

Table 1.2 - Contd.

Sl. No.	Geometry, Flow Field, Thermal Field and other Features in Brief	Boundary Conditions	Reference
32	Two-dimensional simulations of heat transfer through porous material partially filled in a parallel channel were considered. Developing thermal field and developed flow field. Brinkman-Forchheimer extended Darcy flow model. Numerical study.	Constant wall temperature	Abdedou and Bouhadef [128]
33	A saturated porous medium occupies a tube. Thermal and flow fields were fully developed. Brinkman-Forchheimer-extended Darcy equation. The study encompasses both analytical and numerical analyses.	Constant wall temperature	Dehghan et al. [129]
34	Saturated porous medium-filled micro-channel. Internal heat generation. Darcy-Brinkman flow model. Thermal and flow fields were fully developed. Numerical study.	Variable wall heat flux and wall temperature. Temperature jump condition	Seetharamu et al. [130]
35	The pipe was partially filled with a porous medium with a centred porous layer in the channel. Thermal and flow fields were fully developed. Darcy–Brinkman–Forchheimer-Darcy flow model. Numerical study.	Constant wall heat flux with models A and B	Mahmoudi and Karimi [131]
36	Annulus filled with porous. Darcian velocity over the cross-section. Thermal and flow fields were fully developed. Approximation solutions and analytical study.	Constant heat flux at an inner wall with model A and the outer wall was adiabatic.	Yang et al. [132]
37	The tubes contain a partial filling of metallic foam. The interface between the foam and foam-free regions within the tube was concentric. Thermal and flow fields were fully developed. Brinkman-extended Darcy flow model. Analytical study.	Constant heat flux at a wall with model A	Xu et al. [133]

Contd. on the next page

Table 1.2 - Contd.

Sl. No.	Geometry, Flow Field, Thermal Field and other Features in Brief	Boundary Conditions	Reference
38	Tubes were partially filled with gradient metal foams (GMFs). The interface between the foam and foam-free regions within the tube was concentric. Thermal and flow fields were fully developed. Brinkman-extended Darcy flow model. Numerical study.	Constant heat flux at the wall with model A	Xu et al. [134]
39	Microfoams were sandwiched between two parallel plates with asymmetric heating. Thermal and flow fields were fully developed. Brinkman–Forchheimer- Darcy flow model.	Velocity slip and thermal slip with model A	Xu et al. [135]
40	Investigating heat transfer and entropy generation in a tube filled with double-layer porous media. Analytical study. Darcy-Brinkman's flow model. Analytical study.	Constant wall heat flux with model A	Yang et al. [136]

1.5 Viscous Dissipation in Flows Through Porous Media

The generation of thermal energy due to viscous stresses occurs in the viscous flow of clear fluids and the fluid flow within porous media. The impact of heat released through viscous dissipation becomes noteworthy when a dimensionless parameter, known as the Brinkman number (*Br*), attains higher values. Considering that the effective viscosity can be significantly higher {see Givler and Altobellis [40]} than fluid viscosity when flows through the porous medium are encountered, the Brinkman number shall be considerably higher than that for clear fluid flows. Current applications that involve fluid flow through porous media necessitate the consideration of viscous dissipation effects in the energy conservation equation. The phenomenon of viscous dissipation holds relevance in various applications. For instance, noticeable temperature increases occur in polymer processing flows, such as injection moulding or high-rate extrusion.

Additionally, aerodynamic heating in the thin boundary layer around high-speed aircraft elevates the skin temperature. These applications may generally involve internal flows, such as the flow through porous materials, fully or partially filled channels, and ducts. When the effective fluid viscosity is high, temperature differences are slight, or kinetic energy is substantial, viscous dissipation is expected to play a significant role. A detailed exploration of the importance of dissipation can be found in Vafai [30].

1.5.1 Dissipation Modeling

The form of the dissipation function, ψ, for flows through porous media is not unique. In deriving the conservation of {as in, say, Shah and London [1], Schlichting and Gersten [137] and Al-Hadhrami et al. [138 and 139], or for more generality} thermal energy equation for clear fluid flows, mechanical energy equation is subtracted from the overall conservation of energy equation. Different models proposed by other authors for the dissipation function for porous media have not always been compatible with the momentum equation used in those investigations.

The forms of the dissipation function, ψ, available in the literature for flow through porous media for unidirectional flow, are as follows.

Nield [140]: $$\psi = \left(\frac{\mu}{K}\right)u^2 - \mu_e u\left(\frac{d^2u}{dy^{*2}}\right) \tag{1.13}$$

Al-Hadhrami et al. [138 and 139]: $$\psi = \left(\frac{\mu}{K}\right)u^2 + \mu_e\left(\frac{du}{dy^*}\right)^2 \tag{1.14}$$

1.5.2 Forced Convection in Channels Filled with Porous Material with Viscous Dissipation

A general review of the dissipation models in porous media was developed, and the background is available in Nield and Bejan [4]. When the thermal energy equation includes a viscous dissipation term involving Brinkman number, Nield [140] termed it

the Brinkman-Brinkman problem. The different dissipation functions that have been proposed are given by Eqs. (1.13) to (1.14).

In porous media, the impact of viscous dissipation on internal forced convection has received much attention over the past ten years due to its numerous applications in heat pipes, electronics cooling, catalytic reactors, and other devices. Vafai [30] describes the utility of dissipation. Nield and Bejan [4] provided a basic overview of the dissipation models in porous media. Viscous dissipation was initially considered by adding a velocity square term to the energy equation for the porous media (Bejan [5] and Nield [140]). Later, a new paradigm for viscous dissipation was proposed by Al-Hadhrami et al. [139]. Extensive research has been done for various geometries to examine the impact of viscous dissipation on internal forced flow problems. The majority of these studies assume LTE between the porous and fluid phases. Fully developed issues with various boundary conditions and viscous dissipation functions were addressed by several authors (Nield et al. [141], Tso et al. [142], and Nakayama and Shenoy [143]).

The adoption of the LTNE model considering viscous dissipation is relatively limited in existing studies. This investigation specifically compared the differences between LTE and LTNE models, revealing a pronounced influence of viscous dissipation on the Nusselt number. The study delved into the effects of various relevant parameters, including Biot number, Darcy number, Brinkmann number, and thermal conductivity ratio, and discussed the significance of thermal asymmetries in heat transfer. In a related context, Baig et al. [144] scrutinized the impact of viscous dissipation within the LTNE model under constant heat flux boundary conditions. Under the LTNE model, Buonomo et al. [145] explained that temperature gradients in the fluid and porous along the sections decrease as temperature and velocity increase. An increase in bulk heat transfer improves the heat transmission at channel walls.

Tables 1.3 and 1.4 provide an overview of the literature concerning convective heat transfer through porous media, encompassing dissipation and detailing the utilized LTE and LTNE models.

Table 1.3: An overview of the literature on flow and heat transfer in various geometries filled with porous material, including dissipation under LTE

Sl. No.	Geometry, Flow Field, Thermal Field and other Features in Brief	Boundary Conditions	Reference
1	The channel Filled via porous material fully developed flow with Darcy model and developed thermal field.	Constant wall temperature	Hooman and Gurgenci [146]
2	Porous material was bounded by parallel plate channel and fully developed thermal and flow fields, with the Darcy- Brinkman model. Different dissipation models yielded almost the same results for small Darcy numbers.	Constant wall temperature and constant wall heat flux	Nield et al. [147]
3	Filled channel via porous material under the LTE model. Viscous dissipation was applied. Thermal and flow fields were fully developed. The Brinkman-Darcy equation flow model. Analytical and numerical solutions were obtained.	Unequal, constant wall temperature	Mahmud and Fraser [148]
4	Filled channel via porous material under the LTE model. Viscous dissipation was applied. Thermal and flow fields were fully developed. The Brinkman-Darcy flow model. An analytical solution has been obtained.	Constant wall heat flux	Hung and Tso [149]
5	Partially filled channel via porous material. Three viscous dissipation models were applied. The conduction limit was considered. The Brinkman-Darcy flow model. An analytical solution has been obtained.	Constant wall heat flux	Bhargavi and Reddy [150]
6	Two-dimensional laminar forced convection. Developing thermal field and fully developed flow field. The flow between asymmetrically heated parallel plates was studied. Numerical study.	Isothermal with unequal temperature	Repaka and Satyamurty [151]

Contd. On the next page

Table 1.3 - Contd.

Sl. No.	Geometry, Flow Field, Thermal Field and other Features in Brief	Boundary Conditions	Reference
7	Vertical plate. Steady mixed convection flow employing the Darcy-Forchheimer model. Boundary layer approximation was made in the energy equation. Effects of thermal dispersion and viscous dissipation were studied.	Isothermal wall temperature	Murthy [152]
8	Vertical plate. Analytical solution for steady free convection employing Darcy model. Boundary layer approximation was made in the energy equation.	Constant wall temperature	Rees et al. [153]
9	Vertical plate channel. Numerical solution for fully developed free and forced convection flow employing Darcy model. Axial conduction was considered.	Equal and unequal wall temperatures	Ingham et al. [154]
10	Vertical Plate. Analytical solution for two-dimensional mixed convection employing the Darcy-Forchheimer model. Boundary layer approximation was made in the energy equation.	Isothermal wall temperature	Tashtoush [155]
11	Partially filled vertical channel via porous material. Thermal dissipation and Darcy dissipation were considered. Brinkman-extended Darcy. They mixed convection flow. Thermal and flow fields were fully developed. Homotopy perturbation method.	Stress jumped and constant but unequal wall temperature	Abiodun et al. [156]
12	Partially filled vertical channel via porous material. Thermal dissipation and Darcy dissipation were considered. Brinkman-extended Darcy. Natural convection flow. Thermal and hydrodynamic fields were fully developed. Homotopy perturbation method.	Stress jumped and constant but unequal wall temperature	Abiodun et al. [157]

Contd. on next page

Table 1.3 - Contd.

Sl. No.	Geometry, Flow Field, Thermal Field and other Features in Brief	Boundary Conditions	Reference
13	The channel was filled via porous material, and the flow was fully developed with the Darcy Brinkman model. Developing thermal field, including axial conduction. A modified Graetz methodology. Three models were evaluated.	Constant wall temperature	Nield et al. [158]
14	Circular duct filled with porous material, Darcy Brinkman model. The development of a thermal field included viscous dissipation and axial conduction. Numerical solution.	Constant wall heat flux	Hooman et al. [159]
15	Vertical channel with symmetric and asymmetric heating. Steady mixed convection flow employing the Darcy model. Thermal and flow fields were fully developed. Effects of thermal dispersion and viscous dissipation were studied. Perturbation method.	Isothermal with equal or unequal temperatures	Barletta [160]
16	An inclined channel with asymmetric heating. Steady mixed convection flow employing the Darcy model. Thermal and flow fields were fully developed. Effects of thermal dispersion and viscous dissipation were studied. Perturbation method.	Isothermal with unequal temperatures	Barletta and Zanchini [161]
17	Couette-Poiseuille flow between parallel plates with viscous dissipation was studied. Thermal and flow fields were fully developed. Analytical study.	One wall was at constant heat flux, and the other was at adiabatic	Aydim and Avic [162]
18	Couette-Poiseuille flow between parallel plates with viscous dissipation occurs. Thermal and flow fields were fully developed. Analytical study.	Unequal and constant wall heat flux	Chen et al. [163]
19	Partially filled channel via porous material with viscous dissipation and axial conduction was studied. Thermal and flow fields were fully developed. The Brinkman-Darcy equation flow model. An analytical solution was obtained.	Constant wall heat flux	Bhargavi and Reddy [164]

Table 1.4: An overview of the literature on flow and heat transfer in various geometries filled with porous material, including dissipation under LTNE

Sl. No.	Geometry, Flow Field, Thermal Field and other Features in Brief	Boundary Conditions	Reference
1	A channel with porous material with viscous dissipation. Thermal and flow Brinkman-Darcy flow model. Analytical study.	Constant wall heat flux with model A	Chen and Tso [165]
2	The channel was filled via porous material with viscous dissipation. They were developing a thermal field and a fully developed flow field. The Brinkman-Darcy equation flow model. Analytical study.	Constant wall heat flux with model A	Chen and Tso [166]
3	Parallel plates were porous micro-channels filled with porous material with viscous dissipation. The Darcy-extended Brinkman flow model. Developing thermal field and fully developed flow field. Numerical studies.	At the wall, temperature jumps and velocity slip	Buonomo et al. [167]
4	Partially filled channel via porous material with viscous dissipation under the LTNE model. Developing thermal field and fully developed flow field. The Darcy- Brinkman model equation flow model. Entropy generation analyses were discussed. An analytical solution was obtained.	The upper wall was adiabatic, and the lower wall was at constant heat flux with model A	Torabi et al. [168]
5	Fully filled channel via porous material. Developing thermal field and fully developed flow field. Viscous dissipation was considered. Darcy flow model. Analytical study.	Constant wall temperature	Yang and Liu [169]
6	Fully filled channel via porous material. Thermal and flow fields were fully developed. Viscous dissipation was considered. Darcy Brinkman flow model. Entropy generation was calculated. Analytical study.	Constant but unequal wall heat flux with model A	Chee et al. [170]

Contd. on the next page

Table 1.4 - Contd.

Sl. No.	Geometry, Flow Field, Thermal Field and other Features in Brief	Boundary Conditions	Reference
7	A horizontal microchannel with thick walls that was filled with porous material. Fields were completely developed in terms of heat and hydrodynamics. Considerations include magnetic field and viscous dissipation. To depict the fluid flow in the porous media, utilised the Darcy equation. Investigated analytically.	Case 1: Constant but unequal wall temperature. Case 2: Convective boundary conditions for the upper wall and constant heat flux at the lower wall	Torabi and Peterson [171]
8	A porous media was inserted into a microchannel. Within a microchannel embedded in a porous medium, a water-alumina nanofluid flows. Thermal and flow fields were fully developed. Viscous dissipation was considered. Darcy Brinkman flow model. Entropy generation was calculated. Analytical study.	Constant wall heat flux with model A	Ting et al. [172]
9	Single microchannels that were filled with porous materials make up a microreactor. There were two substantial barriers in the microstructure of the system. A catalytic coating was present on the inside surface of the microchannel. Thermal and flow fields were fully developed. Viscous dissipation was considered. Darcy Brinkman flow model. The advective-diffusive model governed mass transfer. Entropy generation was calculated. Analytical study.	Unequal wall heat flux	Hunt et al. [173]

Contd. on the next page

Table 1.4 - Contd.

Sl. No.	Geometry, Flow Field, Thermal Field and other Features in Brief	Boundary Conditions	Reference
10	A microreactor consists of a single microchannel filled with porous materials. CuO-Water nanofluid was considered. Thermal and flow fields are fully developed. Viscous dissipation was considered. Darcy Brinkman flow model. Temperature field in a microchannel heat sink. Analytical study.	The upper plate was insulated, and the lower plate was at constant heat flux with model A	Chen and Tso [174]
11	A microreactor consists of a single microchannel filled with porous materials. Alumina water nanofluids were considered. Thermal and flow fields were fully developed. Viscous dissipation was considered. Darcy Brinkman flow model. New temperature field in a microchannel heat sink. Numerical study.	The upper plate was adiabatic, and the lower plate was at constant heat flux with model A	Loh et al. [175]
12	Mixed convective heat transfer in a vertical micro-porous channel. Viscous dissipation and internal heat generation. Darcy Brinkman flow model. A numerical solution was obtained by applying the finite element method.	Asymmetric constant wall temperature and constant wall heat flux	Leela et al. [176]
13	Horizontal channel filled with a porous medium. Thermal and flow fields were fully developed. The energy equation includes two viscous dissipation terms. The temperature distribution was local, and total entropy generation was discussed. Analytical-numerical solution technique.	Case1: asymmetric constant wall temperature Case2: Convective boundary condition	Torabi and Zhang [177]
14	Plate channels are filled with metallic or packed beds. The Brinkman-Darcy-Forchheimer model had variable properties: porosity, thermal dispersion, and viscous dissipation. Flow and thermal fields were developing. Numerical study.	The upper plate was at constant wall heat flux with model B, and the lower plate was adiabatic.	Jiang et al. [178]

1.6 Magnetohydrodynamics (MHD)

Numerous technical and industrial fields, such as the petroleum industry, plasma research, geothermal energy extraction, and others, have found significant applications for studying magnetohydrodynamic (MHD) flow and heat transfer for a viscous incompressible fluid across a plate. An area of continuum mechanics called magnetohydrodynamics focuses on how magnetic fields affect the motion of electrically conducting fluids. Moving magnetic lines of force cause potential differences that lead to the creation of electric currents in working materials. These currents alter the magnetic field in turn. The Lorentz force, the passage of an electric current through a magnetic field, also affects fluid flow.

In their study, Raju et al. [179] explored the magnetohydrodynamic (MHD) of forced convective flow of a viscous fluid with finite depth in a saturated porous medium over a stationary horizontal channel. The investigation considered a thermally insulated and impermeable bottom wall, incorporating Joule heating and viscous dissipation considerations. Sharmila and Saranya [180] delved into the impact of a magnetic field on fully developed forced convection through a porous medium confined by a parallel plate channel, taking into account boundary and inertial effects. Numerous researchers, including Kurzweg [181], Gulab Ram and Mishra [182], Raptis and Kafousias [183], Raptis and Perdikis [184], Manju et al. [185], and Vineet and Amit [186] have examined the influence of magnetic fields on fluid flow across various geometries and under diverse conditions.

Baoku et al. [187] investigated the influence of magnetic field, thermal radiation, and thermal conductivity on the Couette flow of a highly viscous fluid with temperature-dependent viscosity through a porous channel. The researchers obtained a numerical solution employing finite difference methods. Several researchers, including Ashish et al. [188], Ghofrani et al. [189], Sheikholeslami et al. [190], Takhar and Beg [191], Barletta et al. [192], Guven et al. [193], Sahar [194], Srivastava and Satya [195], and Jhankal et al. [196], have investigated the interaction between forced convection and porous medium/magnetic field due to its relevance in engineering applications.

1.7 Numerical Method

The intended studies involve pursuing numerical solutions for two-dimensional conservation of energy equations in fluid and porous phases, incorporating viscous dissipation and axial conduction. These computations are highly demanding, even within the established velocity field framework. When accounting for axial conduction, the conservation of the thermal energy equation exhibits an elliptic nature. In the context of the considered internal flows, applying a downstream boundary condition at an unknown axial distance necessitates an iterative approach to reach a solution. Several numerical techniques have been extensively employed for this class of flows. One such method involved using an implicit finite-difference scheme to solve the energy conservation equation with a boundary layer approximation, as demonstrated by Habchi and Acharya [197]. Naito and Nagano [198] successfully obtained numerical solutions for the full Navier-Stokes and energy equations using the Successive Over-Relaxation (SOR) method. Nguyen [199] employed the Alternating Direction Implicit (ADI) [200, 201] and Quadratic Upwind Interpolation for Convective Kinematics (QUICK) [202] methods to solve the Navier-Stokes and energy equations in finite difference form. Jeng et al. [203] utilized the SIMPLER (Semi-Implicit Method for Pressure Linked Equations-Revised) algorithm with a staggered grid system. Krishnan and Sastri [204] adopted the Crank-Nicholson semi-implicit scheme to solve the energy equation. Min et al. [205] solved the discretized momentum and energy equations using a line-by-line approach with the TDMA (Tri-Diagonal Matrix Algorithm), while the pressure equation was solved using a line SOR method.

The Successive Acceleration Replacement (SAR) scheme is a non-linear over-relaxation method introduced by Lew [206], Lieberstein [207], and Dellinger [208]. Lew [206] and Dellinger [208] employed the SAR scheme to solve non-linear ordinary differential equations, with Dellinger's approach differing primarily in the choice of the relaxation factor. Satyamurty [209] demonstrated the applicability of the SAR scheme in solving a system of partial differential equations for studying two-dimensional natural convection heat transfer in porous media. This scheme has been extensively applied by researchers such as Satyamurty and Marpu [210], Marpu and Satyamurty [211], Satyamurty and Marpu [212], Marpu and Satyamurty [213], Marpu [214],

Sharma [215], and Prakash Chandra [216]. More recently, the SAR scheme has been employed for forced convection studied by Bhargavi and Reddy [75], Satyamurty and Bhargavi [217], and Jagadeesh and Satyamurty [218]. The present thesis has chosen the SAR scheme to obtain numerical solutions for the problems under investigation.

Philosophy of Successive Accelerated Replacement (SAR)

The core principle underlying the SAR scheme is to suggest a profile for each variable that satisfies the specified boundary conditions. Consider the partial differential equation that governs a variable, $\varphi(X,Y)$, expressed in finite difference form as $\bar{\varphi}_{P,Q}=0$. This equation represents the nodal point (*P*, *Q*), when the non-dimensional height and length of the channel are divided into a finite number of intervals, denoted as *PD* and *QD*, respectively. The presumed profile for the variable φ at any mesh point typically does not fulfil the equation. Define the error in the equation at coordinates (*P*, *Q*) and the k^{th} iteration as $\bar{\varphi}^{\text{k}}_{P,Q}$. The following sources yield the $(k+1)^{\text{th}}$ approximation to the variable φ:

$$\varphi^{\text{k+1}}_{P,Q}=\varphi^{\text{k}}_{P,Q}-\omega\left\{\frac{\bar{\varphi}^{\text{k}}_{P,Q}}{\left(\partial\bar{\varphi}^{\text{k}}_{P,Q}/\partial\varphi_{P,Q}\right)}\right\} \tag{1.15}$$

The acceleration factor ω in Eq. (1.15) ranges from $0<\omega<2$. A value of $\omega>1$ indicates over-relaxation, while $\omega<1$ implies under-relaxation.

Until a convergence requirement is met, the variable φ is corrected at every mesh point over an entire region of interest. The requirement is that, at any mesh point between the k^{th} and $(k+1)^{\text{th}}$ approximations, the normalized change in the variable must satisfy the condition given below:

$$\left|1-\left(\frac{\varphi^{\text{k}}_{P,Q}}{\varphi^{\text{k+1}}_{P,Q}}\right)\right|<\varepsilon_t \tag{1.16}$$

where the error tolerance limit, ε_t, is a tiny, positive value that is prescribed. It is necessary to associate each dependent variable with an equation to correct the first estimated profiles. It is common practice to link the equation containing that variable's highest-order derivative.

1.8 Lacune in the Past Study on Forced Convection Heat Transfer in the Channels Under LTNE Model

Motivated by the relevance to several modern applications, including fuel cells, solar absorbers, and catalytic converters, the present studies seek to investigate forced convection within channels filled with a porous material. As was previously said, porous channels can be the primary geometry of interest in a device, or they can add a porous insert to enhance heat transmission. By forming a convoluted channel and manipulating effective thermal conductivity, forced convection in ducts packed with porous material presents an opportunity to improve heat transmission. Extending the findings of earlier studies by Shah and London [1], Vafai [30], Mahjoob and Vafai [58], Hooman and Merrikh [59], Poulikakos and Kazmierczak [61], Bhargavi and Reddy [75], and Barletta [160], it is predicted that porous material-filled channels will show a higher increase in Nusselt number than when compared to clear fluid flow configurations under local thermal equilibrium (LTE) model. When considering variables like viscous dissipation, it is vital to assess the influence on heat transport cautiously.

The transport processes through porous media, consisting of a fluid phase and a porous matrix, can be modelled by considering both to be in local thermal equilibrium (LTE) or local thermal non-equilibrium (LTNE). The LTE model based on the one-equation model is valid when the temperature difference between the fluid and porous phases is neglected. The LTNE conditions refer to a situation where different components or regions within a system are not in thermal equilibrium with each other. Research by Vadasz [51], Intravaia et al. [53], Stoner and Maris [52], Vafai and Sozen [50], and Vadasz [51] demonstrated that a significant percentage of applications did not adhere to the LTE assumption. Minkowycz et al. [54] discovered a separate failure

region linked to a rapidly shifting surface heat flow. Recently, Al-Sumaily et al. [55] conducted an extensive review, summarizing the legitimacy of the LTE theory. His studies concluded that, in an LTNE scenario, there are always a variety of drives for giving more physical realism for accurate modelling of any practical problem.

Existing literature on forced convection in channels filled with porous material is reasonably comprehensive, focusing primarily on two-dimensional flow and temperature fields under LTNE conditions. However, studies incorporating magnetic fields, axial conduction, and dissipation in flows through porous-filled channels have yet to be widely reported, especially concerning heat transfer enhancement under LTNE, as far as the author's knowledge extends.

Current research endeavours have been initiated to address certain gaps in the literature. The specific aspects under investigation in this thesis are outlined in § 1.9, detailing the scope and objectives of the study.

1.9 Scope and Objective of the Study

The objective of the present study is to make available hydrodynamic and thermal characteristics for the laminar incompressible flow of a Newtonian fluid in channels filled with porous material in thermally developing region under the LTNE model. Effects of axial conduction and viscous dissipation form part of the investigation. Enhancement in the heat transfer under LTNE and its dependence on axial location and other non-dimensional parameters such as Darcy number, Biot number, Hatmann number, Brinkman number and the thermal conductivity ratio have been established.

The numerical solutions have been obtained for the following values of the parameters characterizing different problems studied. Darcy number: $0.001 \leq Da \leq 1.0$. Forchheimer number: $1 \leq F \leq 100$. Hartmann number: $0.1 \leq M \leq 10$. Biot number: $10 \leq Bi \leq 100$. When considering axial conduction, the Peclet number, Pe, lies in $5 \leq Pe \leq 100$. When axial conduction is disregarded, indicated by $A_c = 0$, Pe is absorbed in ξ^* and does not appear explicitly. The Brinkman number is $0.8 \leq Br \leq 100$ when viscous

dissipation is included. The thesis comprises six chapters, with Chapter 1 providing a comprehensive introduction to the research and a thorough literature review. It provides an overview of fluid flow and heat transfer within ducts containing porous materials, considering LTE model and LTNE model. It also concisely examines heat transfer phenomena under the LTNE model and offers a comprehensive survey of dissipation models applicable to porous media. Furthermore, the numerical approach employed in this thesis is detailed. An overview of appropriate dissipation models for porous media is presented, and the numerical scheme utilized throughout the thesis is explained. The sixth Chapter is the conclusion of the thesis. The flow field is assumed to be fully developed, and the thermal field is developing and is subjected to constant wall heat flux in Chapters 2 to 4.

The schematic model and coordinate system of the parallel plate channel filled with porous medium. The distance between the parallel plates is denoted by H, and T_e fluid enters the channel at a uniform temperature. Constant wall heat flux (q_w) is imposed on the channel walls, and the fluid flow through the porous region is governed by the Darcy-Brinkman-Forchheimer model. A magnetic field (B_o) is applied perpendicular to the channel walls, and the flow is characterized by laminar, incompressible, steady, unidirectional flow and a developing thermal field. Porous and fluid regions are in LTNE. The porous medium is uniform and exhibits isotropic properties. The factors include axial conduction and viscous dissipation. Furthermore, the thermophysical properties remain constant.

The following topics, which form the subject matter of chapters 2 to 5 of the present thesis, have been studied.

- Non-linear Flow and Heat Transfer of the Porous Filled Channel.
- Forced Convection Heat Transfer at the Entry Region of the Porous Filled Channel with Axial Conduction Effect.
- Forced Convection Heat Transfer at the Entry Region of the Porous Channel with Viscous Dissipation.
- Forced Convection Heat Transfer at the Entry Region of the Porous Channel with Axial Conduction and Viscous Dissipation.

The forced convection heat transfer in the context of laminar flow within a thermally developing region focusing on the influence of LTNE has been studied in Chapter 2. This investigation pertains to parallel plate channels fully submerged within a porous material. The channel walls are subjected to constant heat flux boundary conditions. The flow equation in the nonlinear flow model governs the Darcy-Brinkman-Forchheimer field, assuming unidirectional flow. Additionally, a transverse application of the magnetic field is imposed along the channel walls. The effect of Darcy number, Forchheimer number, Hartmann number, Biot number, and thermal conductivity ratio is discussed for the thermally developing region.

The intended research involves pursuing numerical solutions in Chapter 2 and the complete thesis for the two-model conservation of energy equations (LTNE model). These computations pose significant demands, even within the established velocity field framework. Researchers have effectively employed the Successive Accelerated Replacement (SAR) [29] scheme to address various problems. This methodology has seen widespread utilization by Satyamurty and Bhargavi [30] and Bhargavi and Sharath Kumar Reddy [31]. The present thesis has chosen the SAR scheme to obtain numerical solutions for investigated problems. Extensive numerical trials have been conducted, and the following values for the parameters involved have been found to be satisfactory. (a) The acceleration factor, $0.6 \leq \omega \leq 1.1$; (b) Error tolerance limit, $\varepsilon_t = 10^{-3}$, 10^{-4}, and 10^{-5}; (c) non-uniform divisions in the axial direction, $2000 \leq PD \leq 9000$; and d) Number of divisions in the normal direction, $60 \leq QD \leq 100$ (uniform) were considered in the study. The non-uniform grids have been generated in geometric progression (GP).

The numerical solutions presented are based on implementing the following parameter values, as determined through conducted numerical trials. a) $\omega \leq 1$; b) $\varepsilon_t = 10^{-5}$; c) $\xi^*_{fd} = 0.4$; d) $PD = 1000$ with $\Delta\xi^*_P$ generated in geometric progression with $s = 1/8$; and e) $QD = 90$ with $\Delta\eta = 1/90$ (ref., Chapter 2 §, 2.6.1).

In Chapter 2, the study presents outcomes concerning dimensionless temperature profiles in both fluid and porous phases for the wall temperature and the

local Nusselt number within the parallel plate channel. As normalized dimensionless axial distance increases, the local Nusselt number decreases and reaches the fully developed value. Notably, the local Nusselt number is influenced by a magnetic field and variations in thermal conductivity ratio. As the Biot number and thermal conductivity ratio grows, the local Nusselt number decreases. The effect of the Forchheimer number on the local Nusselt number is less effective. Hence, Darcy Brinkman's model for the flow model is considered in the subsequent chapters. A fully developed condition is also shown even when LTNE is used. Wall temperature increases as normalized axial distance, ξ^* increases for all Biot numbers, from being initially nonlinear to subsequently becoming linear for $\xi^* > 0.005$, which is the onset of a fully developed condition. It serves the purpose of the downstream boundary condition at the exit when axial conduction is used (elliptic PDE).

Chapter 3 delves into the impact of axial conduction on the forced convective heat transfer characteristics within a duct filled with porous material undergoing thermal development under LTNE. The influence of axial conduction is particularly pronounced at low Peclet numbers (*Pe*) across various Biot numbers (*Bi*). The axial conduction effect is negligible, i.e., $A_c = 0$, for a significant value of Peclet number, *Pe* (≥ 100) in the LTNE except very near the entry. Additionally, for high Biot numbers, LTNE tends to LTE. The dimensionless temperature based on the bulk mean temperature in the fluid and porous phases is invariant for axial distance. Local Nusselt number variation depends on the parameters, Darcy number, Biot number, Peclet number, and thermal conductivity ratio. Local Nusselt number decreases as thermal conductivities and Biot numbers increase. As the Darcy number increases, the local Nusselt number decreases. It reaches the clear fluid fully developed Nusselt number for a large Darcy number.

This Chapter (Chapter 4) employs the effect of two viscous dissipation models, the form drag model (FD model) and the clear fluid compatible (CFC model), at the thermal entrance. The thermal characteristics of fluid flow through a porous material immersed in a parallel plate channel have been studied. It was investigated numerically under LTNE. Flow is considered unidirectional and governed by the Darcy Brinkman

model porous area. Numerical solutions have been obtained for the thermal field. The increase in the Brinkman number, Biot number, and thermal conductivity ratio improves the temperature distribution. In contrast to the result in the form drag model, a significant value of the local Nusselt number is obtained in the CFC model. As a result, the clear fluid compatible model has better convectional heat transmission.

Axial conduction and viscous dissipation have an integrated impact on the thermally growing domain under the LTNE framework in a duct filled with saturated porous media. It explores the thermal characteristics of fluid flow through a porous medium confined within a channel defined by parallel plates. In this chapter, the clear fluid compatible (CFC) model is used since it has significantly increased heat transfer. The effect of Peclet number, Brinkman number, Biot number, and thermal conductivity ratio on temperature distribution and local Nusselt number are discussed. Due to decreased thermal diffusion via the fluid phase in the porous media, the local Nusselt number tends to drop under the LTNE in the presence of the Peclet number as the Brinkman number rises. It shortens the thermal entry length. In the presence of axial conduction and viscous dissipation, the local Nusselt number drops as the thermal conductivity ratio rises.

The summary and significant conclusions drawn from the present studies are presented in Chapter 6 of the thesis.

Chapter 2

Non-linear Flow and Heat Transfer of the Porous Filled Channel

2.1 Introduction

In the majority of cases explored in the literature, an underlying assumption has been made that the porous matrix and the fluid coursing through it exist in a state of LTE, $T_f = T_p = T$, signifying that T_f and T_p represent the temperatures of the fluid and porous phases, respectively. Under the LTE condition, it is presupposed that the disparity between the temperature averages across the fluid and porous phases is negligible. On a microscopic scale, it is imperative that the temperature and the heat flux rate at the interface between the fluid and porous phases remain equivalent. However, considering the average values over a representative elementary volume may not produce locally uniform temperatures for both phases. In such instances, the two phases are said to be in a state of LTNE.

This chapter aims to examine forced convection heat transfer in the context of laminar flow within a thermally developing region, focusing on the influence of LTNE. The investigation pertains to a parallel plate channel fully submerged within a porous material. The channel walls are subjected to constant heat flux boundary conditions. Within the nonlinear flow model, the flow field in the porous region is governed by the Darcy-Brinkman-Forchheimer equation, assuming unidirectional flow. Additionally, a transverse application of the magnetic field is imposed along the channel walls. Specific well-known parameters define the system, these being the Hartmann number (*M*), Darcy number (*Da*), Forchheimer number (*F*), thermal conductivity ratio (κ) and Biot number (*Bi*). SAR schemes have been applied to obtain numerical solutions. Plots are given for the dimensionless temperature profiles in the fluid and porous phases, wall temperature, and the local Nusselt number at the parallel plate channel, which has been

displayed. The magnetic field and the thermal conductivity ratio significantly affect the local Nusselt number.

2.2 Mathematical Model

The schematic model and coordinate system of the parallel plate channel filled with porous medium are shown in Fig. 2.1. The distance between the parallel plates is denoted by *H*, and the fluid enters the channel at a uniform temperature T_e (Fig. 2.1). Constant wall heat flux (q_w) is imposed on the channel walls. The fluid flow through the porous region is governed by the Darcy-Brinkman-Forchheimer model. A magnetic field (B_o) is applied perpendicular to the channel walls, and the flow is characterized by laminar, incompressible, steady, and unidirectional behavior. The flow field is assumed to be fully developed; hence, dp/dx^* is a constant and growing thermal field. Porous and fluid regions are in LTNE. The porous medium is uniform and exhibits isotropic properties. Negligible factors include heat generation, axial conduction, and thermal dispersion. Furthermore, the thermophysical properties remain constant.

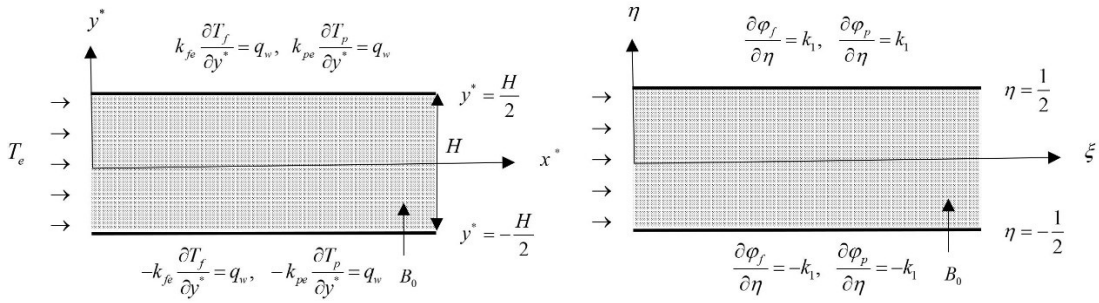

(a) Dimensional (b) Dimensionless

Fig. 2.1: Schematic model and the parallel plate channel coordinate system

Governing Equations

The momentum equation for the fluid flow across a porous medium by employing the Darcy Brinkman Forchheimer model is given by:

$$\mu_e \frac{d^2u}{dy^{*2}} - \frac{\mu}{K}u - \frac{\rho c_F}{\sqrt{K}}u^2 + \vec{J}\times\vec{B} = \frac{dp}{dx^*} \tag{2.1}$$

In Eq. (2.1), u denotes the velocity in the porous medium, and μ_e, μ, ρ, and K are effective viscosity, fluid viscosity, the density of the fluid, permeability in the porous region, and c_F is the Forchheimer coefficient, respectively. $\vec{B}$ is the magnetic induction vector of the applied uniform magnetic field and $\vec{J}$ is the electric current density. Assuming that there is no external electric field and that no internal factors, such as charge separation or polarization, are causing an induced electric field., $\vec{J} = \sigma\left(\vec{u} \times \vec{B}\right)$, where σ is electric conductivity, Lorentz force $F_L = \vec{J} \times \vec{B}$ and velocity vector $\vec{u}$ are opposite in direction and collinear. Hence $F_L = \vec{J} \times \vec{B} = -\sigma {B_0}^2 u$, where $B_0 = \left|\vec{B}\right|$. Thus, the governing equations given in Eq. (2.1) are reduced to:

$$\mu_e \frac{d^2 u}{dy^{*2}} - \frac{\mu}{K} u - \frac{\rho c_F}{\sqrt{K}} u^2 - \sigma {B_0}^2 u = \frac{dp}{dx^*} \tag{2.2}$$

The steady-state conservation of thermal energy equations of the fluid and porous phases are given by:

Fluid phase

$$\left(\rho C_p\right)\left(u_p \frac{\partial T_f}{\partial x^*}\right) = k_{fe} \frac{\partial^2 T_f}{\partial y^{*2}} + a_{pf} h_{pf} \left(T_p - T_f\right) \tag{2.3}$$

Porous phase

$$k_{pe} \frac{\partial^2 T_p}{\partial y^{*2}} - a_{pf} h_{pf} \left(T_p - T_f\right) = 0 \tag{2.4}$$

In Eqs. (2.3) and (2.4), ρ is density, C_p is the specific heat, T_f is the fluid phase temperature, T_p is the porous phase temperature, k_{fe} is the effective fluid thermal conductivity, k_{pe} is the effective porous thermal conductivity, respectively. a_{pe} is the interfacial area per unit volume of the porous media and h_{pf} is the porous-to-fluid heat transfer coefficient in the literature.

Boundary Conditions

Hydrodynamics boundary conditions are given by:

$$u = 0, \quad \text{at } y^* = \frac{H}{2}, -\frac{H}{2} \quad \left(\text{No-slip condition}\right) \tag{2.5}$$

Thermal boundary conditions are as follows:

$$\left.\begin{aligned} k_{fe}\frac{dT_f}{dy^*} = q_w, \;\; k_{pe}\frac{dT_p}{dy^*} = q_w \;\; \text{at } y^* = \frac{H}{2} \\ -k_{fe}\frac{dT_f}{dy^*} = q_w, \;\; -k_{pe}\frac{dT_p}{dy^*} = q_w \;\; \text{at } y^* = -\frac{H}{2} \end{aligned}\right\} \quad \left(\text{Heat flux condition}\right) \tag{2.6}$$

$$T_{f,p}\left(0, y^*\right) = T_e, \quad -\frac{H}{2} < y^* < \frac{H}{2} \quad \left(\text{Inlet condition}\right) \tag{2.7}$$

$$T_p = T_f = T_{interface} \quad \left(\text{Porous-fluid interface}\right) \tag{2.8}$$

In Eq. (2.8), the temperature at the porous-fluid interface is denoted by $T_{\text{interface}}$. At the porous-fluid contact, the temperatures of the two phases need to be locally equal. It differs from the LTE assumption, which assumes that the temperatures of the two phases are equal everywhere.

Dimensionless Variables

The following dimensionless variables are utilised to construct the governing equations, boundary condition, and porous-fluid interface condition {Eqs. (2.2) to (2.8)} dimensionless.

$$\left.\begin{aligned} \xi = \frac{x^*}{H}, \;\; \eta = \frac{y^*}{H}, \;\; U = \frac{u\mu}{\left(-\frac{dp}{dx^*}\right)H^2}, \;\; U_{avg} = \frac{u_{avg}\mu}{\left(-\frac{dp}{dx^*}\right)H^2} \\ \varphi_f = \frac{\left(T_f - T_e\right)}{\left(\frac{q_w H}{k_f}\right)}, \;\; \varphi_p = \frac{\left(T_p - T_e\right)}{\left(\frac{q_w H}{k_f}\right)} \end{aligned}\right\} \tag{2.9}$$

In Eq. (2.9), ξ and η are the dimensionless coordinates along the x^* and y^* directions. The dimensionless temperature and velocity are denoted by φ and *U*, respectively. The fluid and porous phases are designated by subscripts f and p, respectively. The average velocity across the channel is denoted by u_{avg}. The normalized axial distance, ξ^* can be defined as follows:

$$\xi^* = \frac{\xi}{Pe} \tag{2.10}$$

In Eq. (2.10), *Pe* is the Peclet number ($Pe = u_{avg} H / \alpha$, α is thermal diffusivity).

The governing equations (Eqs. (2.2) to (2.4)) in dimensional form become dimensionless form after applying the dimensionless variables are given by Eq. (2.9).

$$\frac{1}{\varepsilon}\frac{d^2U}{d\eta^2} - \left(\frac{1}{Da} + M^2\right)U - F\ U^2 + 1 = 0 \tag{2.11}$$

$$U^N(\eta)\frac{\partial \varphi_f}{\partial \xi^*} = \frac{1}{k_1}\frac{\partial^2 \varphi_f}{\partial \eta^2} + \frac{Bi\ \kappa}{k_1}\left(\varphi_p - \varphi_f\right) \tag{2.12}$$

$$\frac{\partial^2 \varphi_p}{\partial \eta^2} - Bi\left(\varphi_p - \varphi_f\right) = 0 \tag{2.13}$$

The equation (2.11) is the dimensionless form of conservation of momentum and Eqs. (2.12) and (2.13) are the dimensionless form of thermal energy equations in fluid and porous phases, respectively (LTNE model).

In Eq. (2.12), $U^N(\eta)$ is normalized velocity and can be calculated as follows:

$$U^N(\eta) = \frac{U(\eta)}{U_{avg}} \tag{2.14}$$

In Eq. (2.14), U_{avg}, the average velocity is calculated by the following formula:

$$U_{avg} = \int_{-1/2}^{1/2} U(\eta)\, d\eta \tag{2.15}$$

In Eqs. (2.11) to (2.13), *Da*, *M*, *F*, *Bi*, and κ denote the Darcy number, Hartmann number, Forchheimer number, Biot number, and effective thermal conductivity ratio, respectively; however, ε and k_1 represent the ratio between the viscosity of the fluid to the effective viscosity of the porous medium, and fluid thermal conductivity to effective fluid thermal conductivity, respectively and it can be defined as follows:

$$Da = \frac{K}{H^2} \tag{2.16}$$

$$M = \sqrt{\frac{\sigma B_0^2 H^2}{\mu_f}} \tag{2.17}$$

$$F = \frac{\rho c_F}{\sqrt{K}} \frac{H^4}{\mu^2} \left(-\frac{dp}{dx^*} \right) \tag{2.18}$$

$$Bi = \frac{a_{pf} h_{pf} H^2}{k_{pe}} \tag{2.19}$$

$$\kappa = \frac{k_{pe}}{k_{fe}} \tag{2.20}$$

$$\varepsilon = \frac{\mu}{\mu_e} \tag{2.21}$$

$$k_1 = \frac{k_f}{k_{fe}} \tag{2.22}$$

In Eq. (2.22), k_f is the thermal conductivity in the fluid region.

Dimensionless Boundary Conditions

Hydrodynamics boundary conditions are given by:

$$U = 0, \quad \text{at} \quad \eta = \frac{1}{2}, -\frac{1}{2} \tag{2.23}$$

Thermal boundary conditions are as follows:

$$\left.\begin{aligned} &\frac{\partial \varphi_f}{\partial \eta} = k_1, \quad \frac{\partial \varphi_p}{\partial \eta} = k_2 \qquad \text{at} \quad \eta = \frac{1}{2} \\ &\frac{\partial \varphi_f}{\partial \eta} = -k_1, \quad \frac{\partial \varphi_p}{\partial \eta} = -k_2 \quad \text{at} \quad \eta = -\frac{1}{2} \end{aligned}\right\} \tag{2.24}$$

$$\varphi_{f,p}(0,\eta) = 0, \quad \text{for} \quad -\frac{1}{2} < \eta < \frac{1}{2} \tag{2.25}$$

$$\varphi_f = \varphi_p = \varphi_{interface} \tag{2.26}$$

In Eq. (2.24), the ratio, k_2 is defined by:

$$k_2 = \frac{k_f}{k_{pe}} \tag{2.27}$$

2.3 Skin Friction Coefficient

At the wall location, $y^* = H/2$, the skin friction coefficient (C_{fp}) can be defined as:

$$C_{fp} = \frac{\mu_e \left(\frac{du}{dy^*} \right)\Big|_{y^* = H/2}}{\rho u_{ref}^2} \tag{2.28}$$

where u_{ref} is defined by:

$$u_{ref} = -\frac{\left(\frac{dp}{dx^*} \right) H^2}{\mu} \tag{2.29}$$

Using dimensionless variables from Eq. (2.9), Eq. (2.28) becomes,

$$Re\,C_{fp} = \frac{1}{\varepsilon}\frac{dU}{d\eta}\bigg|_{\eta=1/2} \tag{2.30}$$

where *Re,* the Reynolds number is given by:

$$Re = \frac{\rho u_{ref} H}{\mu} \tag{2.31}$$

2.4 Local Nusselt Number

The local heat transfer coefficient (h_ξ) is determined at the wall $y^* = H/2$ adjacent to the porous medium.

$$-k_{fe}\frac{\partial T_f}{\partial y^*}\bigg|_{y^*=\frac{H}{2}} = h_\xi\left(T_w - T_b\right) \tag{2.32}$$

In Eq. (2.32), the bulk mean temperature (T_b) is denoted as follows:

$$T_b = \frac{\int_{-H/2}^{H/2} uT_f dy^*}{\int_{-H/2}^{H/2} u dy^*} \tag{2.33}$$

Employing dimensionless variables {using Eq. (2.9)}, at $\eta = 1/2$, the local Nusselt number (Nu_ξ) is expressed by:

$$Nu_\xi = \frac{h_\xi(2H)k_1}{k_f} = \frac{-2\left(\frac{\partial\varphi_f}{\partial\eta}\right)\Big|_{\eta=1/2}}{\left(\varphi_w - \varphi^*\right)} = \frac{2}{\left(\varphi^* - \varphi_w\right)} \tag{2.34}$$

In Eq. (2.34), φ_w and φ^* are defined by:

$$\varphi_w = \frac{\left(T_w - T_e\right)}{q_w H / k_f} \tag{2.35}$$

$$\varphi^* = \frac{\left(T_b - T_e\right)}{q_w H / k_f} \tag{2.36}$$

where φ^* is evaluated by,

$$\varphi^* - \varphi_w\left(\xi^*\right) = \frac{\int_{-1/2}^{1/2} U^N(\eta)\left(\varphi_f - \varphi_w\right) d\eta}{\int_{-1/2}^{1/2} U^N(\eta)\, d\eta} \tag{2.37}$$

The dimensionless temperature based on the bulk mean temperature, φ_b is defined by

$$\varphi_b = \frac{T - T_e}{T_b - T_e} = \frac{\varphi}{\varphi^*} \tag{2.38}$$

2.5 Limiting Cases

Analytical expressions for dimensionless temperature and the Nusselt number for Case 1: Hartmann number, $M \neq 0.0$, Forchheimer number, $F = 0.0$, and Case 2: Hartmann number, $M = 0.0$, Forchheimer number, $F = 0.0$, for the fully developed thermal field are given for Darcy Brinkman Model. The procedure by Kays and Crawford [2] has been adopted to derive analytical solutions.

Case 1: $F = 0.0$, $M \neq 0.0$

Substituting $F = 0.0$ in Eq. (2.11), the dimensionless form Darcy Brinkman model is given by:

$$\frac{1}{\varepsilon}\frac{d^2U}{d\eta^2}-\left(\frac{1}{Da}+M^2\right)U+1=0 \tag{2.39}$$

Let the temperatures at the upper wall ($y^*=H/2$) be T_{wf} and T_{wp}. The corresponding dimensionless wall temperatures in fluid and porous phases, φ_{wf} and φ_{wp} are defined by:

$$\varphi_{wf}=\frac{\left(T_{wf}-T_e\right)}{\left(q_wH/k_f\right)},\quad \varphi_{wp}=\frac{\left(T_{wp}-T_e\right)}{\left(q_wH/k_f\right)} \tag{2.40}$$

Since the boundary conditions are of Neumann type, Eq. (2.24), constants cannot be evaluated using both Neumann type conditions. Hence, Eq. (2.12) and Eq. (2.13) are solved using the following Dirichlet boundary conditions discussed in Kays and Crawford [2].

$$\varphi_f\left(\pm\frac{1}{2}\right)=\varphi_{wf},\quad \varphi_p\left(\pm\frac{1}{2}\right)=\varphi_{wp} \tag{2.41}$$

The set of equations {Eqs. (2.12), (2.13), and (2.39)} are solved based on boundary conditions {Eqs. (2.23) and (2.41)}. The temperature profiles in the fluid and porous phases are expressed relative to φ_{wf} and φ_{wp}, respectively.

Since it is assumed that the thermal field is fully developed and constant flux boundary conditions are applied at the wall, $\left(\partial\varphi_f/\partial\xi^*\right)=\left(d\varphi^*/d\xi^*\right)$ becomes a constant, say λ.

The dimensionless temperatures in the fluid and porous phases and the fully developed Nusselt number expression for the Darcy Brinkman model, respectively, are given by:

The dimensionless temperature in fluid and porous phases:

$$\varphi_{wf}-\varphi_f(\eta)=\frac{\lambda k_1\left\{\begin{array}{l}2A_2^4\left\{e^{\frac{\sqrt{\kappa Bi}(1-2\eta)}{\sqrt{2}}}+e^{\frac{\sqrt{\kappa Bi}(1+2\eta)}{\sqrt{2}}}-e^{\sqrt{2\kappa Bi}}-1\right\}\\+\kappa BiA_2^2A_3\left[\kappa Bi\left(1-4\eta^2\right)\left(1-A_2^2\right)+8\right]\\+8\kappa BiA_3\left[A_4A_5\cosh\left[\eta A_2\right]-\kappa Bi\right]\end{array}\right\}}{8\kappa BiA_2A_3A_4A_7} \tag{2.42}$$

$$\varphi_{wp}-\varphi_p(\eta)=-\frac{\lambda k_1e^{\sqrt{\frac{\kappa Bi}{2}}}\left\{\begin{array}{l}A_5\cosh\left[\sqrt{\frac{\kappa Bi}{2}}\right]\left\{\begin{array}{l}A_4\cosh\left[\frac{A_2}{2}\right]\left\{\begin{array}{l}4A_2{}^2+8\kappa Bi\\+\kappa Bi\left(4\eta^2-1\right)A_2{}^2\end{array}\right\}\\-16\kappa^2Bi^2\cosh\left[\eta A_2\right]\end{array}\right\}\\+4A_2{}^4\cosh\left[\sqrt{2\kappa Bi}\eta\right]\end{array}\right\}}{8\kappa Bi\left(2\kappa Bi-A_2{}^2\right)A_2A_3A_7} \tag{2.43}$$

Fully developed Nusselt number:

$$\left(Nu_{fd}\right)_{DBM}=\frac{12\kappa BiDa^2A_7\sqrt{\varepsilon A_1}A_{11}{}^2+\left\{\frac{4\sqrt{\kappa Bi}\left(\varepsilon A_1-\kappa BiDa\right)A_{10}}{Da}-A_{16}\right\}}{\left\{-A_{11}\left\{\begin{array}{l}-6\sqrt{2}\left(e^{\sqrt{2\kappa Bi}}-1\right)\left(\varepsilon A_1\right)^{7/2}\\+\frac{1}{A_6\sqrt{\kappa Bi}}\left\{\begin{array}{l}12\kappa BiDa^{3/2}\left[2A_6A_{10}A_{15}+A_{12}A_{18}\right]\\+\sqrt{\varepsilon A_1}A_3\left\{\begin{array}{l}A_{17}\cosh\left[A_2\right]A_9^2+A_{14}\\-4\kappa BiDa\left(18+\kappa Bi\right)\varepsilon^2A_1{}^2\\+\left(6+\kappa Bi\right)\varepsilon^3A_1{}^3\end{array}\right\}\end{array}\right\}\end{array}\right\}\right\}} \tag{2.44}$$

Case 2: $F \neq 0.0$, $M = 0.0$

In the absence of the Hartmann number, M ($M = 0$), the velocity profiles match with the work done by Reddy and Bhargavi [217] for all the values of the Forchheimer number (F) for the channel filled with porous material.

The variation of $\left(Nu_{fd}\right)_{DBM}$ with *Bi* is shown in Figs. 2.2(a) to 2.2(c) for various values of Hartmann number, *M* at given values of effective thermal conductivity ratios (κ = 0.1, 1.0, and 10.0). Each value of κ and *M*, $\left(Nu_{fd}\right)_{DBM}$ increases and attains a maximum at a small value of *Bi* and then decreases. For each *Bi*, as *M* increases, $\left(Nu_{fd}\right)_{DBM}$ increases for every value of κ. The constants, A_i, i = 1,2,3, …, 18, appearing in Eqs. (2.42) to (2.44) are given in the Appendix.

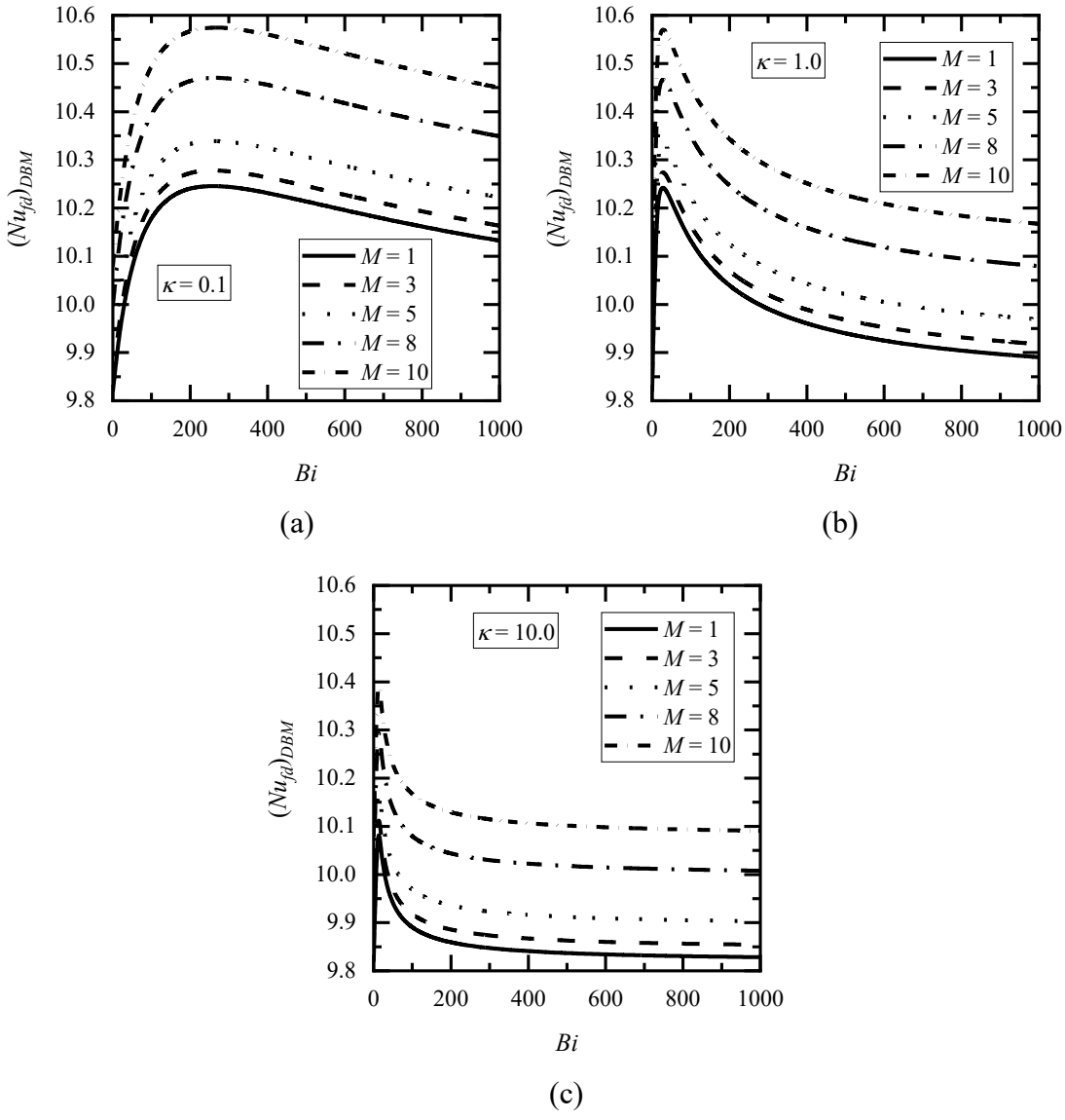

Fig. 2.2: Variation of fully developed Nusselt number, $\left(Nu_{fd}\right)_{DBM}$ with Biot number, *Bi*, for various values of Hartmann number, *M* for (a) κ = 0.1, (b) κ = 1.0, and (c) κ = 10.0 at Darcy number, *Da* = 0.005

2.6 Numerical Methodology: Successive Accelerated Replacement (SAR)

The employment of the SAR scheme is discussed in Satyamurty and Bhargavi [74], Marpu and Satyamurty [211], and Reddy and Bhargavi [217]}:

Let *PD* and *QD* represent the number of divisions in ξ and η directions, respectively, while $\Delta\xi^*$ and $\Delta\eta$ represent the width in ξ and η directions. The errors $\bar{U}$ and $\bar{\varphi}_f$ in the fluid phase and $\bar{\varphi}_p$ in the porous phase are provided in finite difference form.

Following discretization of the governing equations Eqs. (2.11) to (2.13) with uniform mesh in η-direction and non-uniform mesh in ξ-direction, the following equations are obtained:

$$\bar{U}(Q)=\frac{1}{\varepsilon}\frac{U(Q-1)-2U(Q)+U(Q+1)}{(\Delta\eta)^2}-\left(\frac{1}{Da}+M^2\right)U(Q)-\left[U(Q)\right]^2F+1 \quad (2.45)$$

$$\bar{\varphi}_f(P,Q)=U(Q)\left[\frac{\varphi_f(P,Q)-\varphi_f(P-1,Q)}{\xi(P)-\xi(P-1)}\right]-\frac{Bi\ \kappa}{k_1}\left[\varphi_p(P,Q)-\varphi_f(P,Q)\right]$$
$$-\frac{1}{k_1}\left[\frac{\varphi_f(P,Q+1)-2\varphi_f(P,Q)+\varphi_f(P,Q-1)}{(\Delta\eta)^2}\right] \quad (2.46)$$

$$\bar{\varphi}_p(P,Q)=\left[\frac{\varphi_p(P,Q-1)-2\varphi_p(P,Q)+\varphi_p(P,Q+1)}{(\Delta\eta)^2}\right]$$
$$-Bi\left[\varphi_p(P,Q)-\varphi_f(P,Q)\right] \quad (2.47)$$

where $\Delta\xi^*$ is the ξ -direction uniform grid size specified by, $\xi(P)-\xi(P-1)$.

$$\Delta\xi^*=\frac{\xi^*_{fd}}{PD} \quad (2.48)$$

where ξ^*_{fd} denotes the fully developed normalized length,

$$\Delta\eta = \frac{1}{QD} \tag{2.49}$$

The following derivatives are required to correct the profile for U, φ_f and φ_p

$$\frac{d\bar{U}(Q)}{dU(Q)} = -\frac{2}{\varepsilon(\Delta\eta)^2} - 2U(Q)F - \left(\frac{1}{Da} + M^2\right) \tag{2.50}$$

$$\frac{\partial\bar{\varphi}_f(P,Q)}{\partial\varphi_f(P,Q)} = \frac{U(Q)}{\xi(P)-\xi(P-1)} + \frac{2}{k_1(\Delta\eta)^2} + \frac{Bi\ \kappa}{k_1} \tag{2.51}$$

$$\frac{\partial\bar{\varphi}_p(P,Q)}{\partial\varphi_p(P,Q)} = -\left[\frac{2}{(\Delta\eta)^2} + Bi\right] \tag{2.52}$$

Discretized boundary conditions

$$\left.\begin{aligned}\varphi_f(P,QD+1) &= \frac{2k_1\ \Delta\eta + 4\varphi_f(P,QD) - \varphi_f(P,QD-1)}{3}\\ \varphi_p(P,QD+1) &= \frac{2k_2\ \Delta\eta + 4\varphi_p(P,QD) - \varphi_p(P,QD-1)}{3}\end{aligned}\right\} \quad \text{(Upper wall)} \tag{2.53}$$

$$\left.\begin{aligned}\varphi_f(P,1) &= \frac{2k_1\ \Delta\eta + 4\varphi_f(P,2) - \varphi_f(P,3)}{3}\\ \varphi_p(P,1) &= \frac{2k_2\ \Delta\eta + 4\varphi_p(P,2) - \varphi_p(P,3)}{3}\end{aligned}\right\} \quad \text{(Lower wall)} \tag{2.54}$$

Inlet boundary condition is as follows:

$$\varphi_{f,p}(1,Q) = 0 \ \text{ for } \ 1+\left(\frac{QD}{2}\right) < Q < (1+QD) \tag{2.55}$$

The discretized form of the product of Reynolds number (*Re*) and the skin friction coefficient (C_{fp}) can be obtained using three-point backward finite different formulas and given by:

$$ReC_{fp} = \frac{3U(Q+1) - 4U(Q) + U(Q-1)}{2\Delta\eta} \tag{2.56}$$

2.6.1 Numerical Trials

Numerical trials have been done for the following equations under the local thermal equilibrium (LTE) model.

Darcy Brinkman model (substituting $F = 0$ and $M = 0$ in Eq. (2.11))*:*

$$\frac{1}{\varepsilon}\frac{d^2U}{d\eta^2} - \frac{1}{Da}U + 1 = 0 \tag{2.57}$$

Energy equation:

$$U(\eta)\frac{\partial\varphi_f}{\partial\xi^*} = \frac{1}{k_1}\frac{\partial^2\varphi_f}{\partial\eta^2} \tag{2.58}$$

Boundary conditions are given by:

$$U\big|_{\eta=\frac{1}{2}} = 0, \quad \left.\frac{dU}{d\eta}\right|_{\eta=0} = 0 \tag{2.59}$$

$$\left.\frac{\partial\varphi_f}{\partial\eta}\right|_{\eta=\frac{1}{2}} = k_1, \quad \left.\frac{\partial\varphi_f}{\partial\eta}\right|_{\eta=0} = 0 \tag{2.60}$$

Appropriate values for the parameters that provide convergent solutions must be identified to generate reasonable numerical solutions. The error tolerance limit, acceleration factor, and the number of grids in ξ^*, and η directions are *PD* and *QD*,

respectively the parameters. Numerical trials are performed with $10^{-3} \le \varepsilon_t \le 10^{-5}$, $0.6 \le \omega \le 1.1$, $2000 \le PD \le 9000$, and $60 \le QD \le 100$ for $Da = 0.005$.

Number of Grids, Uniform Spacing

Table 2.1 shows Nu_ξ values for QD = 60, 70, 80, 90, and 100 with PD = 2000, 4000, 6000, 8000, and 9000. From Table 2.1, the value of Nu_ξ = 9.816 with QD = 90 found in the numerical trials at ξ^* = 0.4, coincides with the equivalent fully developed value of 9.8156, which is obtained analytically. It shows that QD = 90 grids is appropriate. When uniform grids QD = 90 and PD = 8000 are used, the values of local Nusselt numbers do not change appreciably.

Acceleration factor, ω

To determine suitable values for the acceleration factor, ω, sufficiently large PD = 8000, QD = 90, and uniform mesh have been chosen. The error tolerance limit has been fixed at 10^{-4} values at different locations, from the inlet to the fully developed region. It has been selected as the criterion for arriving at a suitable value for the acceleration factor ω. Values of Nu_ξ at different ξ^* and ω are given in Table 2.2.

The acceleration factor is obtained from:

$$\omega = \left(\frac{\varepsilon_t}{\bar{\varphi}^k_{P,Q}} \right) \varphi^k_{P,Q} \left(\frac{\partial \bar{\varphi}^{-k}_{P,Q}}{\partial \varphi_{P,Q}} \right) \tag{2.61}$$

The number of iterations, NI, decreased from 14592 to 2726 as ω increased from 0.6 to 1.1. The computational time, directly proportional to the number of iterations, decreases as ω increases. As expected, the converged values are independent of the acceleration factor.

Error tolerance limit

Similar to the numerical trials described above, numerical solutions have been obtained for values of error tolerance limit, ε_t = 10^{-3}, 10^{-4}, and 10^{-5} with PD = 8000, QD = 90,

choosing ω as per Eq. (2.61). Values of different ε_t at different values are given in Table 2.3. As noted, concerning the acceleration factor, the thermal field is fully developed for $\xi^* \geq 0.4$. The fully developed values obtained with $\varepsilon_t = 10^{-4}$ are very close to the analytically obtained values of $Nu_\xi = 9.8156$ (see Fig. 10, Satyamurty and Bhargavi [74]) for $Da = 0.005$ and $\delta_p = 1.0$, $\varepsilon_t = 10^{-4}$ is an acceptable value for the error tolerance limit.

Non-uniform grids generation (Bhargavi and Reddy [75])*:*

The following formula is used to construct uniform grids:

$$\xi(i) = (i-1)\Delta\xi^* \tag{2.62}$$

The axial distance is increased in a geometric progression to produce non-uniform grids. Let $\Delta\xi^*_P$ be the rise in geometric progression with (1+*d*) as a common ratio, and in geometric progression, the first term $\Delta\xi^*_1$ is given by,

$$\Delta\xi^*_P = (1+d)^{(P-1)}\,\Delta\xi^*_1 \tag{2.63}$$

Let the first non-uniform grid width of $\Delta\xi^*_1$ be defined by:

$$\Delta\xi^*_1 = s\ \Delta\xi^* \tag{2.64}$$

where $\Delta\xi^*$ is uniform cell width and *s* is a constant less than unity.

A common ratio of (1+*d*), can be determined as follows:

$$\xi^*_{fd} = \Delta\xi^*_1\left(\frac{(1+d)^{PD}-1}{d}\right) \tag{2.65}$$

Table 2.1: Uniform mesh and grid independence test: Nu_{ξ} at various ξ^* for $Da = 0.005$, $\varepsilon_t = 10^{-4}$ and $\omega = 0.8$ (NI = Number of Iterations)

QD	PD	ξ^*									NI
		0.0016	**0.0050**	**0.0100**	**0.0300**	**0.0500**	**0.1000**	**0.150**	**0.2000**	**0.4000**	
60	2000	28.5561	19.0660	15.2571	11.3921	10.4248	9.8939	9.8343	9.8243	9.8044	3343
	4000	28.3332	19.0178	15.2371	11.3864	10.4218	9.8933	9.8342	9.8243	9.8046	3845
	6000	28.2595	19.0018	15.2304	11.3845	10.4208	9.8931	9.8341	9.8243	9.8047	4349
	8000	28.2595	19.0018	15.2304	11.3845	10.4208	9.8931	9.8341	9.8243	9.8047	4349
	9000	28.2105	18.9632	15.2260	11.3832	10.4201	9.8929	9.8340	9.8243	9.7788	5106
70	2000	28.2976	18.9745	15.2090	11.3753	10.4151	9.8895	9.8315	9.8227	9.8165	4299
	4000	28.0791	18.9269	15.1892	11.3697	10.4121	9.8889	9.8314	9.8227	9.8165	4800
	6000	28.0069	18.9111	15.1826	11.3678	10.4111	9.8887	9.8314	9.8226	9.8165	5303
	8000	28.0069	18.9111	15.1826	11.3678	10.4111	9.8887	9.8314	9.8226	9.8165	5303
	9000	27.9590	18.9283	15.1782	11.3665	10.4104	9.8885	9.8313	9.8226	9.8165	6059
80	2000	28.1172	18.9120	15.1764	11.3640	10.4085	9.8865	9.8296	9.8214	9.8166	5387
	4000	27.9023	18.8649	15.1567	11.3584	10.4056	9.8859	9.8295	9.8214	9.8166	5886
	6000	27.8313	18.8493	15.1502	11.3566	10.4046	9.8857	9.8295	9.8214	9.8166	6389
	8000	27.7958	18.8414	15.1469	11.3556	10.4040	9.8855	9.8294	9.8214	9.8165	6893
	9000	27.7841	18.8115	15.1458	11.3553	10.4039	9.8855	9.8294	9.8214	9.8165	7145
90	2000	27.9871	18.8676	15.1533	11.3561	10.4039	9.8843	9.8282	9.8205	9.8165	6604
	4000	27.7748	18.8209	15.1337	11.3505	10.4009	9.8837	9.8281	9.8205	9.8165	7101
	6000	27.7047	18.8053	15.1272	11.3486	10.3999	9.8835	9.8281	9.8205	9.8165	7605
	8000	27.6581	18.7678	15.1228	11.3473	10.3992	9.8834	9.8280	9.8205	9.8165	8109
	9000	27.6488	18.7929	15.1220	11.3471	10.3991	9.8833	9.8280	9.8205	9.8165	8360
100	2000	27.8903	18.8348	15.1363	11.3502	10.4005	9.8827	9.8271	9.8198	9.8164	7946
	4000	27.6802	18.7884	15.1168	11.3446	10.3975	9.8821	9.8270	9.8198	9.8164	8442
	6000	27.6108	18.7729	15.1103	11.3427	10.3965	9.8819	9.8270	9.8198	9.8164	8946
	8000	27.6547	18.7657	15.1220	11.3475	10.3998	9.8838	9.8280	9.8208	9.8165	9450
	9000	27.5555	18.7906	15.1225	11.3463	10.3987	9.8838	9.8270	9.8108	9.8164	9702

Table 2.2: Nu_{ξ} at different ξ^* for different values of the acceleration factor, ω, for $PD = 8000$, $QD = 90$ and $\varepsilon_t = 10^{-4}$ for $Da = 0.005$

ω	Nu_{ξ} at different ξ^*									NI
	0.0006	**0.0010**	**0.0050**	**0.0100**	**0.0300**	**0.1000**	**0.1500**	**0.2000**	**0.4000**	
0.6	39.3998	32.6986	18.7975	15.1239	11.3476	9.8834	9.8280	9.8205	9.8165	14592
0.8	39.3998	32.6986	18.7975	15.1239	11.3476	9.8834	9.8280	9.8205	9.8165	8108
1.0	39.3998	32.6986	18.7975	15.1239	11.3476	9.8834	9.8280	9.8205	9.8165	4177
1.1	39.3998	32.6986	18.7975	15.1239	11.3476	9.8834	9.8280	9.8205	9.8164	2726
1.2	Did not converge									

Table 2.3: Nu_ξ at different ξ^* for different values of the error tolerance limit, ε_t, for PD = 8000, QD = 90, for Da = 0.005, ω = 0.8

ε_t	Nu_ξ at different ξ^*									*NI*
	0.0006	**0.0010**	**0.0050**	**0.0100**	**0.0300**	**0.1000**	**0.1500**	**0.2000**	**0.4000**	
10^{-3}	39.7049	32.8921	18.8414	15.1469	11.3556	9.8853	8.7034	10.7295	10.7296	2426
10^{-4}	39.7049	32.8921	18.8414	15.1469	11.3556	9.8855	9.8294	9.8214	9.2586	6313
10^{-5}	39.7049	32.8921	18.8414	15.1469	11.3556	9.8855	9.8294	9.8214	9.7615	6893

Table 2.4: The constant values of d and s for PD = 500, 1000, and 2000

s	values of d for PD		
	500	**1000**	**2000**
1/4	0.00469119	0.00234112	0.00116945
1/8	0.00666086	0.00332264	0.00165938
1/16	0.00850544	0.00424098	0.00211757

Table 2.5: Using GP, comparison of Nu_ξ at various ξ^* values for uniform and non-uniform grids with QD = 90, Da = 0.005, ω = 0.8, and $\varepsilon_t = 10^{-5}$

PD		Nu_ξ at different ξ^* values									*NI*
	CPU Time	**0.0016**	**0.0050**	**0.0100**	**0.0300**	**0.050**	**0.1000**	**0.150**	**0.2000**	**0.4000**	
1000 non-uni	1m24.682s	27.9594	18.8852	15.1732	11.3649	10.4083	9.8868	9.8297	9.8215	9.8166	5191
2000 non-uni	3m1.092s	27.8946	18.8667	15.1444	11.3607	10.4056	9.8860	9.8296	9.8215	9.8166	5422
3000 non-uni	12m47.181s	27.6293	18.8177	15.1532	11.3558	10.4055	9.8863	9.8296	9.8214	9.8165	15754
8000 Uniform	16m9.204s	27.8313	18.8493	15.1502	11.3566	10.4046	9.8857	9.8295	9.8214	9.8166	99436

Eq. (2.65) determines d for a specific value of s, ξ^*_{fd} = 0.4, and PD. PD = 2000, ξ^*_{fd} = 0.4, and a uniform grid size of $\Delta\xi^*$ = 0.0002 generated a suitable solution. For ξ^* = 0.4, if $\Delta\xi^*_1$ = 0.0002 is chosen as the first non-uniform grid, Table 2.4 shows the constant d and s values for PD = 1000 and 2000. The value of s is selected from Table 2.4 as 1/8. The formula given in Eq. (2.64) is used in the generation of non-uniform grids. The grids in geometric progression have been created as detailed above for $\Delta\xi^*_P$.

Table 2.5 shows the Nu_ξ values for Da = 0.005 at various ξ^* values. Table 2.5 also shows the results achieved with 8000 uniform grids.

The Nu_ξ values obtained with non-uniform grids formed in geometric progression with PD = 2000 are close to those obtained with 8000 uniform grids at various ξ^*. The reduction in computational time is substantial.

The following values for the parameters involved have been established to be satisfactory based on numerical experiments. (a) The acceleration factor: $0.6 \leq \omega \leq 1.1$. However, under-relaxation has been preferred and $\omega < 1$ has been employed, (b) $\varepsilon_t = 10^{-4}$, (c) QD = 90 with $\Delta\eta$ = 1/90, and (d) PD = 2000.

2.7 Numerical Results and Discussions

The SAR methodology has been widely used in the literature (Bhargavi and Reddy [75], Marpu and Satyamurty, [211], and Marpu [214]) to generate numerical solutions to Eqs. (2.11) to (2.13) using finite difference expressions to Eqs. (2.45) to (2.47) and the derivatives, to Eqs. (2.50) to (2.52) and the boundary conditions and to Eqs. (2.53) to (2.55). It is taken that $k_1 = k_f / k_{fe} = 1$, $k_2 = k_f / k_{pe} = 1$ and $\varepsilon = \mu / \mu_{eff} = 1$. $0.001 \leq Da \leq 0.1$, $1 \leq F \leq 100$, $0.5 \leq M \leq 65$, and $10 \leq Bi \leq 100$, while $0.1 \leq \kappa \leq 10$ are the ranges used for the remaining parameters. These ranges of parameters are also used in the literature (ref., [29], [37], and [82]).

2.7.1 Hydrodynamics Field

The velocity profiles and skin friction coefficient for flow through a porous material-filled channel have been examined in this section.

Velocity

Figures 2.3(a, b) and 2.4(a, b) showcase the dimensionless velocity profiles for various Hartmann number (M) values at Da = 0.01 and Da = 0.1, respectively. The Forchheimer numbers (F) are set to 1 and 100, respectively, as indicated in the figures. These velocity

profiles visually present the velocity distribution within the channel, highlighting the effects of the Hartmann and Forchheimer numbers on the flow characteristics.

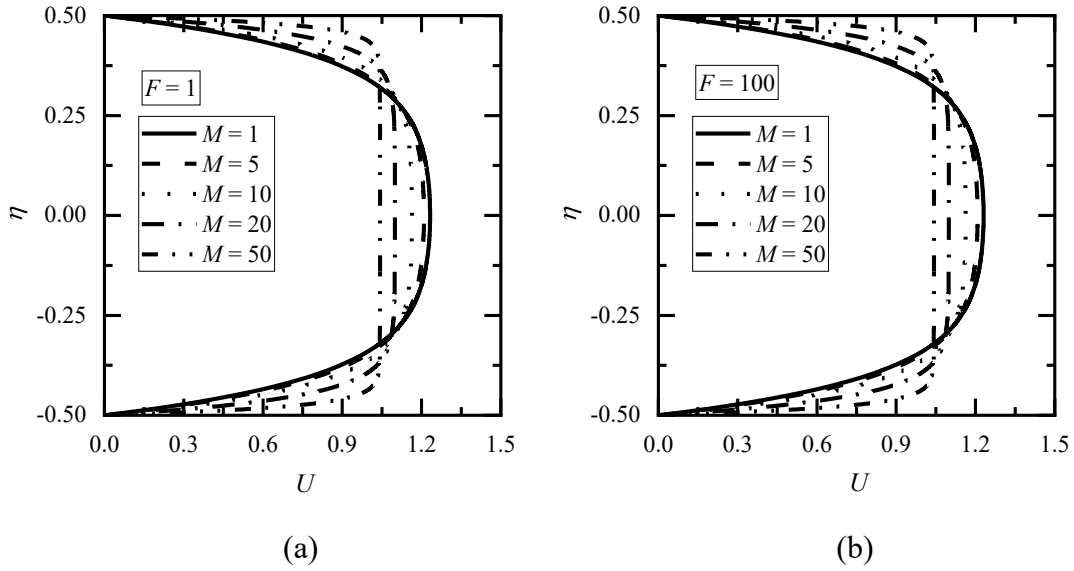

Fig. 2.3: Effect of velocity profiles for various Hartmann numbers, M values for (a) $F = 1$, and (b) $F = 100$ at $Da = 0.01$

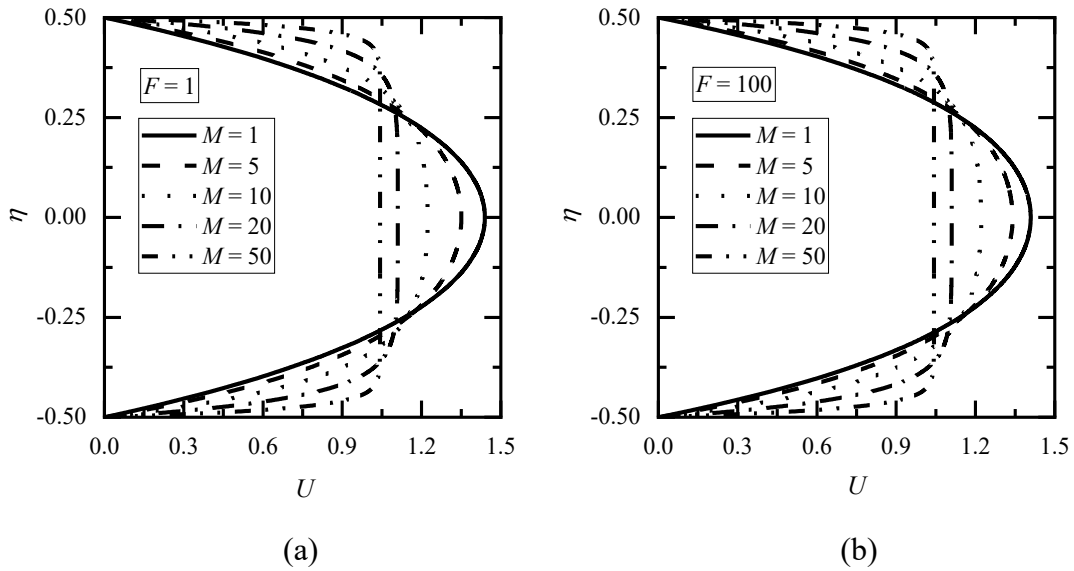

Fig. 2.4: Effect of velocity profiles for various Hartmann numbers, M values for (a) $F = 1$, and (b) $F = 100$ at $Da = 0.1$

From the figures, dimensionless velocity U attains a maximum at the center of the channel ($\eta = 0$). From Fig. 2.3, it can be observed that as the magnetic field becomes more significant in regulating fluid motion, the value of dimensionless velocity, U, falls with an increase in Hartmann number, M. The high Hartmann number, which denotes the dominance of magnetic forces over viscous forces, explains this.

Fluid mobility is often suppressed when magnetic forces are dominant. For any Forchheimer number, this holds. However, the rise in the parameter, F, signifies that the resistive forces are generated within the system. It leads to a decrease in the fluid's motion; consequently, the velocity decreases with an increase of F for each value of M, as shown in Figs. 2.3 and 2.4. By comparing Figs. 2.3 and 2.4, it is clear that as the Darcy number, Da, increases, U increases. For a significant value of Da, the increase in the velocity is more significant because, for a prominent Da, the porous region begins to behave like a clear fluid region. These velocity profiles match those reported in Reddy and Bhargavi [217] for channel-filled porous regions without Hartmann numbers ($M = 0$).

Skin friction coefficient

Figures 2.5 and 2.6 illustrate the variation of the product of skin friction coefficient and Reynolds number profiles (ReC_{fp}) with Da at distinct Forchheimer numbers (F = 1, 5, 10, 50, and 100) and Hartmann numbers (M = 0.5, 1.0, 2.0, 3.0, and 4.0). It may be observed from Figs. 2.5 and 2.6 that Da grows, drops, and approaches 6 (the value in the clear fluid channel). However, as Da value increases, the value of ReC_{fp} diminishes, and it tends to 6. The value $ReC_{fp} = 6$ is obtained in a clear fluid channel. However, this fact has been discussed in Bejan [5]. Additionally, at a given Da, the value of ReC_{fp} increases with the Forchheimer number (F) and the Hartmann number (M).

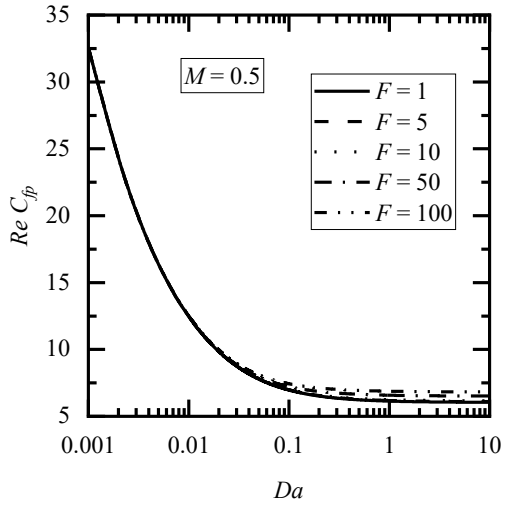

Fig. 2.5: Effect of Darcy number, Da for various values of Forchheimer numbers, F at $M = 0.5$

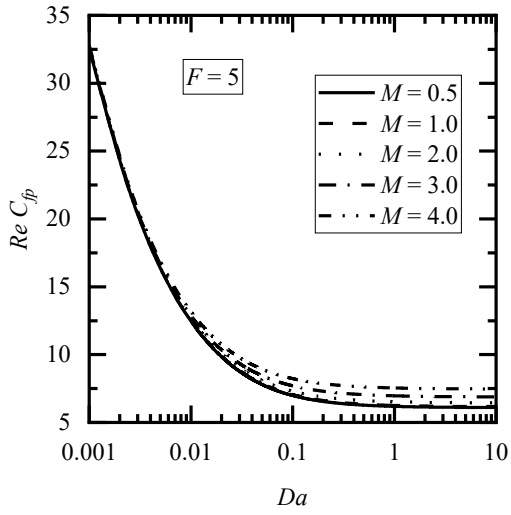

Fig. 2.6: Effect of Darcy number, Da for various values of Hartmann numbers, M at $F = 5$

2.7.2 Thermal Field

The dimensionless temperature profiles in both phases, fluid and porous, dimensionless temperature based on bulk mean temperature, wall temperature, and the local Nusselt numbers for flow through the porous-filled channel, are examined in the present section.

Dimensionless temperature profiles for the fluid phase, φ_f and porous phase, φ_p for Biot number, Bi = 10, Forchheimer number, F = 1, Darcy number, Da = 0.001, and thermal conductivity ratio, κ = 0.1 for different values of ξ^* are shown in Figs. 2.7(a, b) and 2.8(a, b) at Hartmann number, M = 0.5 and 65, respectively. A similar type of plot is given for large values of Forchheimer number (F = 100), Biot number (Bi = 100), and thermal conductivity ratio (κ = 10.0) given in Figs. 2.9, 2.10, and 2.11, respectively. From Figs. 2.7 to 2.11, φ_f, and φ_p increase with an increase of ξ^*. This fact is true in the LTE model as discussed in the literature (ref., [37], [115], and [116]).

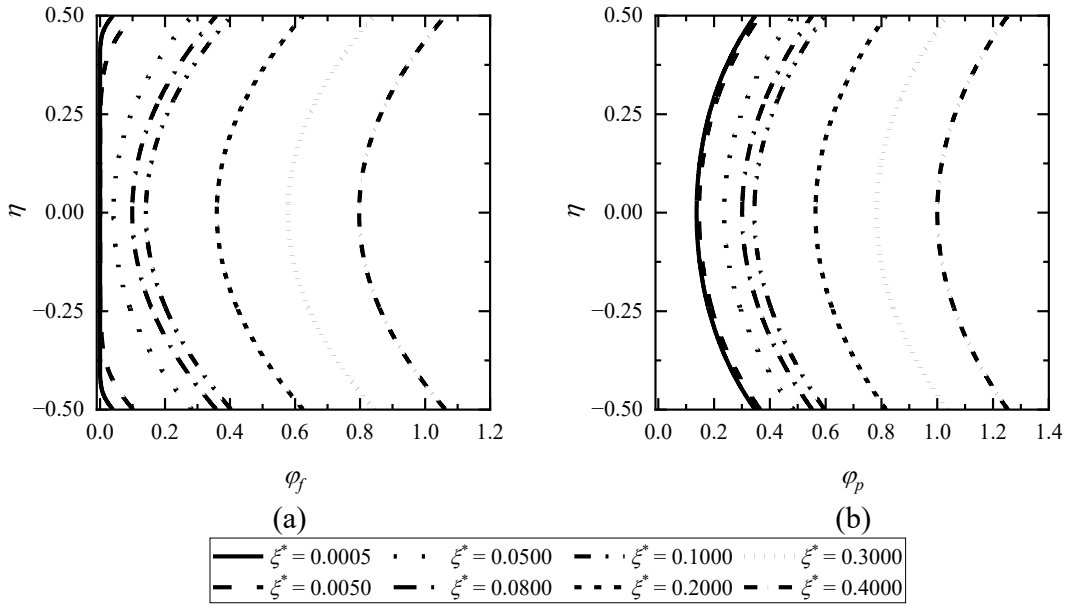

Fig. 2.7: Impact of (a) φ_f and (b) φ_p for distinct ξ^* values at Bi = 10, κ = 0.1, F = 1, Da = 0.001, and M = 0.5

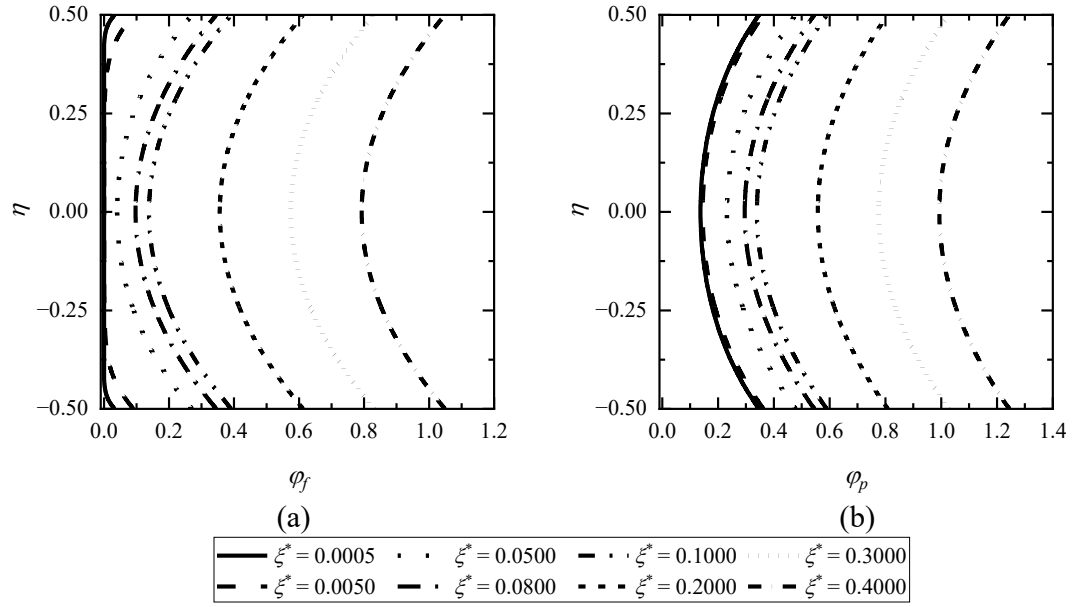

Fig. 2.8: Impact of (a) φ_f and (b) φ_p for distinct ξ^* values at $Bi = 10$, $\kappa = 0.1$, $F = 1$, $Da = 0.001$, and $M = 65$

From Figs. 2.7(a, b) and 2.8(a, b), as Hartmann number (M) increases, φ_f, and φ_p decrease numerically for all the values of ξ^*. Upon comparison of Figs. 2.7(a, b) and 2.9(a, b), it is evident that as Forchheimer number (F) increases, temperature decreases, but has a minimal effect on the temperature profiles of φ_f, and φ_p.

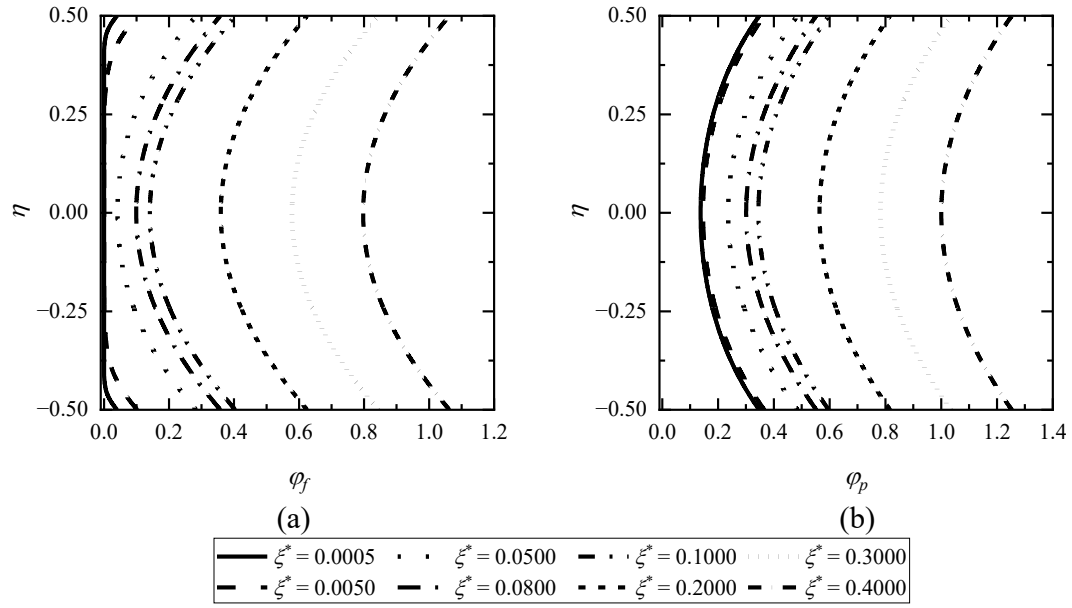

Fig. 2.9: Impact of (a) φ_f and (b) φ_p for distinct ξ^* values at $Bi = 10$, $\kappa = 0.1$, $F = 100$, $Da = 0.001$, and $M = 0.5$

By comparing Figs. 2.7(a, b) and 2.10(a, b), a clear pattern emerges. As the Biot number (*Bi*) increases from 10 to 100, the fluid phase temperature, φ_f increment becomes less pronounced. In contrast, porous phase temperature, φ_p shows a decreasing trend for each value of ξ^*, eventually approaching the temperature in the fluid region under LTE. It implies that when the Biot number is large, the system transitions from LTNE to LTE. The observed behaviour of approaching LTE as the Biot number increases holds for all values of Hartmann number, Forchheimer number, and Darcy number. Regardless of the specific values of these parameters, the trend of moving towards LTE with higher Biot numbers remains consistent throughout the analysis.

To see the effect of the thermal conductivity ratio, $\kappa \left(= k_{pe} / k_{fe}\right)$, plots are given for a significant value of κ (κ = 10). Fig. 2.11 indicates a more substantial temperature increment in the temperature profiles of φ_f, and φ_p for larger values of κ. As κ increases, the temperature variations become more pronounced in both φ_f, and φ_p. Furthermore, upon comparing Figs. 2.7(a, b) with 2.11(a, b), it can be observed that as the thermal conductivity ratio, κ, increases, both φ_f, and φ_p show an increment. This increase in φ_f, and φ_p is attributed to the rise in the effective thermal conductivity of the porous medium as κ increases. The higher thermal conductivity ratio enhances the overall heat transfer within the system, resulting in elevated temperature profiles for φ_f, and φ_p. From Figs. 2.7 to 2.11, it can also be observed that the temperature in a porous phase, φ_p is larger than in a fluid phase φ_f. This is due to the LTNE condition.

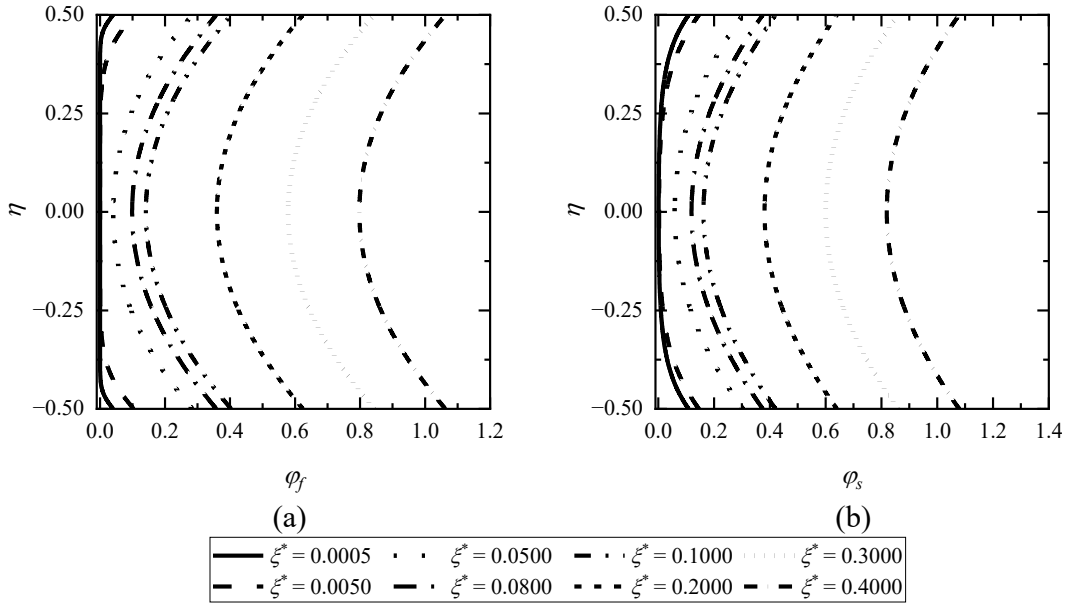

Fig. 2.10: Impact of (a) φ_f and (b) φ_p for distinct ξ^* values at $Bi = 100$, $\kappa = 0.1$, $F = 1$, $Da = 0.001$, and $M = 0.5$

To see the effect of the thermal conductivity ratio, $\kappa \left(= k_{pe} / k_{fe}\right)$, plots are given for a significant value of κ ($\kappa = 10$). Fig. 2.11 indicates a more substantial temperature increment in the temperature profiles of φ_f, and φ_p for larger values of κ. As κ increases, the temperature variations become more pronounced in both φ_f, and φ_p. Furthermore, upon comparing Figs. 2.7(a, b) with 2.11(a, b), it can be observed that as the thermal conductivity ratio, κ, increases, both φ_f, and φ_p show an increment. This increase in φ_f, and φ_p is attributed to the rise in the effective thermal conductivity of the porous medium as κ increases. The higher thermal conductivity ratio enhances the overall heat transfer within the system, resulting in elevated temperature profiles for φ_f, and φ_p. From Figs. 2.7 to 2.11, it can also be observed that the temperature in a porous phase, φ_p is more significant than in a fluid phase φ_f. This is due to the LTNE condition.

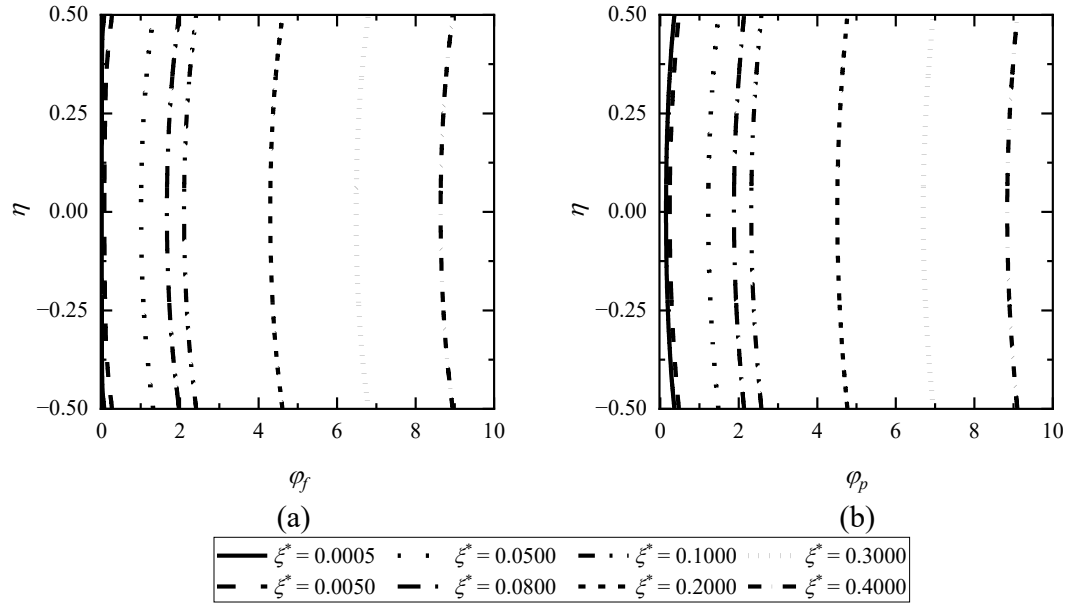

Fig. 2.11: Impact of (a) φ_f and (b) φ_p for distinct ξ^* values at $Bi = 10$, $\kappa = 10.0$, $F = 1$, $Da = 0.001$, and $M = 0.5$

Dimensionless temperature based on bulk mean temperature in the fluid phase and porous phase:

To validate the fully developed condition for a channel filled with porous region under LTNE, dimensionless temperature based on bulk mean temperature, φ_b is given in Fig. 2.12 for $Da = 0.001$, $\kappa = 0.1$, $F = 1$, and $Bi = 10$ for (a) $M = 0.5$, and (b) $M = 10$. From Fig. 2.12, it is clear that it tends to zero for large $\xi^* \geq 0.35$ for any F, M, Bi, κ and Da. It means that φ_b is invariant with respect to ξ^* for large ξ^*, which is a fully developed condition. This type of validation is available in Repaka and Satyamurty [73] for LTE model.

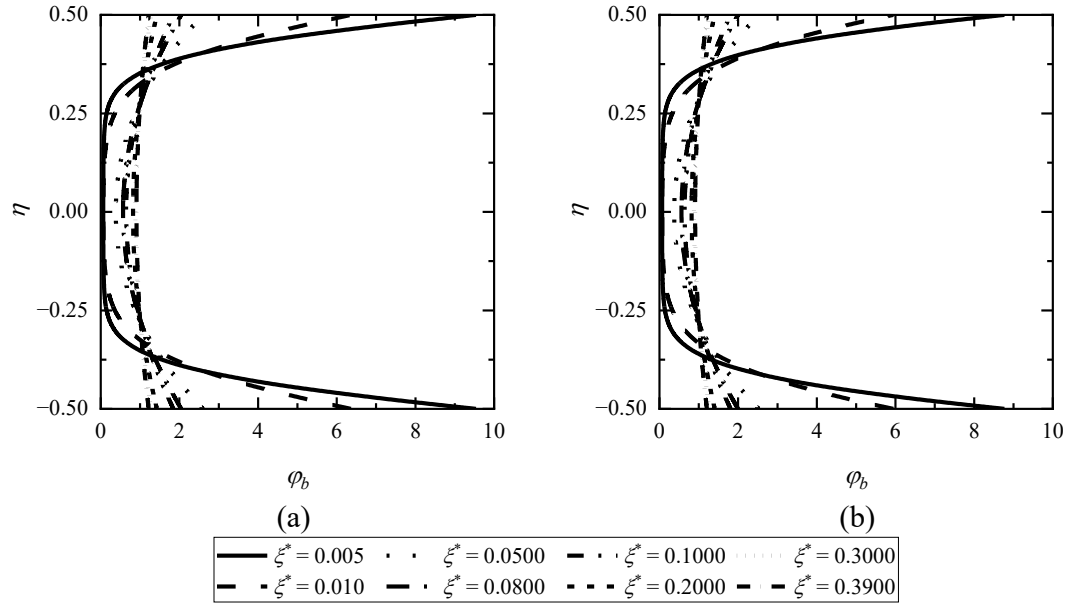

Fig. 2.12: φ_b profiles for different ξ^* values at $Bi = 10$, $\kappa = 0.1$, $F = 1$, $Da = 0.001$, for (a) $M = 0.5$, and (b) $M = 10$

Fully developed condition for thermal field

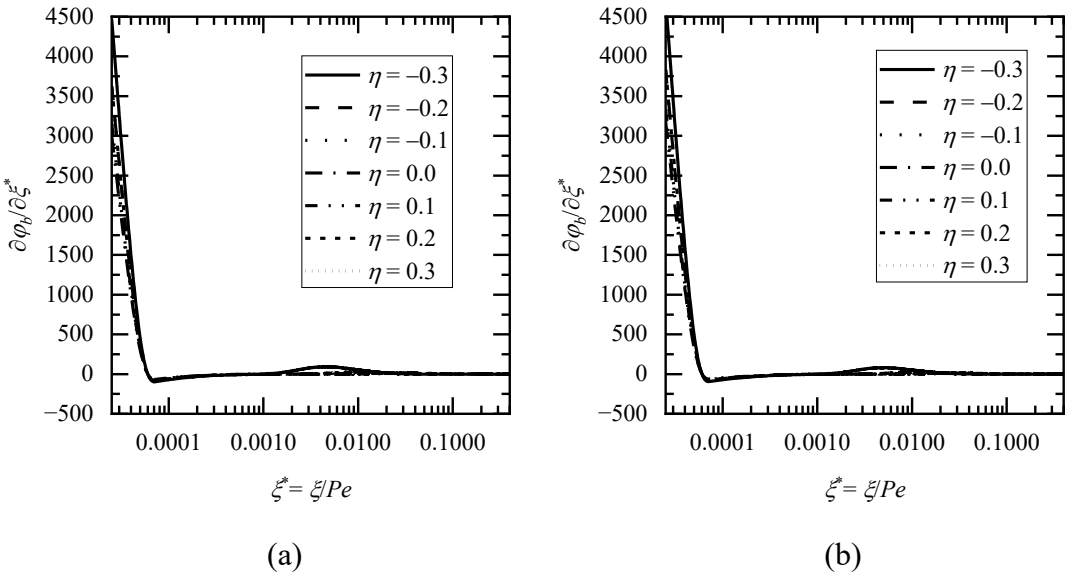

Fig. 2.13: $\partial\varphi_b / \partial\xi^*$ profiles for different η values for $Da = 0.001$, $F = 1$, $Bi = 10$, and $\kappa = 0.1$ for (a) $M = 0.5$ and, (b) $M = 10$

To validate the fully developed condition, a plot of $\partial\varphi_b / \partial\xi^*$ with ξ^* for $M = 0.5$ and $M = 50$ at η = –0.3, –0.2, –0.1, 0.0, 0.1, 0.2, and 0.3 is shown in Fig. 2.13 for $Da = 0.001$, $F = 1$, $Bi = 10$, and $\kappa = 0.1$. It can be seen that $\partial\varphi_b / \partial\xi^* \to 0$ for $\xi^* \geq 0.3$ in Fig. 2.13. For $-1/2 \leq \eta \leq 1/2$, when $\partial\varphi_b / \partial\xi^* \to 0$, the thermal field is characterized

as being fully developed. Even Fig. 2.12 is compatible with this observation. Thus, for LTNE, the fully matured condition is validated. Furthermore, as Satyamurty and Bhargavi [74] demonstrated, this phenomenon is true for LTE.

Wall temperature:

Since the constant heat flux conditions at the walls are applied, wall temperatures are unknown. Hence, wall temperature profiles are given to measure the effect of relevant parameters. The variations of wall temperatures in fluid phase (φ_{wf}) and porous phase (φ_{wp}) with ξ^* for $F = 10$, $Bi = 10$, and $\kappa = 1.0$ for $M = 0.5$, and 10 are demonstrated in Fig. 2.14(a, b) for (a) $Bi = 10$ and (b) $Bi = 100$.

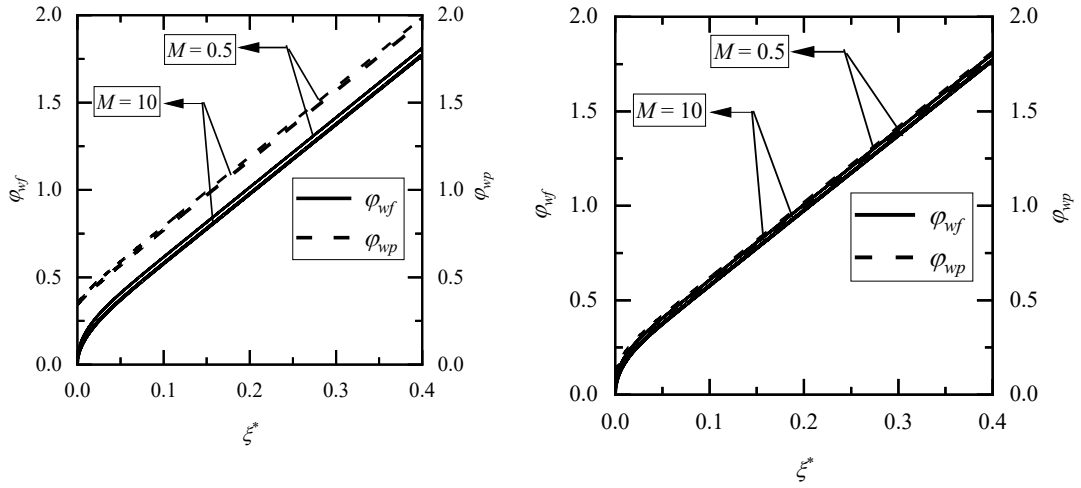

Fig. 2.14: Impact of φ_{wf} and φ_{wp} with ξ^* for $M = 0.5$, and 10 at $F = 10$, $Da = 0.005$, and $\kappa = 1.0$, for (a) $Bi = 10$ and (b) $Bi = 100$

As ξ^* increases, wall temperatures in the fluid phase (φ_{wf}) and porous phase (φ_{wp}) also increase for all Hartmann numbers. φ_{wf} and, φ_{wp} increase as ξ^* increases, initially non-linearly and then linearly for $\xi^* > 0.03$, say. It is the condition for the onset of a fully developed temperature field, where constant heat flux is employed at the channel walls. From Fig. 2.14, it can be observed that $\varphi_{wp} > \varphi_{wf}$ because of the heat transmission from the fluid to the porous, there is more heat for the porous wall temperature than the fluid wall temperature.

Local Nusselt numbers

The effect of the local Nusselt number, Nu_ξ with ξ^* for $F = 10$, $M = 1$, and $\kappa = 0.1$, is shown in Figs. 2.15(a) and 2.15(b) for $Bi = 10$ and 100, respectively, for $Da = 0.001$, 0.005, 0.01, 0.05, and 0.1. Similar plots are designed for various values of Hartmann number, M, ($M = 1$, 10, 25, 50, and 65) and thermal conductivity ratio, κ ($\kappa = 0.1$, 1.0, 5.0, and 10.0) in Fig. 2.16 and Figs. 2.17 and 2.18, respectively.

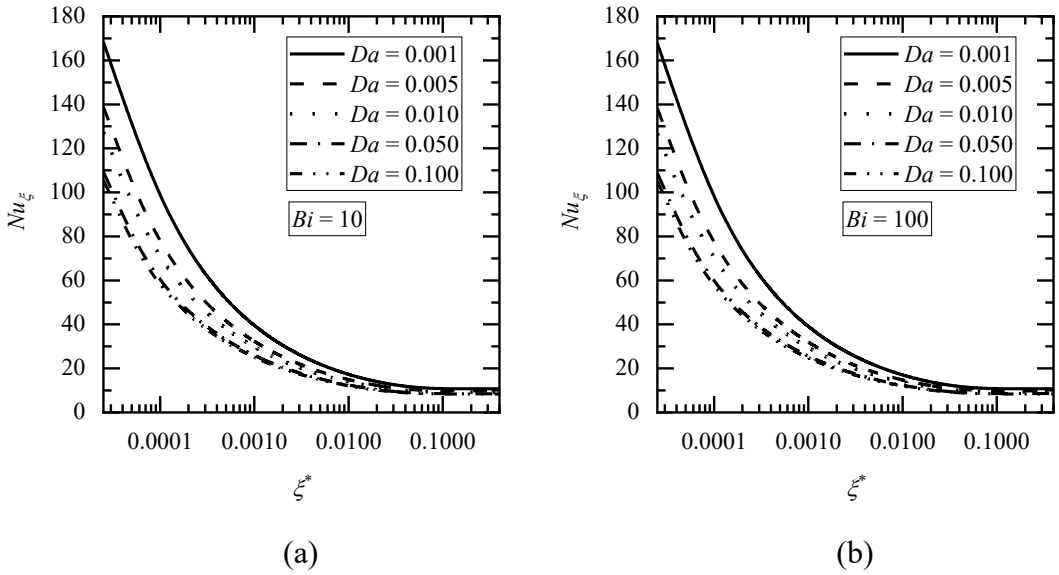

Fig. 2.15: Variation of Nu_ξ with ξ^* for various Darcy numbers, Da at $\kappa = 0.1$, $M = 1$, and $F = 10$ for (a) $Bi = 10$ and (b) $Bi = 100$

From Figs. 2.15 to 2.18, as ξ^* increases, Nu_ξ decreases. The variation trends of Nu_ξ with ξ^* for the channel under a porous medium are similar to the well-reported trend for the channel with clear fluid flow under LTE. As Darcy number is large (say at $Da = 0.1$), values of Nu_ξ, the channel with porous material are the same as those of Nu_ξ for the clear fluid channel. From Fig. 2.15, it decreases with increasing ξ^* and reaches the fully developed value for a given Da. As the Darcy number increases, it decreases and reaches the local Nusselt number in the fluid region. Nu_ξ decreases as Biot number increases. The effect of Hartmann number on Nu_ξ is discussed in Fig. 2.16. As the Hartmann number increases, it also increases for every Biot number, Bi.

The impact of the ratio between effective thermal conductivities of the porous and fluid (i.e., thermal conductivity ratio, κ = 0.1, 1.0, and 10.0) on the variations of Nu_ξ is analyzed and illustrated in Figs. 2.17(a) and 2.17(b) for Hartmann number, M = 1 and 50, respectively at Da = 0.005, F = 10, and Bi = 10. Similar types of plots are given in Fig. 2.18 for a large Biot number, Bi = 100. The key findings observed from Figs. 2.17 and 2.18 are: (i) there is a significant change with respect to κ $\left(= k_{pe} / k_{fe}\right)$. As κ increases, Nu_ξ decreases for all Da, F, M, and Bi, (ii) as Hartmann number increases, Nu_ξ increases for each value of the ratio, κ (iii) by comparing Figs. 2.17 and 2.18, as Bi increases, Nu_ξ decreases for each value of ratio, κ. This feature was also observed for the constant wall temperature boundary condition given by Nield et al. [34]. A porous material with a higher effective thermal conductivity of the porous phase than a fluid phase is obtained by increasing the ratio κ. Since the Nusselt number correlates to the fluid phase's convective heat transmission, the values of the Nusselt number for the porous material-filled channel fall.

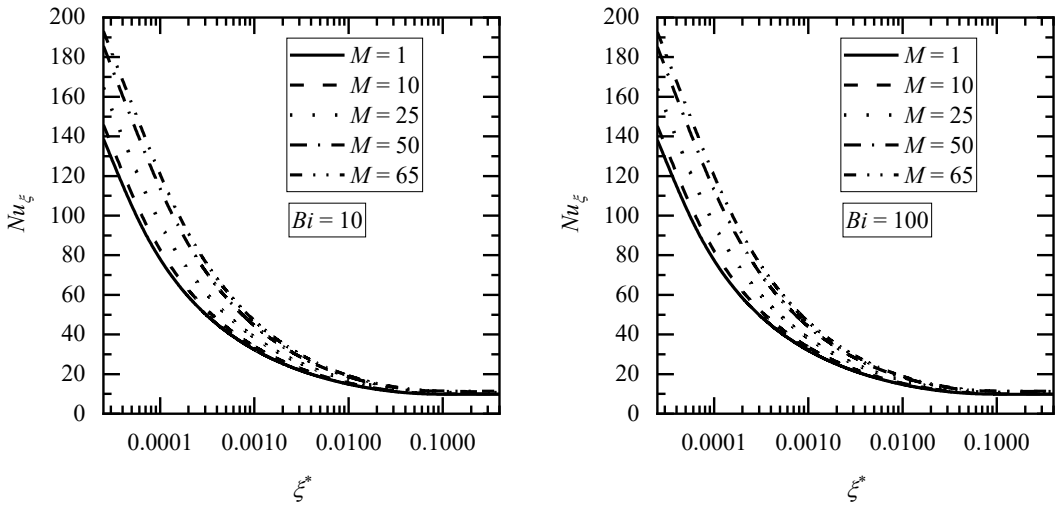

Fig. 2.16: Variation of Nu_ξ with ξ^* for various Hartmann numbers, M at κ = 0.1, Da = 0.005 and F = 10 for (a) Bi = 10 and (b) Bi = 100

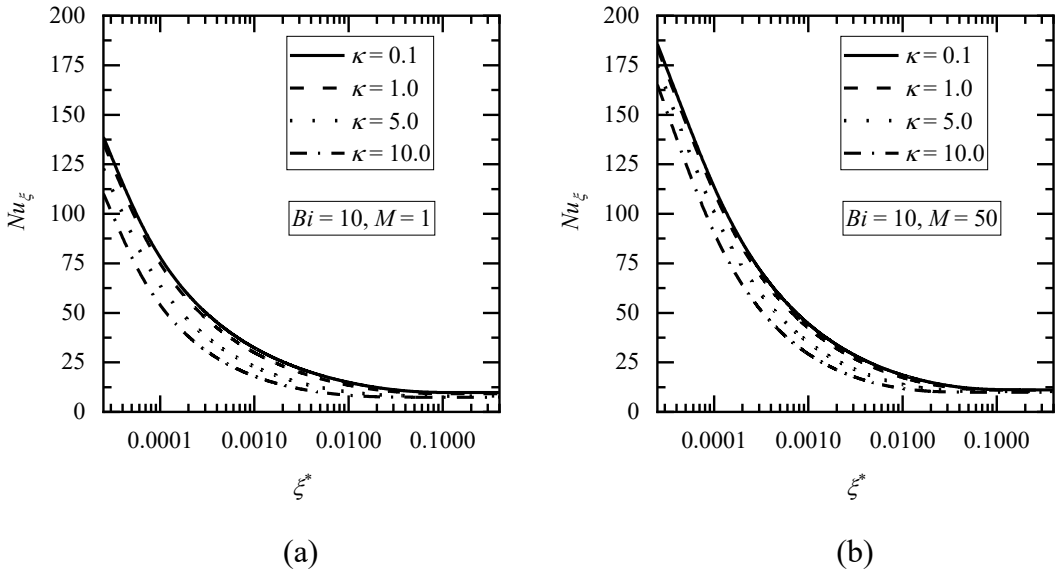

Fig. 2.17: Variation of Nu_ξ with ξ^* for various thermal conductivity ratios, κ at Da = 0.005, Bi = 10, and F = 10 for (a) M = 1 and (b) M = 50

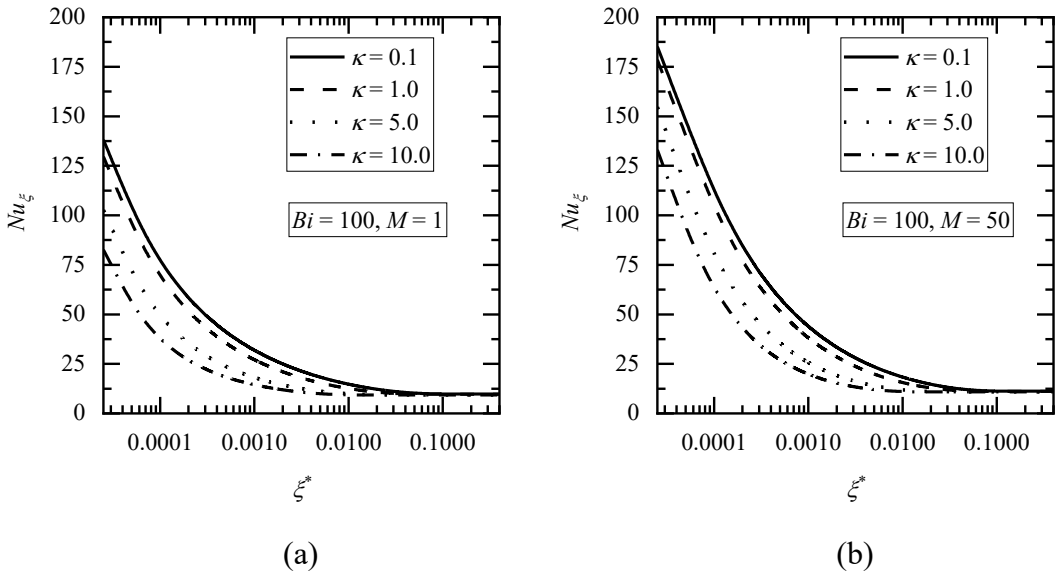

Fig. 2.18: Variation of Nu_ξ with ξ^* for various thermal conductivity ratios, κ at Da = 0.005, Bi = 100, and F = 10 for (a) M = 1 and (b) M = 50

The variation of Forchheimer number, F, is given in Table 2.6 at various ξ^* values at Darcy number Da = 0.001, Bi = 50, κ = 0.1, and for two different values of M, M = 5 and M = 65. From Table 2.6, it is clear that the effect of F is much less on Nu_ξ.

Table 2.6: Variation of Nu_ξ for different Forchheimer numbers, F

	M = 5, Bi = 50			M = 65, Bi = 50		
ξ^*	**F = 1**	**F = 10**	**F = 100**	**F = 1**	**F = 10**	**F = 100**
0.00005	130.977	130.977	130.979	158.864	158.864	158.864
0.00010	98.670	98.670	98.672	122.599	122.599	122.599
0.00100	39.285	39.285	39.286	47.222	47.222	47.222
0.00500	21.744	21.744	21.744	24.806	24.806	24.806
0.05000	11.447	11.448	11.448	12.244	12.244	12.244

At the fully developed length, say $\xi^* \geq 0.38$, local Nusselt numbers (Nu_ξ) approach fully developed Nusselt numbers (Nu_{fd}), which are obtained analytically. Local Nusselt numbers, (Nu_ξ) at $\xi^* = 0.38$ and the fully developed Nusselt numbers values (Eq. (2.44)) are given in Table 2.7 for different Hartmann numbers, M = 1, 5, and 10 for Da = 0.005, F = 0, Bi = 10, and κ = 0.1. At the fully developed length, say $\xi^* > 0.38$, local Nusselt numbers (Nu_ξ) approach fully developed Nusselt numbers, Nu_{fd}, which are obtained analytically, as seen in Table 2.7.

Table 2.7: Local Nusselt numbers (Nu_ξ) and the fully developed Nusselt numbers (Nu_{fd}) values with various Hartmann numbers, M at $\xi^* = 0.38$

M	Nu_ξ	Nu_{fd}
1	9.753	9.894
5	9.832	9.971
10	10.143	9.165

Comparison with the work done by Bhargavi and Reddy [75] using LTE for F = 0.0 and M = 0.0

A comparison has been made for large Bi and κ = 1.0, the same as the LTE condition given in Bhargavi and Reddy [75]. Hence, the present work has been compared with that of Bhargavi and Reddy [75] for Darcy numbers Da = 0.005 and 0.1 at F = 0 and M = 0. Variation of Nu_ξ with ξ^* is given in Fig. 2.19. From Fig. 2.19, the present results for large Bi and κ = 1.0 match Bhargavi and Reddy's [75] results.

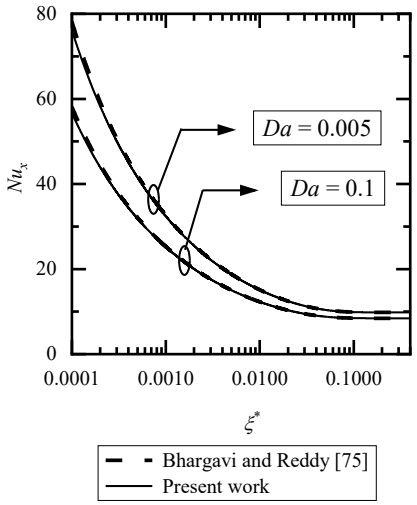

Fig. 2.19: Comparison of Nu_ξ with the literature Bhargavi and Reddy [75] for $F = 0$

Similarly, for the LTE model (immense value of *Bi*), and in the absence of Hartmann number and Forchheimer number, the values of Nu_ξ have been compared with those obtained from the experimental study by Jiang et al. [219] with appropriate scaling. Nu_ξ values have been calculated in an empty plate channel (i.e., in case of large *Da* values) given in Fig. 2.20. The experiment results are taken for water at two different Reynolds numbers $Re = 300$ and $Re = 550$. The agreement is good.

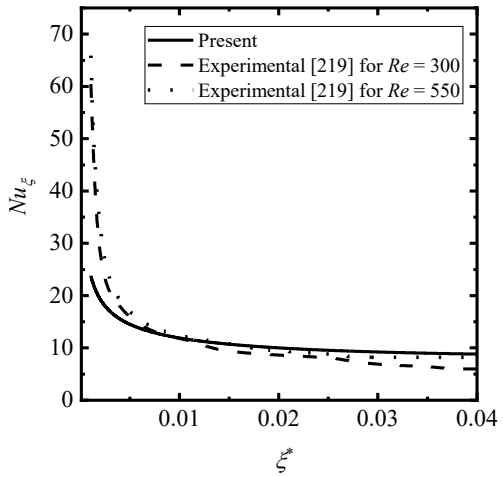

Fig. 2.20: Comparison of Nu_ξ for different ξ^* in an empty plate channel

2.8 Conclusion

The current work involves the numerical study of forced convection heat transfer at the thermal entry of parallel plate channels filled with porous medium under LTNE using a successive acceleration replacement (SAR) scheme. The parallel plates were exposed to a constant wall heat flux. The flow field is unidirectional and obeys Darcy Brinkman Forchheimer equation. The problem is defined by Darcy number (*Da*), Forchheimer number (*F*), Hartmann number (*M*), Biot number (*Bi*), and thermal conductivity ratio (κ).

The numerical solution has been obtained for velocity, skin friction coefficient, temperatures in both phases porous and fluid, and dimensionless temperature based on bulk mean temperature, wall temperature, and local Nusselt number at the entrance for LTNE condition. The key findings on the behaviour of the investigated system are:

i. Velocity decreases slightly as the Forchheimer number increases. However, velocity falls with an increase in Hartmann's number. Additionally, velocity increases as the Darcy number rises, and at a significant value of *Da*, the velocity attains the velocity in the fluid region. As the Forchheimer number increases, ReC_{fp} increases at a given *Da*. *Da* (> 1.0) is prominent ReC_{fp} tends to 6.0 (value in the clear fluid region). Similarly, at a given *Da*, ReC_{fp} increases as the Hartmann number increases, and for prominent *Da* (> 1.0), ReC_{fp} tends to 6.0.

ii. For the Darcy Brinkman Model, analytical equations for dimensionless temperature and the fully developed Nusselt number are found for the fully developed thermal field, both in the presence of the Hartmann number and without the Forchheimer term (*F* = 0).

iii. For all Darcy numbers (*Da*) and Forchheimer numbers (*F*), as Biot number (*Bi*) increases, the temperatures of the porous and fluid phases decrease, and hence, LTE is approached. That means LTNE tends to LTE. When κ = 1.0, φ_f profile is the same for the local thermal equilibrium (LTE) φ_f profile when *Bi* is huge. In the presence of Forchheimer numbers, the Hartmann number increases, φ_f and φ_p decrease. Also, values of φ_p are larger than φ_f.

iv. For large $Da > 0.1$, high κ (say $\kappa = 10.0$), and small Bi, there is a large temperature difference between the two phases. So, the LTNE model can be used.

v. Wall temperature (φ_{wf} and, φ_{wp}) increases as ξ^* increases for all Biot numbers, from being initially nonlinear to subsequently becoming linear for $\xi^* > 0.005$, which is the onset of a fully developed condition. A fully developed condition is shown even when LTNE is used. It serves the purpose of the downstream boundary condition when axial conduction is used (elliptic PDE). Moreover, $\varphi_{wp} > \varphi_{wf}$ because heat transmission from fluid to porous is greater at porous wall temperature than at fluid wall temperature.

vi. As the thermal conductivity ratio and Biot number grow, the local Nusselt number decreases. However, it increases with an increase in Hartmann's number. There is a low effect on Nu_{ξ} due to Forchheimer number (F).

vii. Hence, as a result of the current research work, it is possible to deduce that small κ can improve heat transmission in the entry of porous-filled channels. It is better to use LTNE conditions at the channel entrance.

Chapter 3

Forced Convection Heat Transfer at the Entry Region of the Porous Filled Channel with Axial Conduction Effect

3.1 Introduction

This study explores the impact of axial conduction on forced convective heat transfer characteristics within a channel filled with porous material undergoing thermal development under LTNE. The channel's walls experience a constant heat flux, and the flow within the porous region follows the Darcy Brinkman model. The investigation quantifies the influence of the Biot and Peclet numbers on heat transfer enhancement. A transverse magnetic field is applied along the channel walls, and the system is characterized by well-known parameters such as Darcy number (*Da*), Hartmann number (*M*), Biot number (*Bi*), Peclet number (*Pe*), and thermal conductivity ratio. Numerical solutions are obtained using a successive accelerated replacement (SAR) scheme and presented dimensionless temperature profiles in the fluid and porous phases and plots of the local Nusselt number. At low *Pe*, the axial conduction effect is more pronounced for all *Bi*, whereas at large *Pe*, the axial conduction effect becomes negligible. The local Nusselt number decreases with an increase in the ratio of thermal conductivity and the Biot number. For a large Biot number, LTNE is equivalent to LTE.

3.2 Mathematical Model

The schematic model and coordinate system is discussed in Chapter 2§, 3.2. The Darcy Brinkman model for the fluid flow through the porous region. The field includes axial conduction. Heat generation and thermal dispersion are negligible. The thermophysical properties are constant.

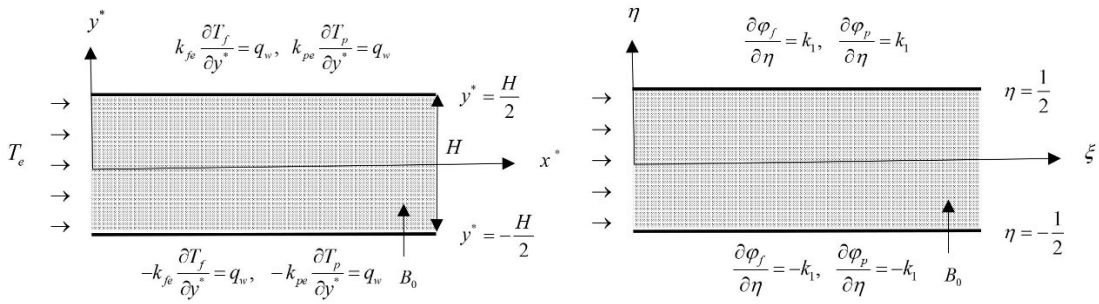

(a) Dimensional (b) Dimensionless

Fig. 3.1: Schematic model and the parallel plate channel coordinate system

Governing Equations

The momentum equation for the fluid flow across a porous medium by employing the Darcy Brinkman model is given by:

$$\mu_e \frac{d^2u}{dy^{*2}} - \frac{\mu}{K}u + \vec{J}\times\vec{B} = \frac{dp}{dx^*} \tag{3.1}$$

In Eq. (3.1), u denotes the velocity in the porous medium, and μ_e, μ, and K are effective viscosity, fluid viscosity, and permeability in the porous region, respectively. $\vec{J}$ is the electric current density and, $\vec{B}$ is the magnetic induction vector of the applied uniform magnetic field. The formulation of the Lorentz force is discussed in Chapter 2§, Eq. (2.1). Thus, the governing equations given in Eq. (3.1) are reduced to:

$$\mu_e \frac{d^2u}{dy^{*2}} - \frac{\mu}{K}u - \sigma {B_0}^2 u = \frac{dp}{dx^*} \tag{3.2}$$

The steady-state conservation of thermal energy equations of the fluid and porous phases are given by:

Fluid phase

$$\left(\rho C_p\right)\left(u\frac{\partial T_f}{\partial x^*}\right) = k_{fe}\left(\frac{\partial^2 T_f}{\partial x^{*2}} + \frac{\partial^2 T_f}{\partial y^{*2}}\right) + a_{pf}h_{pf}\left(T_p - T_f\right) \tag{3.3}$$

Porous phase

$$k_{pe}\left(\frac{\partial^2 T_p}{\partial x^{*2}}+\frac{\partial^2 T_p}{\partial y^{*2}}\right)-a_{pf}h_{pf}\left(T_p-T_f\right)=0 \tag{3.4}$$

In Eqs. (3.3) and (3.4), ρ is density, C_p is the specific heat, T_f is the fluid phase temperature, T_p is the porous phase temperature, k_{fe} is the effective fluid thermal conductivity, k_{pe} is the effective porous thermal conductivity, respectively. a_{pe} is the interfacial area per unit volume of the porous media, and h_{pf} is the porous-to-fluid heat transfer coefficient in the literature.

Boundary Conditions

Hydrodynamics boundary conditions are as follows:

$$u=0, \quad \text{at } y^*=\frac{H}{2},-\frac{H}{2} \quad \left(\text{No-slip condition}\right) \tag{3.5}$$

Thermal boundary conditions are given by:

$$\left.\begin{aligned} k_{fe}\frac{dT_f}{dy^*}=q_w,\ \ k_{pe}\frac{dT_p}{dy^*}=q_w \ \text{ at } y^*=\frac{H}{2} \\ -k_{fe}\frac{dT_f}{dy^*}=q_w,\ \ -k_{pe}\frac{dT_p}{dy^*}=q_w \ \text{ at } y^*=-\frac{H}{2} \end{aligned}\right\} \quad \left(\text{Heat flux condition}\right) \tag{3.6}$$

$$T_{f,p}\left(0,y^*\right)=T_e, \quad -\frac{H}{2}<y^*<\frac{H}{2} \quad \left(\text{Inlet condition}\right) \tag{3.7}$$

$$\frac{\partial}{\partial x^*}\left(\frac{T_{f,p}-T_w}{T_b-T_w}\right)=0 \quad \text{at } -\frac{H}{2}<y^*<\frac{H}{2} \quad \text{(Exit condition)} \tag{3.8}$$

$$T_p=T_f=T_{interface} \quad \left(\text{Porous-fluid interface}\right) \tag{3.9}$$

In Eq. (3.9), the temperature at the porous-fluid interface is denoted by $T_{interface}$.

Dimensionless Variables

The following dimensionless variables are utilised to construct the governing equations, boundary conditions, and porous-fluid interface condition {Eqs. (3.2) to (3.9)} dimensionless.

$$\left.\begin{aligned} &\xi = \frac{x^*}{H},\ \eta = \frac{y^*}{H},\ U = \frac{u\mu}{\left(-\frac{dp}{dx^*}\right)H^2},\ U_{avg} = \frac{u_{avg}\mu}{\left(-\frac{dp}{dx^*}\right)H^2} \\ &\varphi_f = \frac{\left(T_f - T_e\right)}{\left(\frac{q_w H}{k_f}\right)},\ \varphi_p = \frac{\left(T_p - T_e\right)}{\left(\frac{q_w H}{k_f}\right)} \end{aligned}\right\} \tag{3.10}$$

In Eq. (3.10), ξ and η are the dimensionless coordinates along the x^* and y^* directions. The dimensionless temperature and velocity are denoted by φ and U, respectively. The fluid and porous phases are designated by subscripts f and p, respectively. The average velocity across the channel is denoted by u_{avg}. The normalized ξ^* can be defined as,

$$\xi^* = \frac{\xi}{Pe} \tag{3.11}$$

The governing equations (Eqs. (3.2) to (3.4)) in dimensional form become dimensionless form after applying the dimensionless variables are given in Eq. (3.10).

$$\frac{1}{\varepsilon}\frac{d^2U}{d\eta^2} - \left(\frac{1}{Da} + M^2\right)U + 1 = 0 \tag{3.12}$$

$$U^N(\eta)\frac{\partial\varphi_f}{\partial\xi^*} = \frac{1}{k_1}\left[A_c\frac{1}{Pe^2}\frac{\partial^2\varphi_f}{\partial\xi^{*2}} + \frac{\partial^2\varphi_f}{\partial\eta^2} + Bi\ \kappa\left(\varphi_p - \varphi_f\right)\right] \tag{3.13}$$

$$A_c\frac{1}{Pe^2}\frac{\partial^2\varphi_p}{\partial\xi^{*2}} + \frac{\partial^2\varphi_p}{\partial\eta^2} - Bi\left(\varphi_p - \varphi_f\right) = 0 \tag{3.14}$$

In Eqs. (3.13) and (3.14), the presence or absence of the axial conduction term depends on the value of A_c. Specifically, when A_c = 0, the axial conduction term is omitted, whereas when A_c = 1, the axial conduction term is included. Furthermore, where A_c = 0, the solutions to Eqs. (3.13) and (3.14) with respect to the thermal field are independent of *Pe* in terms of their dependence on ξ^*.

Eq. (3.13) and (3.14) are the dimensionless form of thermal energy equations in fluid and porous phase, respectively (LTNE model) and *Da*, *M*, *Pe*, *Bi*, and κ denote Darcy number, Hartmann number, Peclet number, Biot number, and thermal conductivity ratio, respectively; ε and k_1 represent the ratio between the viscosity of the fluid to the effective viscosity of the porous, and fluid thermal conductivity to effective fluid thermal conductivity, respectively and it is defined as:

$$Da = \frac{K}{H^2} \tag{3.15}$$

$$M = \sqrt{\frac{\sigma B_0^2 H^2}{\mu_f}} \tag{3.16}$$

$$Pe = \frac{u_{avg} H}{\alpha} \tag{3.17}$$

$$Bi = \frac{a_{pf} h_{pf} H^2}{k_{pe}} \tag{3.18}$$

$$\kappa = \frac{k_{pe}}{k_{fe}} \tag{3.19}$$

$$\varepsilon = \frac{\mu}{\mu_e} \tag{3.20}$$

$$k_1 = \frac{k_f}{k_{fe}} \tag{3.21}$$

In Eq. (3.17), α is the thermal diffusivity and k_f in Eq. (3.21), is the thermal conductivity in the fluid region.

In Eq. (3.13), $U^N(\eta)$ is normalized velocity and can be calculated by,

$$U^N(\eta) = \frac{U(\eta)}{U_{avg}} \tag{3.22}$$

In Eq. (3.22), U_{avg}, the average velocity is calculated by the following formula:

$$U_{avg} = \int_{-1/2}^{1/2} U(\eta)\, d\eta \tag{3.23}$$

Dimensionless Boundary Conditions

Hydrodynamics boundary conditions are as follows:

$$U = 0, \quad \text{at} \quad \eta = \frac{1}{2}, -\frac{1}{2} \tag{3.24}$$

Thermal boundary conditions are given by:

$$\left.\begin{aligned} \frac{\partial \varphi_f}{\partial \eta} &= k_1, \quad \frac{\partial \varphi_p}{\partial \eta} = k_2 \qquad \text{at} \quad \eta = \frac{1}{2} \\ \frac{\partial \varphi_f}{\partial \eta} &= -k_1, \quad \frac{\partial \varphi_p}{\partial \eta} = -k_2 \quad \text{at} \quad \eta = -\frac{1}{2} \end{aligned}\right\} \tag{3.25}$$

$$\varphi_{f,p}(0,\eta) = 0, \quad \text{for} \quad -\frac{1}{2} < \eta < \frac{1}{2} \tag{3.26}$$

$$\frac{\partial \varphi_b}{\partial \xi^*} = 0 \Rightarrow \left.\begin{aligned} \frac{\partial \varphi_f}{\partial \xi^*} &= \frac{\varphi_f}{\varphi^*}\frac{\partial \varphi^*}{\partial \xi^*} \\ \frac{\partial \varphi_p}{\partial \xi^*} &= \frac{\varphi_p}{\varphi^*}\frac{\partial \varphi^*}{\partial \xi^*} \end{aligned}\right\} \text{ at } \xi^* \geq \xi^*_{fd} \text{ for } -\frac{1}{2} < \eta < \frac{1}{2} \tag{3.27}$$

$$\varphi_f = \varphi_p = \varphi_{interface} \tag{3.28}$$

In Eq. (3.25), the ratio, k_2 is defined by

$$k_2 = \frac{k_f}{k_{pe}} \tag{3.29}$$

In Eq. (3.27), ξ^*_{fd} is the normalized fully developed length. Dimensionless bulk mean temperature, $\varphi^*(\xi^*)$ and the dimensionless temperature based on the bulk mean temperature, $\varphi_b(\xi^*)$ are defined by

$$\varphi^*(\xi^*) = \frac{(T_b - T_e)}{qH / k_f} \tag{3.30}$$

$$\varphi_b(\xi^*) = \frac{(T - T_e)}{(T_b - T_e)} = \frac{\varphi}{\varphi^*} \tag{3.31}$$

In Eqs. (3.30) and (3.31), T_b is the bulk mean temperature.

3.2.1 Velocity Expression

The expression of normalized velocity (Eq. (3.22)) is given by

$$U^N(\eta) = \frac{\sqrt{\varepsilon\left(\frac{1}{Da} + M^2\right)} - \sqrt{\varepsilon\left(\frac{1}{Da} + M^2\right)}\,\mathrm{Cos}\left[\eta\sqrt{\left(\frac{1}{Da} + M^2\right)}\right]\mathrm{Sec}h\left[\frac{1}{2}\sqrt{\left(\frac{1}{Da} + M^2\right)}\right]}{\sqrt{\left(\frac{1}{Da} + M^2\right)} - \mathrm{Tan}h\left[\frac{1}{2}\sqrt{\left(\frac{1}{Da} + M^2\right)}\right]} \tag{3.32}$$

3.3 Numerical Methodology

Numerical solutions for Eqs. (3.13) and (3.14), with the boundary conditions on φ, as specified in Eqs. (3.25) to (3.27) have been computed using the successive accelerated replacement (SAR) scheme using the velocity expression given in Eq. (3.32). This numerical method is described in Satyamurty and Bhargavi [74] and Bhargavi and

Reddy [75]. By employing the SAR scheme, the study obtained approximate solutions that satisfy the given equations and boundary conditions, facilitating the analysis and understanding of the system's behaviour. The iterative scheme, initially developed by Lieberstein [207], was designed to solve systems of nonlinear algebraic equations, particularly those characterized as mildly nonlinear elliptic partial differential equations. Over the years, this scheme has found extensive application in solving nonlinear ordinary differential equations that arise in compressible flows, as evidenced in the works of Lew [206] and Dellinger [208]. Dellinger [208] coined the term SAR to refer to this specific iterative approach.

3.3.1 Application of the SAR Method

Non-uniform:

Non-uniform grids described in Chapter 2, § 2.6.1 have been employed in the axial direction. Let *PD* and *QD* represent the number of divisions in ξ and η directions, respectively, while $\Delta\xi^*$ and $\Delta\eta$ represent the width in ξ and η directions, respectively. When the terms in energy Eqs. (3.13) and (3.14) are expressed in finite difference form, the errors $\bar{\varphi}_f$ in the fluid phase and $\bar{\varphi}_p$ in the porous phase are given by:

$$\begin{aligned}\bar{\varphi}_f(P,Q) = U^N\left[\frac{\varphi_f(P,Q)-\varphi_f(P-1,Q)}{\xi(P)-\xi(P-1)}\right] - \frac{Bi\ \kappa}{k_1}\left[\varphi_p(P,Q)-\varphi_f(P,Q)\right] \\ -\frac{1}{k_1}\left[\frac{\varphi_f(P,Q+1)-2\varphi_f(P,Q)+\varphi_f(P,Q-1)}{(\Delta\eta)^2}\right] \\ -\frac{1}{k_1 Pe^2}\left\{\frac{\begin{array}{c}\left[\xi(P-1)-\xi(P)\right]\varphi_f(P+1,Q) \\ +\left[\xi(P)-\xi(P+1)\right]\varphi_f(P-1,Q) \\ -\left[\xi(P-1)-\xi(P+1)\right]\varphi_f(P,Q)\end{array}}{\left[\xi(P-1)-\xi(P+1)\right]\left[\xi(P)-\xi(P+1)\right]\left[\xi(P-1)-\xi(P)\right]}\right\}\end{aligned} \tag{3.33}$$

$$\bar{\varphi}_p(P,Q)=\left[\frac{\varphi_p(P,Q+1)-2\varphi_p(P,Q)+\varphi_p(P,Q-1)}{(\Delta\eta)^2}\right]-Bi\left[\varphi_p(P,Q)-\varphi_f(P,Q)\right]$$
$$+\frac{1}{Pe^2}\left\{\frac{\begin{array}{c}\left[\xi(P-1)-\xi(P)\right]\varphi_p(P+1,Q)\\+\left[\xi(P)-\xi(P+1)\right]\varphi_p(P-1,Q)\\-\left[\xi(P-1)-\xi(P+1)\right]\varphi_p(P,Q)\end{array}}{\left[\xi(P-1)-\xi(P+1)\right]\left[\xi(P)-\xi(P+1)\right]\left[\xi(P-1)-\xi(P)\right]}\right\} \tag{3.34}$$

The following derivatives are required to correct the profile for φ_f and φ_p:

$$\frac{\partial\bar{\varphi}_f(P,Q)}{\partial\varphi_f(P,Q)}=\frac{U^N}{\left[\xi(P)-\xi(P-1)\right]}+\frac{1}{k_1}\left\{\frac{1}{Pe^2\left[\xi(P)-\xi(P+1)\right]\left[\xi(P-1)-\xi(P)\right]}\right\}$$
$$+\frac{1}{k_1}\left\{\frac{2}{(\Delta\eta)^2}+Bi\ \kappa\right\} \tag{3.35}$$

$$\frac{\partial\bar{\varphi}_p(P,Q)}{\partial\varphi_p(P,Q)}=-\left\{\frac{1}{Pe^2\left[\xi(P)-\xi(P+1)\right]\left[\xi(P-1)-\xi(P)\right]}+\frac{2}{(\Delta\eta)^2}+Bi\right\} \tag{3.36}$$

Discretized boundary conditions are as follows:

Wall boundary conditions

$$\left.\begin{array}{l}\varphi_f(P,QD+1)=\dfrac{2k_1\ \Delta\eta+4\varphi_f(P,QD)-\varphi_f(P,QD-1)}{3}\\ \varphi_p(P,QD+1)=\dfrac{2k_2\ \Delta\eta+4\varphi_p(P,QD)-\varphi_p(P,QD-1)}{3}\end{array}\right\}\quad\text{(Upper wall)} \tag{3.37}$$

$$\left.\begin{array}{l}\varphi_f(P,1)=\dfrac{2k_1\ \Delta\eta+4\varphi_f(P,2)-\varphi_f(P,3)}{3}\\ \varphi_p(P,1)=\dfrac{2k_2\ \Delta\eta+4\varphi_p(P,2)-\varphi_p(P,3)}{3}\end{array}\right\}\quad\text{(Lower wall)} \tag{3.38}$$

Inlet boundary condition

$$\varphi_{f,p}\left(1,Q\right)=0 \;\text{ for }\; 1+\left(\frac{QD}{2}\right)<Q<\left(1+QD\right) \tag{3.39}$$

Exit boundary condition

$$\left.\begin{aligned}
\varphi_f\left(PD+1,Q\right)&=\frac{\varphi^*\left(PD+1\right)\left\{\left[1+\left(\frac{\Delta\xi^*_{PD-2}}{\Delta\xi^*_{PD-1}}\right)\right]^2\varphi_f\left(PD,Q\right)-\varphi_f\left(PD-1,Q\right)\right\}}{\left\{\left[1+\left(\frac{\Delta\xi^*_{PD-2}}{\Delta\xi^*_{PD-1}}\right)\right]^2\varphi^*\left(PD\right)-\varphi^*\left(PD-1\right)\right\}}\\
\varphi_p\left(PD+1,Q\right)&=\frac{\varphi^*\left(PD+1\right)\left\{\left[1+\left(\frac{\Delta\xi^*_{PD-2}}{\Delta\xi^*_{PD-1}}\right)\right]^2\varphi_p\left(PD,Q\right)-\varphi_p\left(PD-1,Q\right)\right\}}{\left\{\left[1+\left(\frac{\Delta\xi^*_{PD-2}}{\Delta\xi^*_{PD-1}}\right)\right]^2\varphi^*\left(PD\right)-\varphi^*\left(PD-1\right)\right\}}\\
&\text{at } \xi^*\geq\xi^*_{fd} \quad \text{for } 1\leq Q\leq 1+QD
\end{aligned}\right\} \tag{3.40}$$

Further, in Eq. (3.40)

$$\Delta\xi^*_P=\xi^*\left(P+1\right)-\xi^*\left(P\right) \tag{3.41}$$

3.4 Local Nusselt Number

The local heat transfer coefficient (h_ξ) is determined at the wall $y^*=H/2$ adjacent to the porous medium.

$$-k_{fe}\left.\frac{\partial T_f}{\partial y^*}\right|_{y^*=\frac{H}{2}}=h_\xi\left(T_w-T_b\right) \tag{3.42}$$

In Eq. (3.42), the bulk mean temperature (T_b) is denoted as follows:

$$T_b = \frac{\int_{-H/2}^{H/2} uT_f dy^*}{\int_{-H/2}^{H/2} udy^*} \tag{3.43}$$

In terms of dimensionless variables {using Eq. (3.10)}, the local Nusselt number at $\eta = 1/2$, Nu_ξ is given by:

$$Nu_\xi = \frac{h_\xi (2H) k_1}{k_f} = \frac{-2\left(\frac{\partial \varphi_f}{\partial \eta}\right)\Big|_{\eta=\frac{1}{2}}}{\left(\varphi_w - \varphi^*\right)} = \frac{2}{\left(\varphi^* - \varphi_w\right)} \tag{3.44}$$

In Eq. (3.44), φ_w and φ^* are defined in Chapter 2, § Eqs. (2.33) and (2.34) and φ^* is evaluated by Eq. (2.35) in Chapter 2.

3.5 Numerical Results and Discussions

Numerical solutions have been obtained using the thermal energy two-equation model (Eqs. (3.13) and (3.14)) in a channel filled with a porous medium. The fully developed velocity profile (Eq. (3.32)) has been employed in the numerical analysis to simulate and investigate the system's heat transfer and thermal behaviour. It is assumed that $k_1 = k_f / k_{fe} = 1$, $k_2 = k_f / k_{se} = 1$, and $\varepsilon = \mu / \mu_{eff} = 1$. $0.001 \le Da \le 0.1$, $0.5 \le M \le 65$, $5 \le Pe \le 100$, $10 \le Bi \le 100$, and $0.1 \le \kappa \le 10$ are the ranges used for parameters.

3.5.1 Thermal Field

This section examines dimensionless temperature profiles, dimensionless temperature based on the bulk mean temperature in both fluid and porous phases, and local Nusselt number for flow through the porous-filled channel.

The dimensionless temperature in the fluid phase and porous phase:

To investigate the effects of axial conduction, Hartmann number (*M*), Biot number (*Bi*), and thermal conductivity ratio (κ) in a thermally developing region, plots are presented for different values of *Pe*, *M*, *Bi*, and κ at various values of normalized dimensionless axial distances, ξ^*. These plots allow for a comprehensive analysis of how the above parameters impact thermal development and heat transfer characteristics within the system at different positions along the channel.

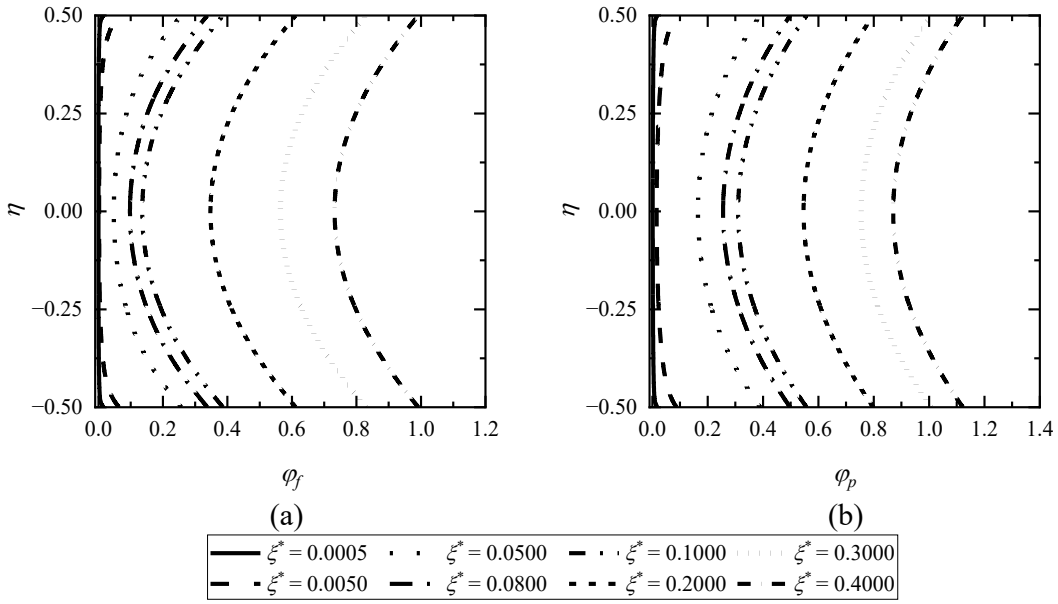

Fig. 3.2: Impact of (a) φ_f and (b) φ_p for distinct ξ^* values for *Bi* = 10, *Pe* = 5, *M* = 1, and κ = 0.1 at *Da* = 0.001

Dimensionless temperature profiles, φ_f in the fluid phase and φ_p the porous phase are given in Fig. 3.2 at *Da* = 0.001, *Bi* = 10, *Pe* = 5, *M* = 1, and κ = 0.1. A similar type of plot is given for large values of *Pe* (*Pe* = 100), *M* (*M* = 65), *Bi* (*Bi* = 100), and κ (κ = 10) in Figs. 3.3 to 3.6, respectively. The temperature behaviour of the fluid and porous phases will depend on the system's specific heat transfer mechanisms and boundary conditions. From Figs. 3.2 to 3.6, both the fluid and porous phases temperatures (φ_f, and φ_p) might experience temperature increases with normalized axial distance, ξ^* for all the values of parameters *Pe*, *M, Bi*, and κ. It could occur when there is significant heat exchange between the phases, which absorb heat from the surroundings.

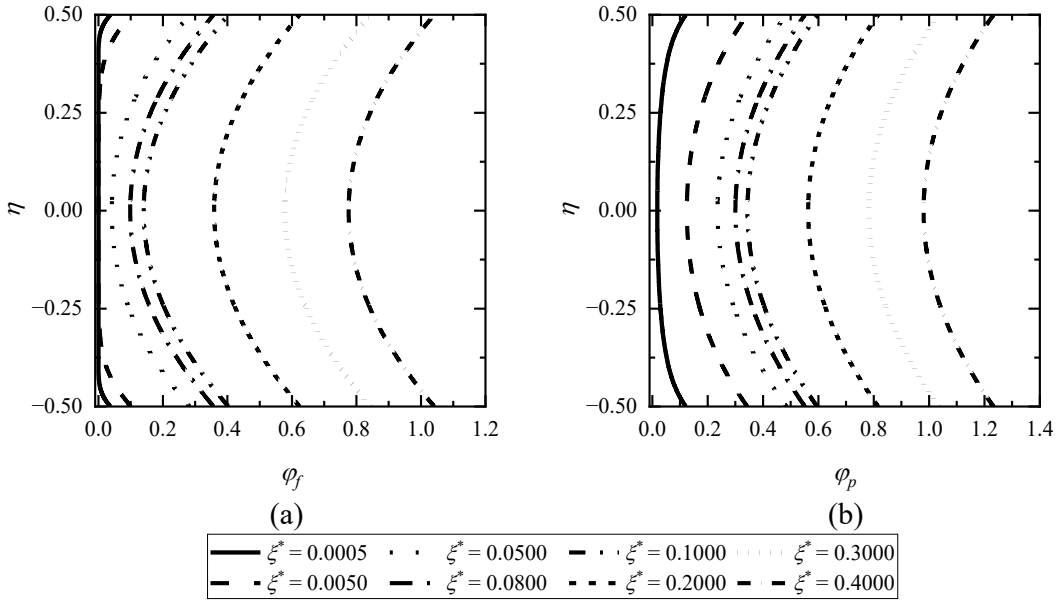

Fig. 3.3: Impact of (a) φ_f and (b) φ_p for distinct ξ^* values for Bi = 10, Pe = 100, M = 1, and κ = 0.1 at Da = 0.001

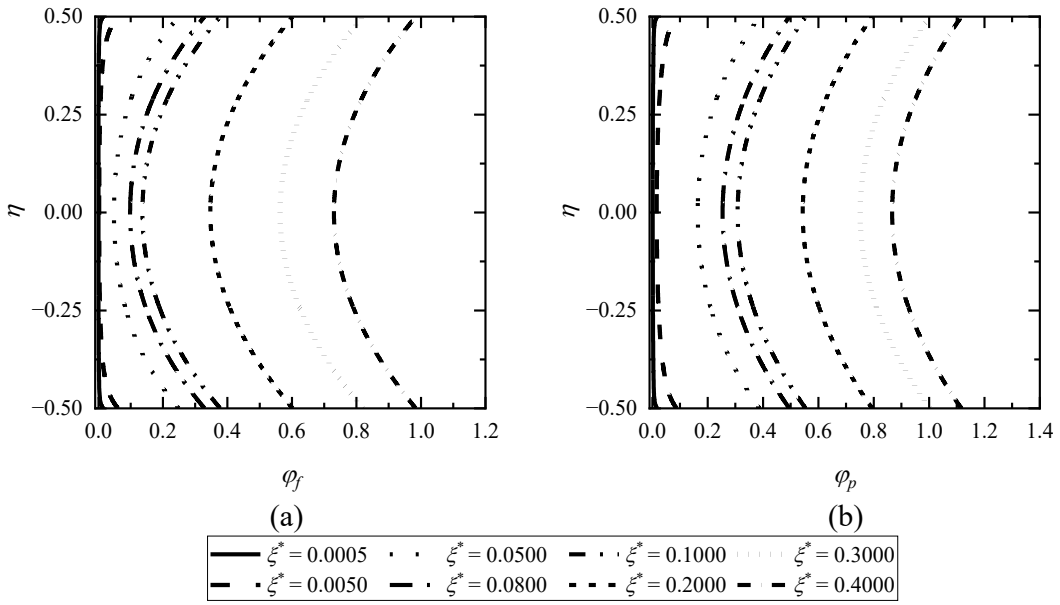

Fig. 3.4: Impact of (a) φ_f and (b) φ_p for distinct ξ^* values for Bi = 10, Pe = 5, M = 65, and κ = 0.1 at Da = 0.001

From Figs. 3.2 and 3.3, as Peclet number, Pe increases (from Pe = 5 to 100), φ_f and φ_p increase for every value of ξ^*. According to this, convection becomes more significant than diffusion when the Peclet number, Pe rises. As a result, mixing and heat exchange within the system are more effectively facilitated. In such situations, convective heat transfer becomes more prevalent. Hence, under the LTNE model,

increasing *Pe* may enhance fluid-porous interaction, promoting better heat exchange between the phases. The Hartmann number, *M*, impacts the system's thermal behaviour in the context of heat transfer under LTNE. From Figs. 3.2(a, b) and 3.4(a, b), as *M* increases, φ_f decreases numerically for all values of ξ^*.

The effect of the Biot number, *Bi*, on the temperature profile is shown in a plot for *Bi* value (*Bi* = 100) in Fig. 3.5(a, b) for φ_f and, φ_p. By comparing Figs. 3.2(a, b) and 3.5(a, b), as *Bi* increases from *Bi* = 10 to 100, φ_p decreases and tends to φ_f (LTE model). It means for the immense value of *Bi*, LTNE tends to LTE. A large Biot number indicates that the internal thermal resistance is dominant, meaning that heat transfer within the porous is less efficient than heat transfer across the porous-fluid interface. Furthermore, the heat transfer within the porous medium approaches thermal equilibrium, and the porous temperature becomes nearly uniform. As a result, the temperature difference between the fluid and porous phases at the interface decreases, and local thermal non-equilibrium effects become less pronounced. In such cases, the system behaviour becomes more like LTE, where the fluid and porous phases are nearly at the same temperature at the interface. This fact is also reported in the literature (Yi et al. [37]; Torabi et al. [117]).

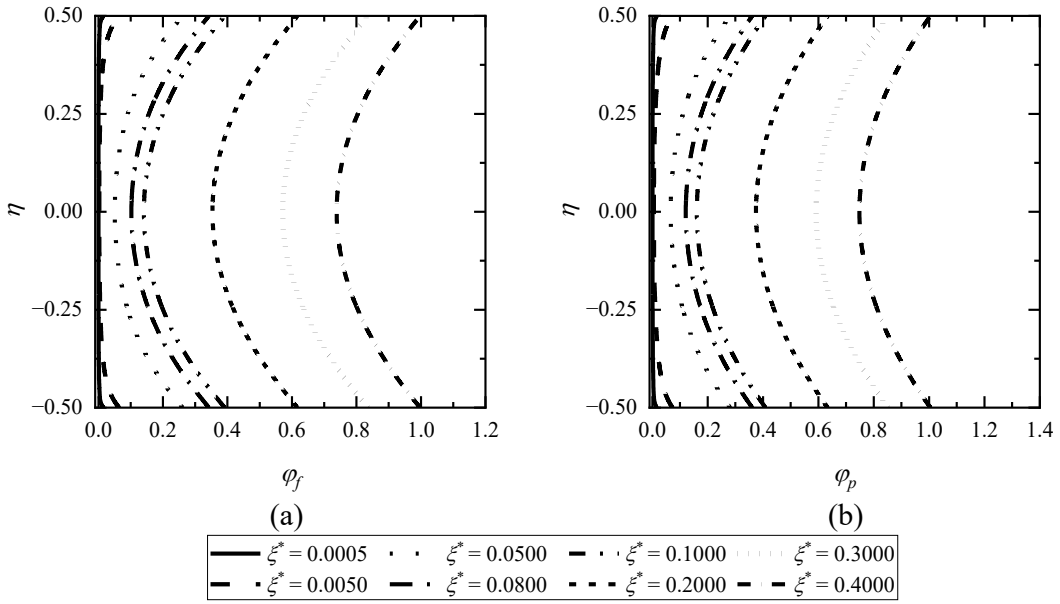

Fig. 3.5: Impact of (a) φ_f and (b) φ_p for distinct ξ^* values for *Bi* = 100, *Pe* = 5, *M* = 1, and κ = 0.1 at *Da* = 0.001

To assess the effect of thermal conductivity ratio, κ $\left(=k_{pe}/k_{fe}\right)$, the plot for the temperature profile is given in Fig. 3.6 for κ = 10. By comparing Figs. 3.2(a, b) and 3.6(a, b), as κ increases from κ = 0.1 to 10.0, φ_f as well as φ_p increase. Heat may be transferred more effectively inside porous materials if the porous phase has more effective thermal conductivity. As a result, the porous phase may experience a greater temperature increase because it can absorb and transport heat more efficiently. From the temperature profiles, it can be observed that $\varphi_p > \varphi_f$ for a low value of *Bi*. This fact is also true in the absence of axial conduction (i.e., $A_c = 0$) and is also discussed in Chapter 2, § 2.7.2.

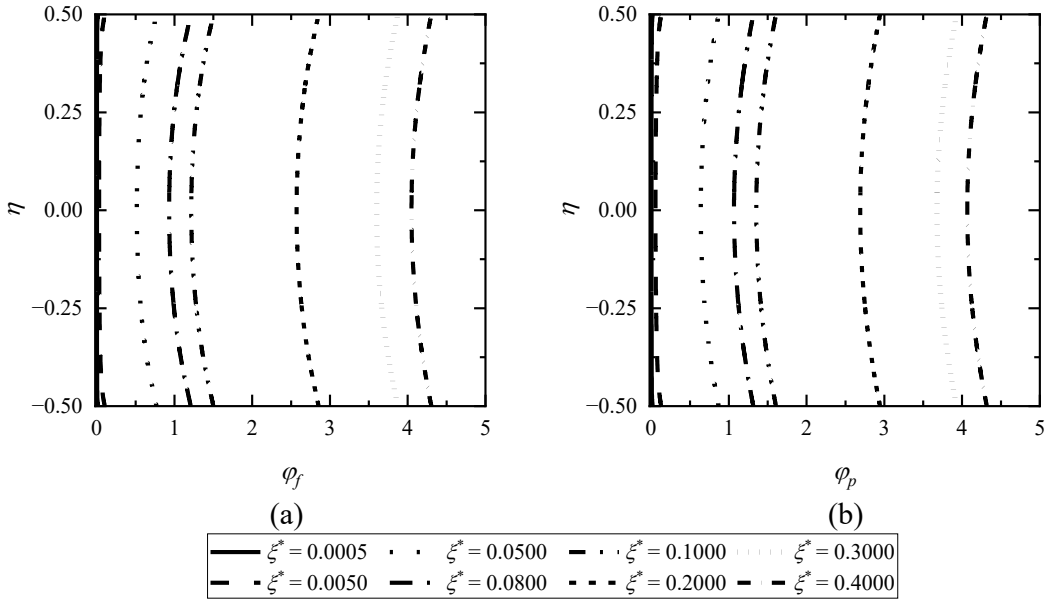

Fig. 3.6: Impact of (a) φ_f and (b) φ_p for distinct ξ^* values for *Bi* = 10, *Pe* = 5, *M* = 1, and κ = 10 at *Da* = 0.001

Dimensionless temperature based on bulk mean temperature in the fluid phase and porous phase:

Dimensionless temperature based on bulk mean temperature in the fluid phase, $\varphi_{b,f}$ and in the porous phase, $\varphi_{b,p}$ are given in Fig. 3.8 for *Da* = 0.005, *M* = 1, *Pe* = 5, *Bi* = 10, and κ = 0.1. From Fig. 3.8, it is clear that $\varphi_{b,f}$ and, $\varphi_{b,p}$ tend to zero for large ξ^* ≥ 0.35 for any *Da*, *M*, *Pe*, *M*, *Bi*, and κ. It means that $\varphi_{b,f}$ and $\varphi_{b,p}$ are invariant with

respect to ξ^* for large ξ^*, which is a fully developed condition. This type of validation is available in Repaka and Satyamurty [151] for LTE.

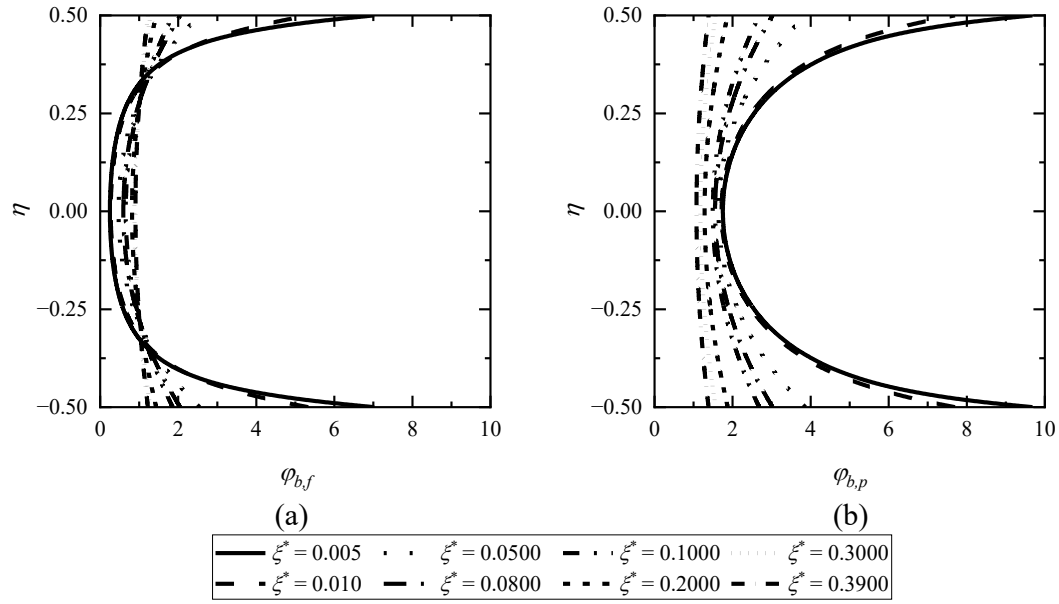

Fig. 3.7: Effect of (a) $\varphi_{b,f}$ and (b) $\varphi_{b,p}$ for various values of Da = 0.005, κ = 0.1, Pe = 5, and Bi = 10 at M = 1

Local Nusselt number

Under conditions of the LTNE model, the local Nusselt number, Nu_ξ number significantly affects the heat transfer behaviour at the porous-fluid interface. In this section, plots with respect to normalized axial distance, ξ^* are given in Figs. 3.8 and 3.9 for various values of Darcy number (Da = 0.001, 0.005, 0.01, 0.05, and 0.1) and Hartmann number (M = 1, 10, 25, 50, and 65). Similar types of plots are given in Figs. 3.10(a, b) and 3.11(a, b) for Nu_ξ vs. ξ^* and for Nu_ξ vs. axial distance, ξ for different values of Pe, Pe = 5, 10, 25, 50, 100, and A_c = 0, respectively for Da = 0.005, M = 1, and κ = 0.1 at Bi = 10 and 100, respectively.

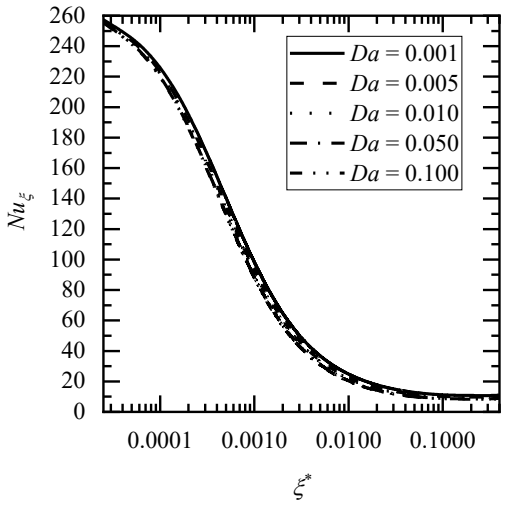

Fig. 3.8: Effect of local Nusselt number, Nu_ξ with ξ^* for various Darcy numbers (Da) at Pe = 5, M = 1, Bi = 10, and κ = 0.1

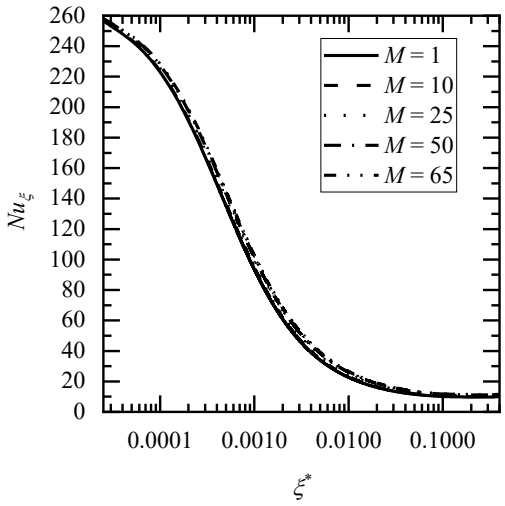

Fig. 3.9: Effect of local Nusselt number, Nu_ξ with ξ^* for various Hartmann numbers (M) at Pe = 5, Da = 0.005, M = 1, Bi = 10, and κ = 0.1

The pattern in the change of Nu_ξ with ξ^* for the channel passing through a porous material is comparable to the trend for the channel with clear fluid flow under the LTE, which has been extensively described (ref. [75]). From Figs. 3.8 to 3.13, it is observed to decrease with increasing ξ^* and tends to the fully developed value for a given Da, M, Bi, Pe, and κ. It can be seen from Figs. 3.10(b) and 3.11(b), that as ξ increases, Nu_ξ also decreases for a given Da, Bi, Pe, and κ. Since the portion of the energy conveyed from the wall manifests as a local enthalpy increase of the fluid in the case of fluid heating, where fluid axial heat conduction is present, the remaining energy is carried upstream via the fluid to the inflow header. Even though thermal energy would warm up the incoming flow, the initial state prevents preheating; hence, the analysis does not include it. As a result, any fluid cross-section has a lower bulk mean temperature, a higher temperature difference between the wall and bulk mean temperatures, and higher wall gradients than the local case with no axial conduction but with the same $T = T_e$ at $\xi^* = 0$. The local Nusselt number rises for a given ξ^* as Pe decreases for finite fluid axial heat conduction. It implies that as Pe lowers, the thermal entrance length ξ^* also grows.

The effect of Da and M is given in Figs. 3.8 and 3.9. According to this, as Da increases, Nu_ξ decreases and tends to the Nusselt number value in the fluid region. It

occurs because the porous medium acts like a clear fluid as its permeability rises. It has been found that $Nu_\xi \rightarrow 8.233$ for $Da \geq 0.2$. It is a value of a fully developed Nusselt number for a clear fluid channel subject to constant wall heat flux. This fact is given in Shah and London [1]. However, the magnetic forces become more dominant at higher Hartmann numbers ($M > 1$), influencing the heat transfer behaviour seen in Fig. 3.9 and, increases with an increase of M. It is because, the presence of a magnetic field can chage the thermal boundary layer at the porous-fluid interface. As a result, the thermal resistance at the contact may rise, increasing the convective heat transfer coefficient (h_ξ) and the value of Nu_ξ .

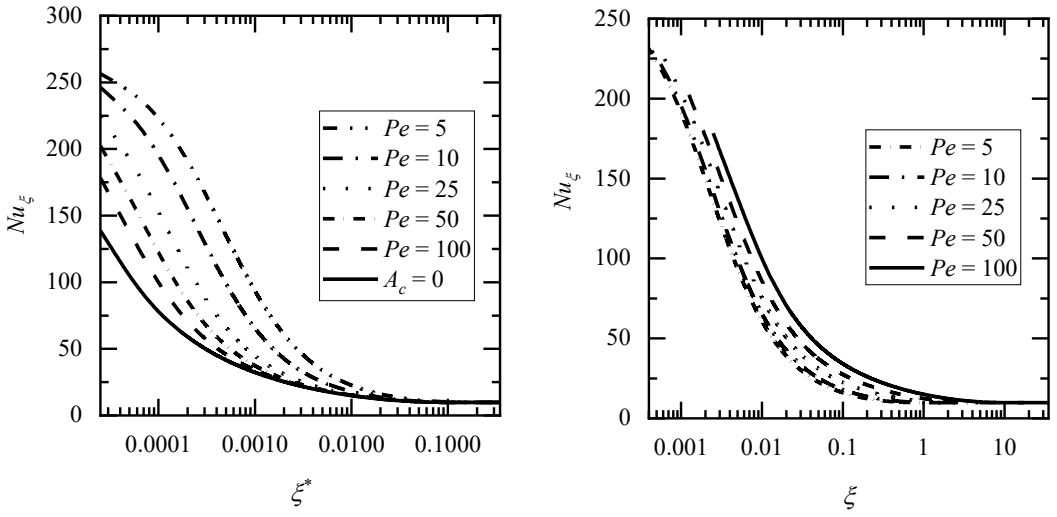

Fig. 3.10: Effect of local Nusselt number (Nu_ξ) with (a) ξ^* (normalized dimensionless axial distance), and with (b) ξ (dimensionless axial distance) for various values of Pe for $\kappa = 0.1$, $Bi = 10$, $M = 1$, and $Da = 0.005$

From Fig. 3.10(a), as Pe increases from 5 to 100, Nu_ξ decreases with each values of ξ^* (for $Da = 0.005$, $M = 1$, $Bi = 10$, and $\kappa = 0.1$) while in Fig. 3.10(b) Nu_ξ increases with each value of ξ, which indicates that convection is more dominant than diffusion. In this regime, Nu_ξ (with ξ) increases as the convective heat transfer becomes more efficient. It happens for all values of parameters Da, M, Bi, and κ. The axial conduction effect is negligible, i.e., $A_c = 0$, for large Pe (≥ 100). This observation is also seen in Fig. 3.11(a, b). Nu_ξ tends to different constant values for large ξ^*. Further, it can be expected that for a large value of Bi, the fully developed values of

Nu_ξ depend on Darcy's number. By comparing Figs. 3.10(a, b) and 3.11(a, b), Nu_ξ decreases as the Biot number, *Bi*, increases. It is due to the dominant behaviour of internal thermal resistance, and the system exhibits substantial LTNE effects. Hence, Nu_ξ decreases as the heat transfer at the interface becomes less efficient due to the temperature difference between the porous and fluid phases.

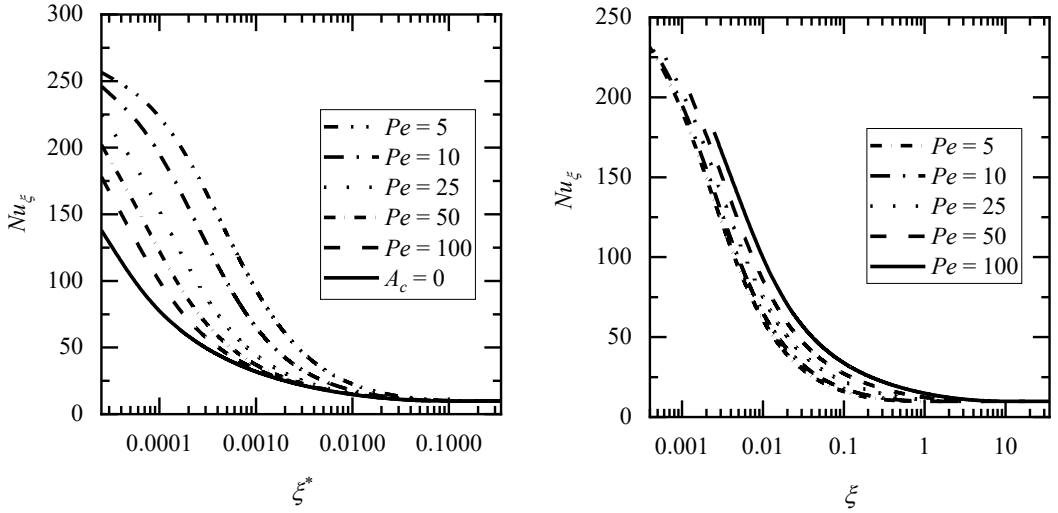

Fig. 3.11: Effect of local Nusselt number (Nu_ξ) with (a) ξ^* (normalized dimensionless axial distance), and with (b) ξ (dimensionless axial distance) for various values of *Pe* for κ = 0.1, *Bi* = 100, *M* = 1, and *Da* = 0.005

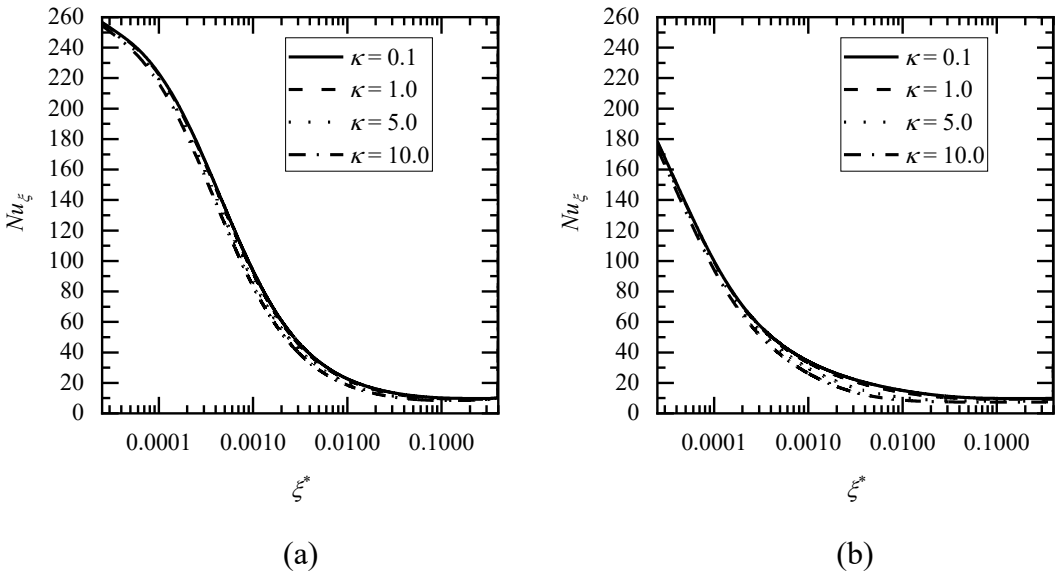

Fig. 3.12: Effect of local Nusselt number (Nu_ξ) with ξ^* for *Da* = 0.005, *M* = 1, and *Bi* = 10 for various values of κ for (a) *Pe* = 5, and (b) *Pe* = 100

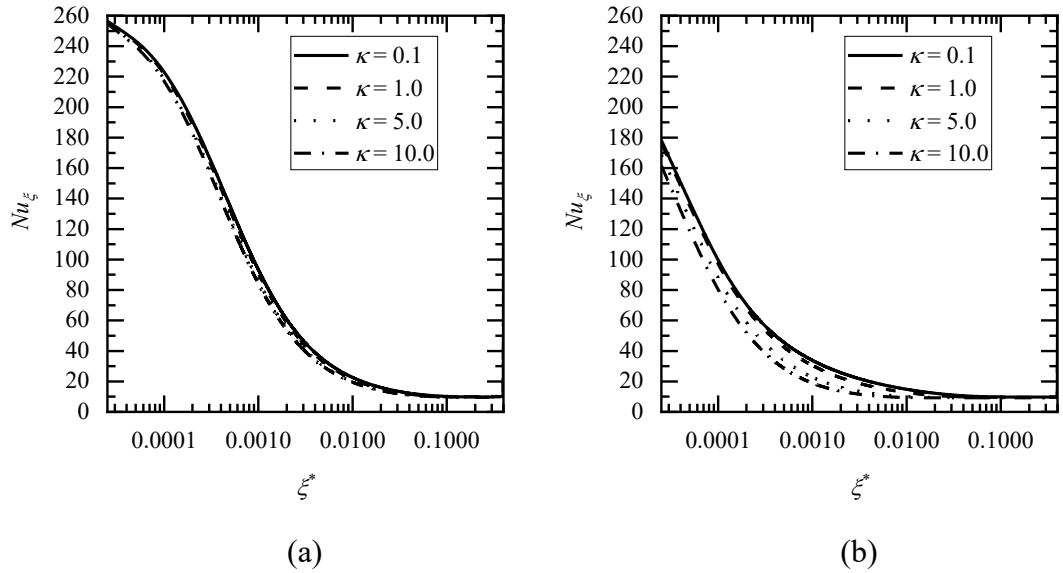

Fig. 3.13: Effect of local Nusselt number (Nu_ξ) with ξ^* for Da = 0.005, M = 1, and Bi = 100 for various values of κ for (a) Pe = 5, and (b) Pe = 100

The effect of thermal conductivity ratio, κ on Nu_ξ with ξ^* is also analyzed and illustrated in Fig. 3.12(a) and Fig. 3.12 (b) at Da = 0.005, M = 1, Bi = 10 and for Pe = 5 and 100, respectively, and, for large Bi, Bi = 100, plots with similar pattern are given in Fig. 3.13(a, b). The significant findings are seen in Figs. 3.12 and 3.13 as (i) at a given Pe, the value of Nu_ξ is less affected by Bi and, (ii) regarding κ $\left(=k_{pe}/k_{fe}\right)$, a significant change has occurred. For all Pe and Bi, Nu_ξ diminishes as κ rises, and (iii) by comparing (a) and (b) of Figs. 3.12 and 3.13, Nu_ξ decreases for all the values of κ as Pe increases at a given Bi. (iv) As Bi increases, Nu_ξ decreases, and this effect is more at a significant value of Pe, and κ. The observed behaviour is consistent with Nield et al. [34]'s boundary condition of a constant wall temperature. A higher ratio, κ allows for the formation of a porous medium in which the porous phase's effective thermal conductivity is greater than that of the fluid phases. As a result, Nu_ξ for the porous material-filled channel falls since it is directly related to the fluid phase's convective heat transmission properties.

3.6 Conclusion

Forced convection in the entry region of a porous material-filled channel under LTNE with axial conduction has been studied numerically. When axial conduction is included, it becomes evident that the dimensionless temperature and other derived values are highly dependent on the Peclet number. This dependence continues when normalised dimensionless axial distance is introduced. The following are the main findings of the present investigation:

i. In the presence of axial conduction, as the Hartmann number increases, φ_f and φ_p decrease. However, LTNE tends to be LTE for high Biot numbers.

ii. As the thermal conductivity ratio, κ increases, φ_f and φ_p increase for each value of ξ^* and for a given *Da*, *Pe*, *M*, and *Bi*. Also, values of φ_p are larger than φ_f.

iii. Under LTNE, $\varphi_{b,f}$ and $\varphi_{b,p}$ are invariant with respect to ξ^* for large ξ^*, which makes the onset of a fully developed condition.

iv. Local Nusselt number, Nu_ξ depends on the values of *Pe*, *Bi*, κ, and *Da.*

v. Axial conduction effect is negligible for a large value of Peclet number, *Pe* ($\geq$ 100) in the LTNE also, except very near the entry.

vi. Local Nusselt number, Nu_ξ decreases as thermal conductivities and Biot numbers increase. It increases with an increase in Hartmann's number.

vii. Nu_ξ decreases as ξ^* increases for all *Da*, *Bi*, and κ and reaches as the fully developed values for $\xi^* > 0.35$. However, it decreases as *Pe* decreases at a given ξ.

viii. For a considerable value of *Da*, $Da \geq 0.2$, $Nu_\xi \rightarrow 8.233$. It is the value of a fully developed Nusselt number in a clear fluid channel.

Chapter 4

Forced Convection Heat Transfer at the Entry Region of the Porous Channel with Viscous Dissipation

4.1 Introduction

Viscous dissipation is essential to forced convective heat transfer, mainly when dealing with fluid flow in channels or pipes with significant velocity gradients. When a fluid flows through a channel, it experiences frictional forces due to interaction with the channel walls, resulting in energy loss in the form of heat. This article employs the effect of two viscous dissipation models, the clear fluid compatible (CFC) model and the form drag (FD) model at the thermal entrance. The thermal characteristics of fluid flowing through a porous material immersed in a parallel plate channel have been studied. It is investigated numerically under the local thermal non-equilibrium model (LTNE). The channel walls are subjected to constant heat flux boundary conditions. Numerical solutions have been obtained for the thermal field. The increase in Brinkman number and thermal conductivity ratio improves the temperature distribution. The parametric structure of this study permitted mapping LTNE and local thermal equilibrium (LTE) areas across a wide range of these dimensionless parameters. Enhancement in the local Nusselt number is obtained in CFC model compared to the value in FD model. The effect of the magnetic field and Forchheimer number are neglected in the present study. The definitions of velocities, dimensionless temperatures, and other notations remain the same as those employed in Chapter 2.

4.2 Mathematical Model

The parallel plate channel's schematic model and coordinate system are shown (Chapter 3, § Fig. 3.1). The thermal field includes viscous dissipation. Porous and fluid regions are in LTNE. The porous medium is isotropic and homogeneous. Heat generation and axial conduction are negligible. The thermophysical properties are constant.

Governing Equations

The steady-state conservation of thermal energy equations of the fluid and porous phases are given by:

Fluid phase

$$\left(\rho C_p\right)\left(u\frac{\partial T_f}{\partial x^*}\right)=k_{fe}\frac{\partial^2 T_f}{\partial y^{*2}}+a_{pf}h_{pf}\left(T_p-T_f\right)+\psi_i \tag{4.1}$$

Porous phase

$$k_{pe}\frac{\partial^2 T_p}{\partial y^{*2}}-a_{pf}h_{pf}\left(T_p-T_f\right)=0 \tag{4.2}$$

In Eqs. (4.1) and (4.2), ρ is density, C_p is the specific heat, T_f is the fluid phase temperature, T_p is the porous phase temperature, k_{fe} is the effective fluid thermal conductivity, k_{pe} is the effective porous thermal conductivity, respectively. a_{pe} is the interfacial area per unit volume of the porous media and h_{pf} is the porous-to-fluid heat transfer coefficient in the literature.

In Eq. (4.1), ψ_{i} is the dissipation function, (i) the clear fluid compatible (CFC) model due to Al-Hadhrami et al. [139], and (ii) the form drag (FD) model due to Nield [140].

CFC model is given below:

$$\psi_1=\left[\frac{\mu}{K}u^2+\mu_e\left(\frac{du}{dy^*}\right)^2\right] \tag{4.3}$$

FD model is as follows:

$$\psi_2=\left[\frac{\mu}{K}u^2-\mu_e u\frac{d^2u}{dy^{*2}}\right] \tag{4.4}$$

The boundary conditions for the governing equations and the dimensionless variables are the same as in Chapter 2, § Eqs. (2.6) and (2.7), and Eq. (2.9).

The governing equations (Eqs. (4.1) and (4.2)) in dimensionless form after applying the dimensionless variables (Chapter 2, § Eq. (2.9)) are given by

$$k_1 U^N(\eta)\frac{\partial \varphi_f}{\partial \xi^*} = \frac{\partial^2 \varphi_f}{\partial \eta^2} + Bi\ \kappa\left(\varphi_p - \varphi_f\right) + \chi_i \tag{4.5}$$

$$\frac{\partial^2 \varphi_p}{\partial \eta^2} - Bi\left(\varphi_p - \varphi_f\right) = 0 \tag{4.6}$$

In Eq. (4.5), χ_i is the dimensionless form of viscous dissipation models and is given by

CFC model is given below:

$$\chi_1 = Br\left[\left(U^N\right)^2 + \frac{Da}{\varepsilon}\left(\frac{dU^N}{d\eta}\right)^2\right] \tag{4.7}$$

FD model is as follows:

$$\chi_2 = Br\left[\left(U^N\right)^2 - \frac{Da}{\varepsilon}U^N\frac{d^2U^N}{d\eta^2}\right] \tag{4.8}$$

The normalized axial distance, ξ^* can be defined as:

$$\xi^* = \frac{\xi}{Pe} \tag{4.9}$$

In Eq. (4.9), *Pe* is the Peclet number defined in Chapter 3 §, Eq. (3.17).

In Eqs. (4.5) to (4.8) , *Da*, *Br, Bi,* and κ denote the Darcy number, Brinkman number, Biot number, and thermal conductivity ratio, respectively; however, ε and k_1 represent the ratio between the viscosity of the fluid to effective viscosity of the porous medium, and fluid thermal conductivity to effective fluid thermal conductivity, respectively, and it can be defined as follows:

$$Da = \frac{K}{H^2} \tag{4.10}$$

$$Br = \frac{u_{ref}^2 \mu H}{q_w K} \tag{4.11}$$

$$Bi = \frac{a_{pf} h_{pf} H^2}{k_{pe}} \tag{4.12}$$

$$\kappa = \frac{k_{pe}}{k_{fe}} \tag{4.13}$$

$$\varepsilon = \frac{\mu}{\mu_e} \tag{4.14}$$

$$k_1 = \frac{k_f}{k_{fe}} \tag{4.15}$$

In Eq. (4.15), k_f is the thermal conductivity in the fluid region. $U^N(\eta)$ is normalized velocity given in Chapter 3, § Eqs. (3.32) is used to solve the coupled system of equations (Eq. (4.5) and (4.6)) by taking the Hartmann number ($M = 0$).

Dimensionless Boundary Conditions

$$\left.\begin{aligned} \frac{\partial \varphi_f}{\partial \eta} = k_1, \quad \frac{\partial \varphi_p}{\partial \eta} = k_2 \qquad \text{at} \quad \eta = \frac{1}{2} \\ \frac{\partial \varphi_f}{\partial \eta} = -k_1, \quad \frac{\partial \varphi_p}{\partial \eta} = -k_2 \quad \text{at} \quad \eta = -\frac{1}{2} \end{aligned}\right\} \tag{4.16}$$

$$\varphi_{f,p}(0,\eta) = 0, \quad \text{for} \; -\frac{1}{2} < \eta < \frac{1}{2} \tag{4.17}$$

$$\varphi_f = \varphi_p = \varphi_{interface} \tag{4.18}$$

In Eq. (4.16), the ratio, k_2 is defined by

$$k_2 = \frac{k_f}{k_{pe}} \tag{4.19}$$

4.3 Local Nusselt Number

The local heat transfer coefficient (h_ξ) is determined at the wall $y^* = H/2$ adjacent to the porous medium.

$$-k_{fe}\left.\frac{\partial T_f}{\partial y^*}\right|_{y^*=\frac{H}{2}} = h_\xi\left(T_w - T_b\right) \tag{4.20}$$

In Eq. (4.20), the bulk mean temperature (T_b) is denoted as follows:

$$T_b = \frac{\int_{-H/2}^{H/2} uT_f dy^*}{\int_{-H/2}^{H/2} u dy^*} \tag{4.21}$$

Upon dimensionless variables, the local Nusselt number at $\eta = 1/2$, Nu_ξ is given by:

$$Nu_\xi = \frac{h_\xi\left(2H\right)k_1}{k_f} = \frac{-2\left(\left.\frac{\partial \varphi_f}{\partial \eta}\right)\right|_{\eta=\frac{1}{2}}}{\left(\varphi_w - \varphi^*\right)} = \frac{2}{\left(\varphi^* - \varphi_w\right)} \tag{4.22}$$

In Eq. (4.22), φ_w and φ^* are defined in Chapter 2, § Eqs. (2.33) and (2.34) and φ^* is evaluated by Eq. (2.35) (Chapter 2).

4.4 Numerical Methodology

The successive accelerated replacement (SAR) scheme is used to solve the coupled thermal energy equations (Eqs. (4.5) and (4.6)), along with the thermal boundary conditions on φ, as specified in Eqs. (4.16) and (4.17). This scheme is briefly discussed in Chapter 2, § 2.6, and utilized in Chapters 2 and 3.

4.5 Numerical Results and Discussions

Numerical solutions have been obtained for the thermal energy two-equation model (LTNE model) in a channel filled with a porous medium. It is assumed that $k_1 = k_f / k_{fe} = 1$, $k_2 = k_f / k_{se} = 1$, and $\varepsilon = \mu / \mu_{eff} = 1$. $0.001 \le Da \le 0.1$, $10 \le Bi \le 100$, $0.8 \le Br \le 100$, and $0.1 \le \kappa \le 10$ are the ranges used for parameters.

4.5.1 Thermal Field

In this section, we analyze the dimensionless temperature profiles for both phases (fluid and porous), wall temperature, and the local Nusselt number for the flow through the channel filled with porous material for the two dissipation models. For the CFC model, the temperature in the fluid and porous phases and the local Nusselt number is denoted as $\varphi_{f,CFC}$, $\varphi_{p,CFC}$, and $Nu_{\xi,\,CFC}$. While for FD model, it is denoted as $\varphi_{f,FD}$, $\varphi_{p,FD}$, and $Nu_{\xi,\,FD}$. The notation for wall temperature for the CFC model is given by $\varphi_{wf,CFC}$, and $\varphi_{wp,CFC}$. Plots are given for various values of normalized axial distance, ξ^*, to examine the effects of the Brinkman number, *Br*, Biot number, *Bi*, and thermal conductivity ratio, κ in thermally developing regions for both models.

The CFC viscous dissipation model:

In the case of the CFC model, plots are given for temperature in both the fluid and porous phases in Figs. 4.1(a ,b) and 4.2(a, b) for Brinkman number, *Br* = 0.8 and 20, respectively, at a given value of parameters involving Darcy number (*Da*), Biot number (*Bi*), and thermal conductivity ratio (κ) (*Bi* = 10, *Da* = 0.001, and κ = 0.1). From these

plots, as ξ^* increases, $\varphi_{f,CFC}$ and $\varphi_{p,CFC}$ increase for each value of the given parameters. At a large value of ξ^*, $\varphi_{f,CFC}$ and $\varphi_{p,CFC}$ do not tend to zero without dissipation. Since, at large ξ^*, the conduction term is balanced by the viscous dissipation term.

As Brinkman number *Br* increases from *Br* = 0.8 to 20, $\varphi_{f,CFC}$ and $\varphi_{p,CFC}$ grow. This is because the two-phase interaction behaves as a heat source in the porous medium. At a significant value of *Br*, the temperature rise will be higher, and the heat conduction will be slower. In this model, it is observed that $\varphi_{p,CFC} > \varphi_{f,CFC}$, which indicates the presence of LTNE model, when channel walls are subjected to constant wall heat flux.

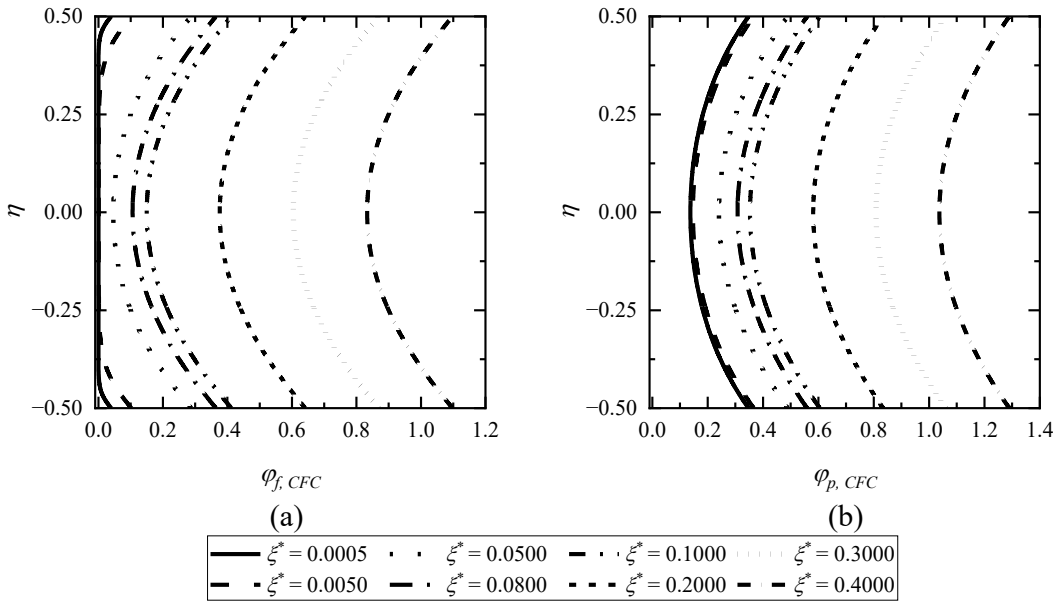

Fig. 4.1: Impact of (a) $\varphi_{f,CFC}$ and (b) $\varphi_{p,CFC}$ for distinct ξ^* values for *Bi* = 10, *Br* = 0.8, and κ = 0.1 at *Da* = 0.001

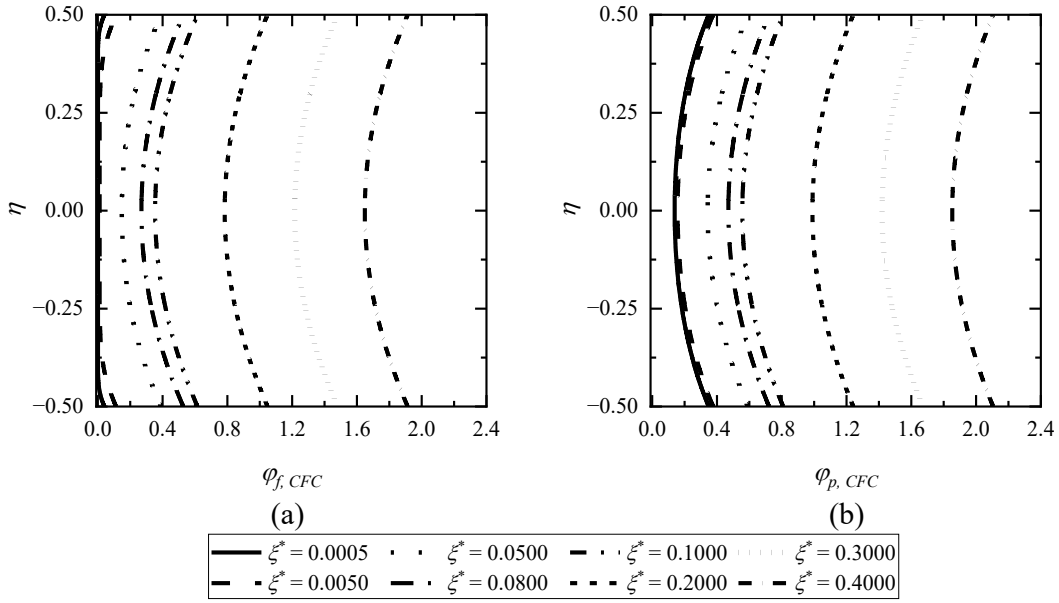

Fig. 4.2: Impact of (a) $\varphi_{f,CFC}$ and (b) $\varphi_{p,CFC}$ for distinct ξ^* values for Bi = 10, Br = 20.0, and κ = 0.1 at Da = 0.001

The FD viscous dissipation model:

In Fig. 4.3(a, b), dimensionless temperature plots are given for the form drag model (FD model) for distinct values of ξ^* at Bi = 10, Da = 0.001, κ = 0.1, and Br = 0.8. From the Figure, temperatures $\varphi_{f,FD}$ and $\varphi_{p,FD}$ increase with an increase in ξ^*. The pattern of the temperature of this model (FD model) is similar to the plots of CFC model. Quantitatively, there is a slight decrease in the dimensionless temperature. As a result, the FD model's temperatures are lower than those in the CFC model under LTNE.

In both the dissipation models, it is observed that the wall temperatures $\varphi_{wf}\big|_{\eta=+1/2} = \varphi_{wf}\big|_{\eta=-1/2}$ and $\varphi_{wp}\big|_{\eta=+1/2} = \varphi_{wp}\big|_{\eta=-1/2}$, which demonstrate the channel's symmetry. For both the dissipation models (CFC and FD models), symmetric profiles of φ_f and φ_p can be seen at $\eta = 0$. Temperatures, φ_f and φ_p have a minimum value at the centre of the channel (at $\eta = 0$) and attain maximum value at the walls.

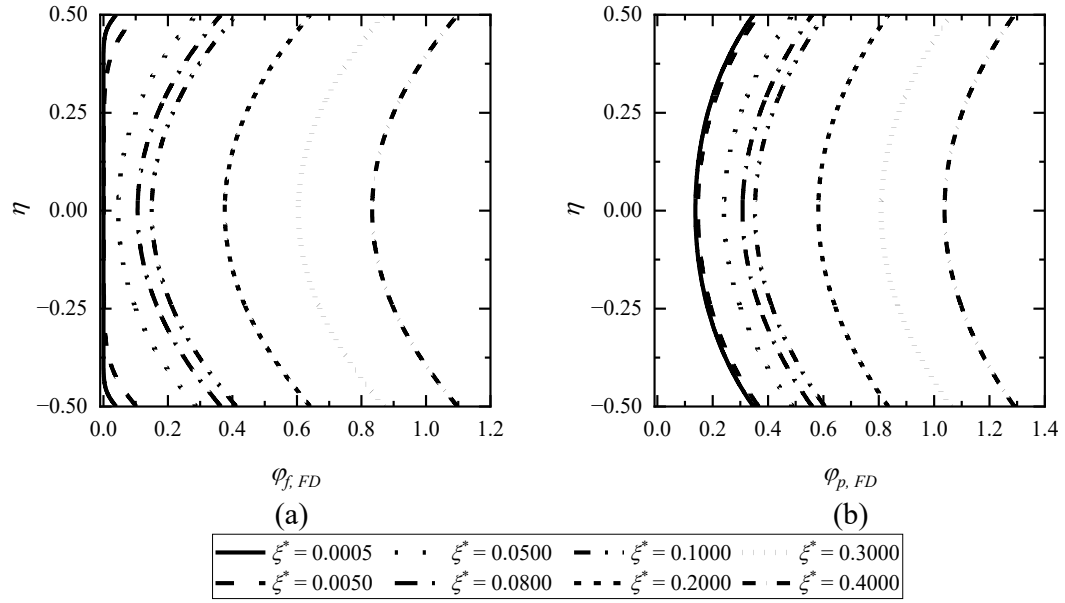

Fig. 4.3: Impact of (a) $\varphi_{f,FD}$ and (b) $\varphi_{p,FD}$ for distinct ξ^* values for Bi = 10, Br = 0.8, and κ = 0.1 at Da = 0.001

The behaviour of the thermal field under LTNE at the entry:

Under LTNE, the behaviour of the thermal field at the entry is discussed for both viscous dissipation models in this section. At an entry point ξ^* = 0.005, plots are given at distinct values of Brinkman number, Br for κ = 0.1 and Bi = 50, for Da = 0.001 and 0.05. For the CFC model, temperature plots ($\varphi_{f,CFC}$ and $\varphi_{p,CFC}$) are given in Fig. 4.4(a, b); for the FD model, temperature plots ($\varphi_{f,FD}$ and $\varphi_{p,FD}$) are shown in Fig. 4.5(a, b). In the case of CFC model, it is clear that as Br increases, $\varphi_{f,CFC}$ and $\varphi_{p,CFC}$ increase for each value of Da. Similarly, in the case of the FD model, $\varphi_{f,FD}$ and $\varphi_{p,FD}$ grow with an increase in Br. By comparing Figs 4.4 and 4.5, in both the phases, temperatures in the FD model are less than temperatures in CFC model (i.e., $\varphi_{f,p,FD} < \varphi_{f,p,CFC}$). Hence, more temperature plots are given for CFC model.

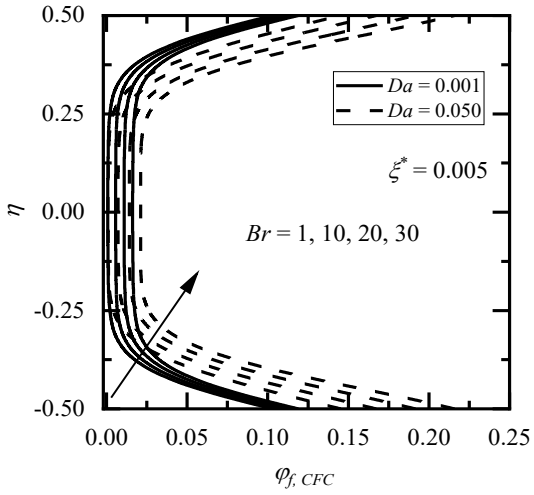

(a)

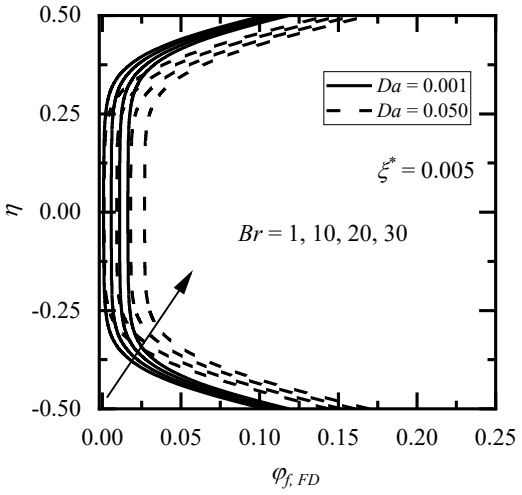

(a)

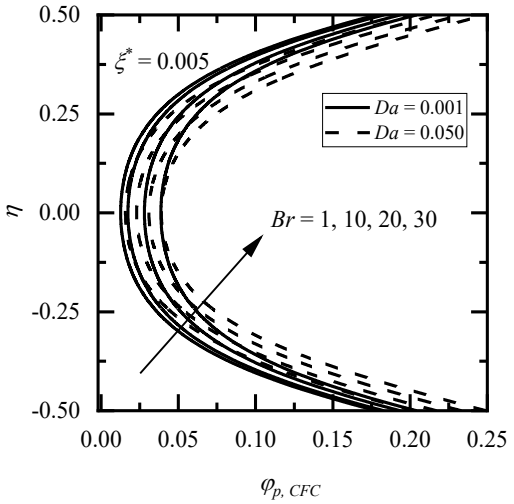

(b)

Fig. 4.4: Impact of (a) $\varphi_{f,CFC}$ and (b) $\varphi_{p,CFC}$ for various values of *Br* at ξ^* = 0.005 at *Da* = 0.001 and 0.05 for *Bi* = 50 and κ = 0.1

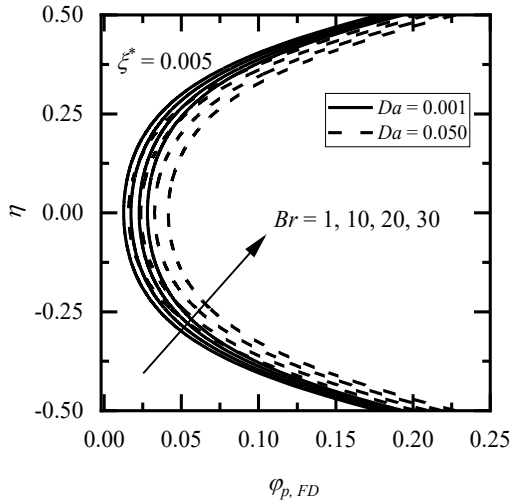

(b)

Fig. 4.5: Impact of (a) $\varphi_{f,FD}$ and (b) $\varphi_{p,FD}$ for various values of *Br* at ξ^* = 0.005 at *Da* = 0.001 and 0.05 for *Bi* = 50 and κ = 0.1

Effect of Biot number (Bi) and thermal conductivity ratio (κ) on temperature:

To analyze the effect of *Bi*, plots are given in Fig. 4.6(a, b) for a considerable value of *Bi*, *Bi* = 100 at *Da* = 0.001, *Br* = 0.8, and κ = 0.1. Comparing Figs. 4.1(a, b) and Figs. 4.6(a, b), It can be said that *Bi* affects the temperature profiles. As *Bi* increases, $\varphi_{f,CFC}$, decreases for all values of ξ^*, *Da*, and κ. Additionally, it is apparent that when *Bi* rises, $\varphi_{p,CFC}$ decreases and tends to $\varphi_{f,CFC}$. It means that for a significant value of *Bi*, LTNE tends to LTE. The literature reports this fact (Dehghan et al. [126]). Also, in the absence of dissipation models, this fact is true and discussed in previous Chapters (Chapters 2

and 3). The increased Biot number, *Bi*, indicates a more intense internal heat exchange between the porous and fluid phases of the porous material, which reduces the temperature difference between the two phases (i.e., the LTE condition). Mathematically, as $Bi \to \infty$, $\varphi_{p,CFC} \to \varphi_{f,CFC}$ (i.e., LTNE tends to LTE) from Eqs. (4.5) and (4.6). In the absence of the dissipation term (*Br*) in the fluid phase energy equation, this phenomenon also holds in tubes with constant wall temperature boundary conditions, as stated in Khashan et al. [35].

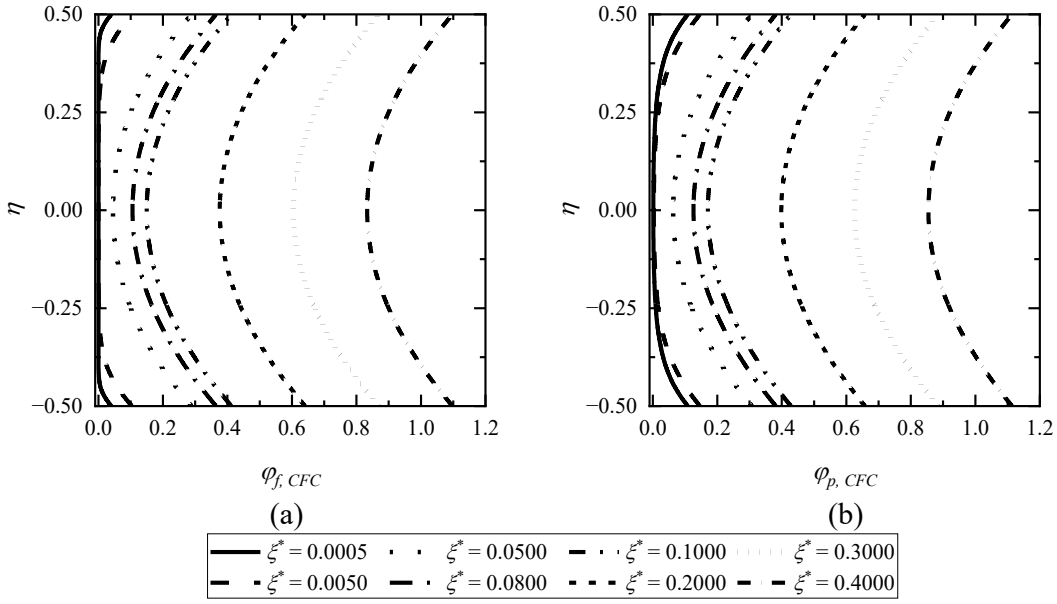

Fig. 4.6: Impact of (a) $\varphi_{f,CFC}$ and (b) $\varphi_{p,CFC}$ for distinct ξ^* values for *Bi* = 100, *Br* = 0.8, and κ = 0.1 at *Da* = 0.001

To access the effect of thermal conductivity ratio, κ, on $\varphi_{f,CFC}$ and $\varphi_{p,CFC}$, the plots are given for distinct values of κ, (κ = 0.1, 1.0, 5.0, and 10.0) for *Da* = 0.001, *Bi* = 10, and *Br* = 0.8 for different values of ξ^* in Fig. 4.7(a, b). Comparing Fig. 4.1(a, b) with Fig. 4.7(a, b), It can be said that the thermal conductivity ratio, κ affects the temperature profiles. From this comparison, it is clear that $\varphi_{f,CFC}$ and $\varphi_{p,CFC}$ increases with an increase in the ratio, κ. Additionally, one can see from Fig. 4.1 to 4.6 that $\varphi_p > \varphi_f$ in both models (CFC and FD models). This finding is stated in the previous chapters when the viscous dissipation is eliminated from the energy equation in the fluid phase.

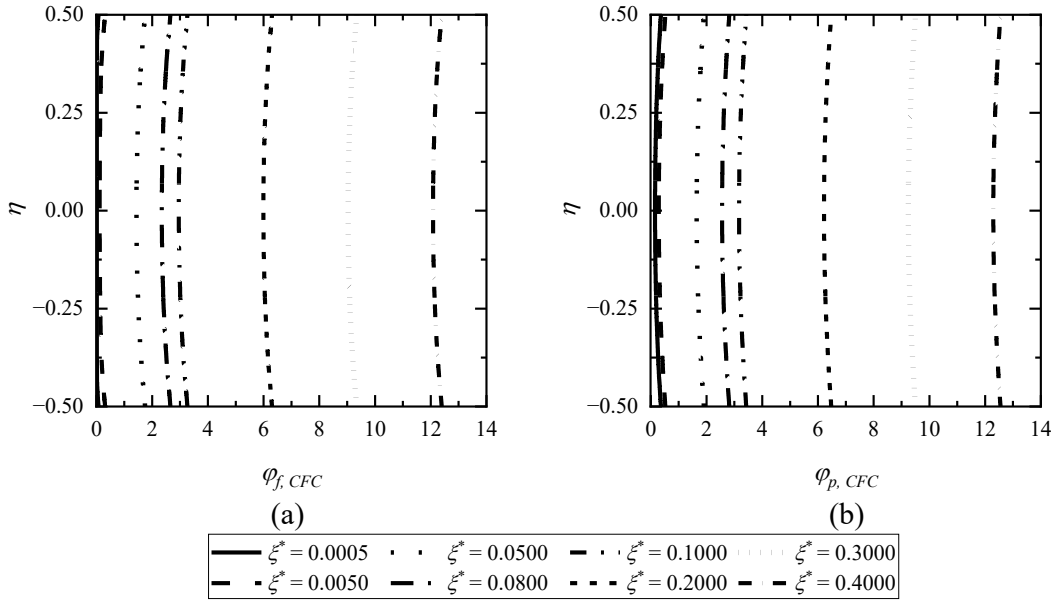

Fig. 4.7: Impact of (a) $\varphi_{f,CFC}$ and (b) $\varphi_{p,CFC}$ for distinct ξ^* values for Bi = 100, Br = 0.8, and κ = 10.0 at Da = 0.001

Wall temperature for the CFC model

Wall temperature profiles are provided so that the impact of the pertinent factors may be seen since wall temperatures are not known because of the constant heat flux at the walls. With ξ^*, wall temperature variations in fluid ($\varphi_{wf,CFC}$) and porous phases ($\varphi_{wp,CFC}$) for Bi = 10, and κ = 0.1 for Br = 0.8, and 10 are demonstrated in Fig. 4.8. For all Br values, $\varphi_{wf,CFC}$ and $\varphi_{wp,CFC}$ rise as ξ^* rises. When $\xi^* > 0.03$, $\varphi_{wf,CFC}$ and $\varphi_{wp,CFC}$ raise initially nonlinearly and later linearly. When a constant heat flow is applied to the channel walls, this is the prerequisite for the onset of a fully developed temperature field. From Fig. 4.8, it can be seen that $\varphi_{wp,CFC} > \varphi_{wf,CFC}$ because the heat transfer from the fluid to the porous increases the temperature of the porous wall more than the fluid wall.

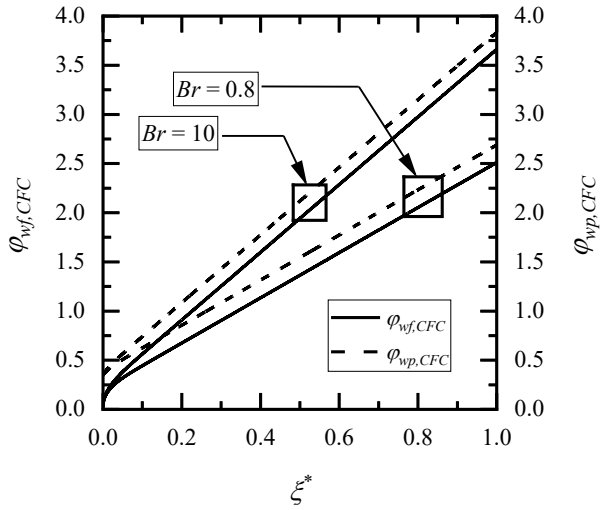

Fig. 4.8: Effect of $\varphi_{wf,\,CFC}$ and $\varphi_{wp,\,CFC}$ with ξ^* at $Da = 0.01$, $\kappa = 0.1$, and $Bi = 10$ for $Br = 0.8$, and 10

Local Nusselt number

In this section, the discussion is given for the local Nusselt number for the CFC model ($Nu_{\xi,\,CFC}$) and the local Nusselt number for the FD model ($Nu_{\xi,\,FD}$) with respect to normalized axial distance (ξ^*) for distinct values of various parameters, *Da*, *Br*, *Bi*, and κ. According to the plots and tables, increasing ξ^* causes a decrease in $Nu_{\xi,\,CFC}$ and $Nu_{\xi,\,FD}$. This is because the local Nusselt number falls as the fluid traverses downstream in the channel until it achieves a constant value.

Analyzing the effect of Brinkman number, *Br* and Darcy number, *Da* on $Nu_{\xi,\,CFC}$, the plots are given in Fig. 4.9(a, b) at $\kappa = 0.1$ and $Bi = 10$ for (a) $Da = 0.005$, and (b) $Da = 0.05$, respectively, for distinct values of *Br*. From Fig. 4.9(a, b), as *Br* increases, it decreases. This result is also accurate under the LTE model and discussed by Arici and Aydin [162]. Moreover, from these figures, as *Da* rises, $Nu_{\xi,\,CFC}$ decreases. The effect of the Biot number, *Bi,* on $Nu_{\xi,\,CFC}$ is given in Table 4.1. It shows that $Nu_{\xi,\,CFC}$ decreases with an increase in *Bi* for each value of *Br* and ξ^*.

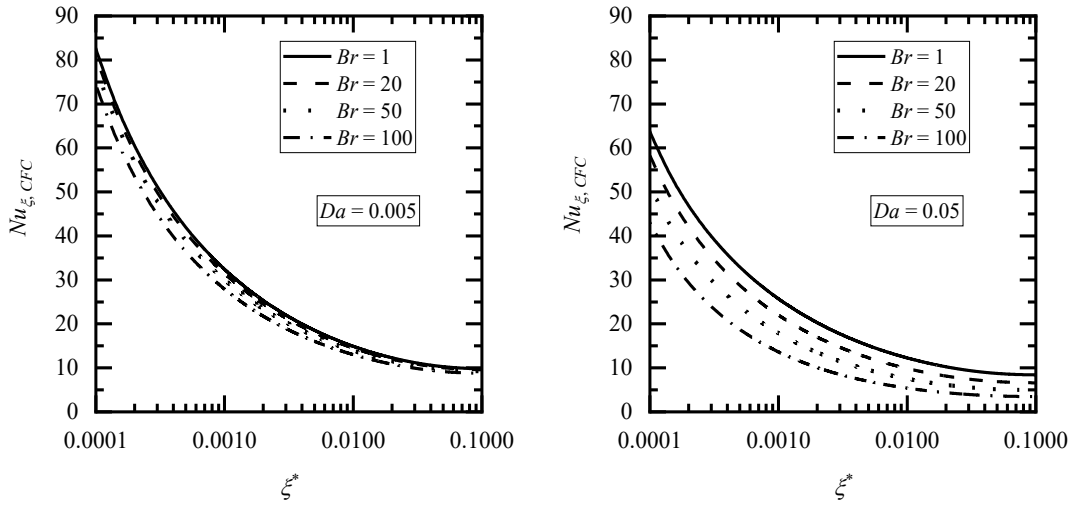

Fig. 4.9: Variation in $Nu_{\xi,\,CFC}$ with ξ^* for distinct values of *Br* at κ = 0.1 and *Bi* = 10 for (a) *Da* = 0.005, and (b) *Da* = 0.05

Table 4.1: Effect of *Bi* on $Nu_{\xi,\,CFC}$ for various values of *Br* and ξ^*

$Nu_{\xi,\,CFC}$				
	Bi = 10		*Bi* = 100	
ξ^*	*Br* = 1	*Br* = 20	*Br* = 1	*Br* = 20
0.001	30.3878	28.9232	30.0173	28.5970
0.005	17.2612	16.3520	17.0521	16.1775
0.050	9.7385	9.2675	9.7318	9.2307

Table 4.2: Effect of parameters *Da*, *Br*, and *Bi*, on $Nu_{\xi,\,FD}$ for various values of ξ^*

	$Nu_{\xi,\,FD}$							
	Da = 0.01				*Da* = 0.05			
	Bi = 10		*Bi* = 100		*Bi* = 10		*Bi* = 100	
ξ^*	*Br* = 1	*Br* = 20	*Br* = 1	*Br* = 20	*Br* = 1	*Br* = 20	*Br* = 1	*Br* = 20
0.001	30.4690	30.4687	30.0959	30.0957	26.4088	26.4086	26.0872	26.0870
0.005	17.3118	17.3113	17.1007	17.1002	15.2643	15.2640	15.0991	15.0988
0.050	9.7645	9.7630	9.7620	9.7605	8.8689	8.8679	8.8907	8.8896

In the case of the FD model, for each value of ξ^*, the effect of parameters, *Da*, *Bi*, and *Br*, on the local Nusselt number for the FD model, $Nu_{\xi,\,FD}$ is given in Table 4.2. From Table 4.2, $Nu_{\xi,\,FD}$ decreases with an increase of *Da*. However, there is significantly smaller decrease in the values of $Nu_{\xi,\,FD}$ with an increase in the Brinkman number, *Br* and Biot number, *Bi*.

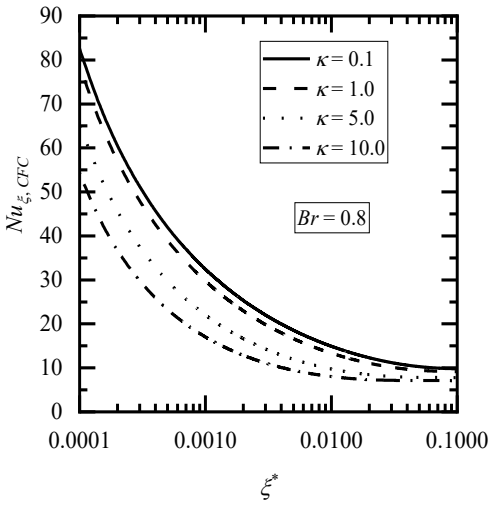

(a)

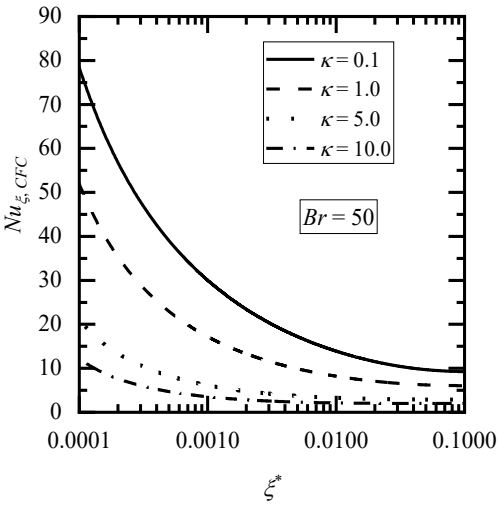

(b)

Fig. 4.10: Variation in $Nu_{\xi,\,CFC}$ with ξ^* for distinct values of κ at $Bi = 10$ and $Da = 0.005$ for (a) $Br = 0.8$, and (b) $Br = 50$

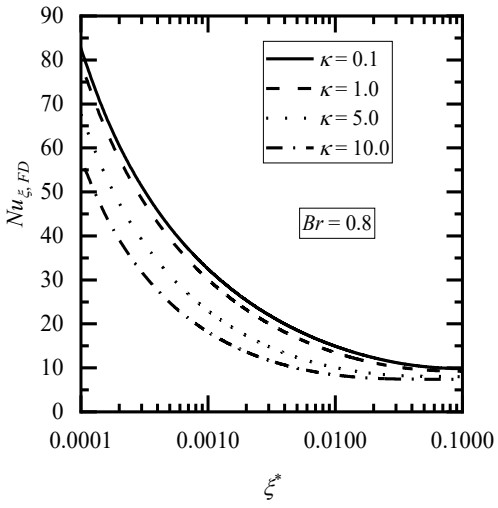

(a)

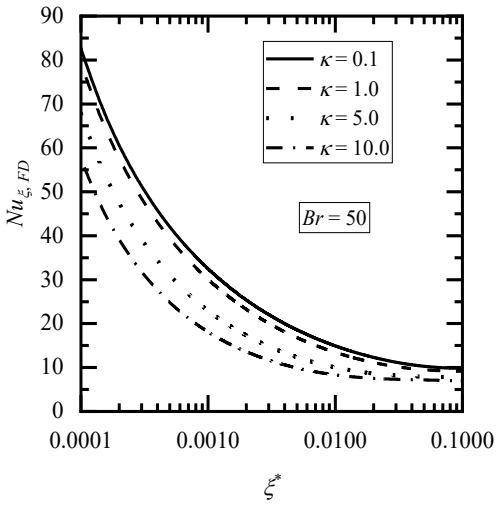

(b)

Fig. 4.11: Variation in $Nu_{\xi,\,CFC}$ with ξ^* for distinct values of κ at $Bi = 10$ and $Da = 0.005$ for (a) $Br = 0.8$, and (b) $Br = 50$

The effect of ratio, κ (for the CFC model) on $Nu_{\xi,\,CFC}$ is shown in Fig. 4.10(a ,b) for distinct values of κ at $Da = 0.005$, and $Bi = 10$ for (a) $Br = 0.8$, and (b) $Br = 50$. A similar type of plot is given for the FD model in Fig. 4.11(a, b). From the plots with respect to κ $\left(= k_{pe} / k_{fe}\right)$, it has been a significant variation in the local Nusselt number. It is clear that as the ratio κ increases (from κ = 0.1 to 10), $Nu_{\xi,\,CFC}$ and $Nu_{\xi,\,FD}$ decrease for each value of *Da*, *Br*, and *Bi*. Reducing the thermal conductivity ratio improves convective heat transmission, governed by the fluid phase. Without a viscous dissipation model, this variation (κ variation) can be seen in Nield et al. [34] for

constant wall temperature boundary conditions. The Nusselt number for the porous-filled duct decreases because it is correlated with the convective heat transfer of the fluid phase. It is noted that at low values of the ratio κ, $Nu_{\xi,\,CFC} > Nu_{\xi,\,FD}$. Hence, the local Nusselt number in the CFC model is substantial, in contrast to the outcome in the FD model. Consequently, the enhanced convectional heat transfer of the CFC model is superior.

Comparison and validation

For the CFC model, a comparison of values of $Nu_{\xi,\,CFC}$ with the literature (Bhargavi and Reddy [75]) is given in Table 4.3 for the LTE model when $Br = 0$ for large Bi. The agreement is good. It is observed that for large Bi (> 335), LTNE tend to LTE. Hence, a comparison is made with the LTE model.

Table 4.3: Comparison of the present work with Bhargavi and Reddy's literature [75] under LTE with $Br = 0$ and large Bi at $\kappa = 1$

Da	$Nu_{\xi,\,CFC}$	
	Bhargavi and Reddy [75]	Present study (At large Bi)
0.001	168.7189	168.7015
0.005	139.0343	139.0308
0.010	127.6779	127.6610
0.050	109.2753	109.2075
0.100	105.2097	105.2033

4.6 Conclusions

Forced convection at the entry region of a porous material-filled channel under LTNE has been numerically examined, including viscous dissipation. The fundamental goal of this study is to determine which of the two viscous dissipation models, the CFC model or the FD model, is appropriate, as well as the validity of the LTNE assumption. The primary findings of the study are as follows:

i. The effect of the Brinkman number, *Br,* can be seen in the temperature profiles for both dissipation models (CFC and FD models).

ii. For each value of *Da*, *Bi*, *Br* and, κ the temperature in both phases rises as ξ^* rises. The increase in *Br* and ratio κ, enhances the temperature distribution. For a large *Bi*, LTNE tends to LTE for each value of *Br* in both dissipation models. However, it is observed that $\varphi_p > \varphi_f$, which validates LTNE effect. It is valid for both models (FD and CFC models).

iii. In CFC and FD models, temperatures in the CFC model are more than the temperatures in the FD model for each value of ξ^* and variable parameters.

iv. Whenever $\left|\varphi_p - \varphi_f\right| \geq 0.13$ at any computing grid in the channel domain, including the developing region, the LTNE condition is claimed.

v. The local Nusselt number strongly depends on the values of parameters *Da*, *Br*, *Bi*, and κ. $Nu_{\xi,\,CFC}$ and $Nu_{\xi,\,FD}$ decrease with an increase of parameters *Br*, *Da*, *Bi*, and ratio κ. The effect of these parameters is much less in the FD model than in the CFC model.

vi. In contrast to the result in the FD model, a significant value of the local Nusselt number is obtained in the CFC model. As a result, the CFC model has excellent increased convectional heat transmission.

Chapter 5

Forced Convection Heat Transfer at the Entry Region of the Porous Channel under LTNE with Axial Conduction and Viscous Dissipation

5.1 Introduction

When analyzing forced convection heat transfer in a fluid, it's essential to consider the combined effects of axial conduction and viscous dissipation, especially in situations where these effects are significant. Axial conduction refers to heat transfer along the direction of fluid flow, while viscous dissipation occurs due to the conversion of kinetic energy into thermal energy within the fluid. This paper examines the combined impact of axial conduction and the clear fluid compatible (CFC) viscous dissipation model used at the thermal entry. The thermal properties of fluid flowing through a porous substance submerged in a channel formed by parallel plates have been examined. LTNE is used to examine it numerically. The boundary condition with constant wall heat flux is applied to channel walls. The Darcy Brinkman model porous area is said to control flow, which is seen as unidirectional. Numerical solutions have been obtained for the thermal field.

5.2 Mathematical Model

The parallel plate channel's schematic model and coordinate system are shown (Chapter 3, § Fig. 3.1). The thermal field includes axial conduction and viscous dissipation. Porous and fluid regions are in LTNE. The porous medium is isotropic and homogeneous. Heat generation is negligible. The thermophysical properties are constant. The normalized velocity expression is taken from Chapter 3, § Eq. (3.32) for $M = 0$, to solve the coupled thermal energy equations.

Governing Equations

The steady-state conservation of thermal energy equations of the fluid and porous phases are given by:

Fluid phase

$$\left(\rho C_p\right)\left(u\frac{\partial T_f}{\partial x^*}\right)=k_{fe}\left(\frac{\partial^2 T_f}{\partial x^{*2}}+\frac{\partial^2 T_f}{\partial y^{*2}}\right)+a_{pf}h_{pf}\left(T_p-T_f\right)+\left[\frac{\mu}{K}u^2+\mu_e\left(\frac{du}{dy^*}\right)^2\right] \tag{5.1}$$

Porous phase

$$k_{pe}\left(\frac{\partial^2 T_p}{\partial x^{*2}}+\frac{\partial^2 T_p}{\partial y^{*2}}\right)-a_{pf}h_{pf}\left(T_p-T_f\right)=0 \tag{5.2}$$

In Eq. (5.1), the dissipation function is considered for a clear fluid compatible (CFC model) with the study by Al-Hadhrami et al. [139].

The boundary conditions for the governing equations and the dimensionless variables are the same as in Chapter 3, § Eqs. (3.5) to (3.8) and Eq. (3.10).

The governing equations (Eqs. (5.1) and (5.2)) in dimensionless form become after applying the dimensionless variables (Chapter 3, § Eq. (3.10)).

$$k_1U^N\left(\eta\right)\frac{\partial\varphi_f}{\partial\xi^*}=A_c\frac{1}{Pe^2}\frac{\partial^2\varphi_f}{\partial\xi^{*2}}+\frac{\partial^2\theta_f}{\partial\eta^2}+Bi\ \kappa\left(\varphi_p-\varphi_f\right)+Br\left[\left(U^N\right)^2+\frac{Da}{\varepsilon}\left(\frac{dU^N}{d\eta}\right)^2\right] \tag{5.3}$$

$$A_c\frac{1}{Pe^2}\frac{\partial^2\varphi_p}{\partial\xi^{*2}}+\frac{\partial^2\varphi_p}{\partial\eta^2}-Bi\left(\varphi_p-\varphi_f\right)=0 \tag{5.4}$$

In Eqs. (5.3) and (5.4), the presence or absence of the axial conduction term depends on the value of A_c. Specifically, when $A_c = 0$, the axial conduction term is omitted, whereas when $A_c = 1$, the axial conduction term is included. Furthermore, in the case where $A_c = 0$, the solutions to Eqs. (5.3) and (5.4) with respect to the thermal field are

independent of *Pe* in terms of the dependence on ξ^*. $U^N(\eta)$ is normalized velocity given in Chapter 3, § Eqs. (3.32) is used to solve the coupled system of equations (Eqs. (5.3) and (5.4)) by taking the Hartmann number (*M* = 0).

In Eqs. (5.3) and (5.4), the definitions of the parameters, *Da, Pe, Br, Bi,* κ, ε, and k_1 are given in Chapter 4, § Eqs. (4.10) to (4.15).

5.3 Local Nusselt Number

The local heat transfer coefficient (h_ξ) is determined at the wall $y^* = H/2$ adjacent to the porous medium as follows:

$$-k_{fe}\left.\frac{\partial T_f}{\partial y^*}\right|_{y^*=\frac{H}{2}} = h_\xi\left(T_w - T_b\right) \tag{5.5}$$

In Eq. (5.5) , the bulk mean temperature (T_b) is denoted as follows:

$$T_b = \frac{\int_{-H/2}^{H/2} uT_f dy^*}{\int_{-H/2}^{H/2} u dy^*} \tag{5.6}$$

Using dimensionless variables, the local Nusselt number at $\eta = 1/2$, Nu_ξ is given by:

$$Nu_\xi = \frac{h_\xi(2H)k_1}{k_f} = \frac{-2\left(\left.\frac{\partial \varphi_f}{\partial \eta}\right)\right|_{\eta=\frac{1}{2}}}{\left(\varphi_w - \varphi^*\right)} = \frac{2}{\left(\varphi^* - \varphi_w\right)} \tag{5.7}$$

In Eq. (5.7), φ_w and φ^* are defined in Chapter 2, § Eqs. (2.33) and (2.34) and φ^* is evaluated by Eq. (2.35) (Chapter 2).

5.4 Numerical Methodology

Numerical solutions to Eqs. (5.3) and (5.4) with the boundary conditions on φ, as specified in Chapter 3, § Eqs. (3.25) to (3.27), have been computed using the successive accelerated replacement (SAR) scheme.

5.5 Numerical Results and Discussions

Numerical solutions have been obtained for the conservation of the thermal energy two-equation model (LTNE model) in a channel filled with a porous medium. It is assumed that $k_1 = k_f / k_{fe} = 1$, $k_2 = k_f / k_{pe} = 1$, and $\varepsilon = \mu / \mu_{eff} = 1$. $0.001 \le Da \le 0.1$, $10 \le Bi \le 100$, $0.8 \le Br \le 100$, $5 \le Pe \le 100$, and $0.1 \le \kappa \le 10$ are the ranges used for parameters.

5.5.1 Thermal Field

In this section, we explore the influence of axial conduction and viscous dissipation within the thermally developing region. The dimensionless temperature profiles, dimensionless temperature based on the bulk mean temperature and the local Nusselt number for flow through the porous-filled channel are examined in the present section.

The dimensionless temperature in the fluid phase and porous phase:

To analyze how the Peclet number (*Pe*), Brinkman number (*Br*), Biot number (*Bi*), and thermal conductivity ratio (κ) affect thermal development in different regions, we present graphical representations of dimensionless temperature profiles in both the porous and fluid phases. These plots cover various values of normalized dimensionless axial distance, $\xi^* \left(= x^* / (Pe) H\right)$. From these plots, it is observed that the wall temperatures, $\varphi_{wf}\big|_{\eta=+1/2} = \varphi_{wf}\big|_{\eta=-1/2}$ and $\varphi_{wp}\big|_{\eta=+1/2} = \varphi_{wp}\big|_{\eta=-1/2}$, which demonstrate the channel's symmetry and symmetric profiles of dimensionless temperature in the fluid phase, φ_f and in the porous phase, φ_p can be seen about $\eta = 0$. Additionally, φ_f and φ_p have a minimum value at the centre of the channel (at $\eta = 0$) and attains maximum value at the walls.

From Figs. 5.1 to 5.5, plots are given for $Da = 0.001$ and at various values of ξ^* at small and large values of parameters Pe, Bi, Br, and κ ($Pe = 5, 100$, $Bi = 10, 100$, $Br = 0.8, 20$, and $\kappa = 0.1, 10$). Under the LTNE model, the normalized axial distance, ξ^* affects the temperature profile. As ξ^* increases (moving downstream), the fluid temperature φ_f gradually increases due to heat absorption from the porous phase φ_p and approaches thermal equilibrium. Furthermore, even though φ_f is still lower than φ_p ($\varphi_p > \varphi_f$), it is increasing as it reaches equilibrium with the surface. The comparison of Figs. 5.1(a) and 5.1(b) demonstrates this.

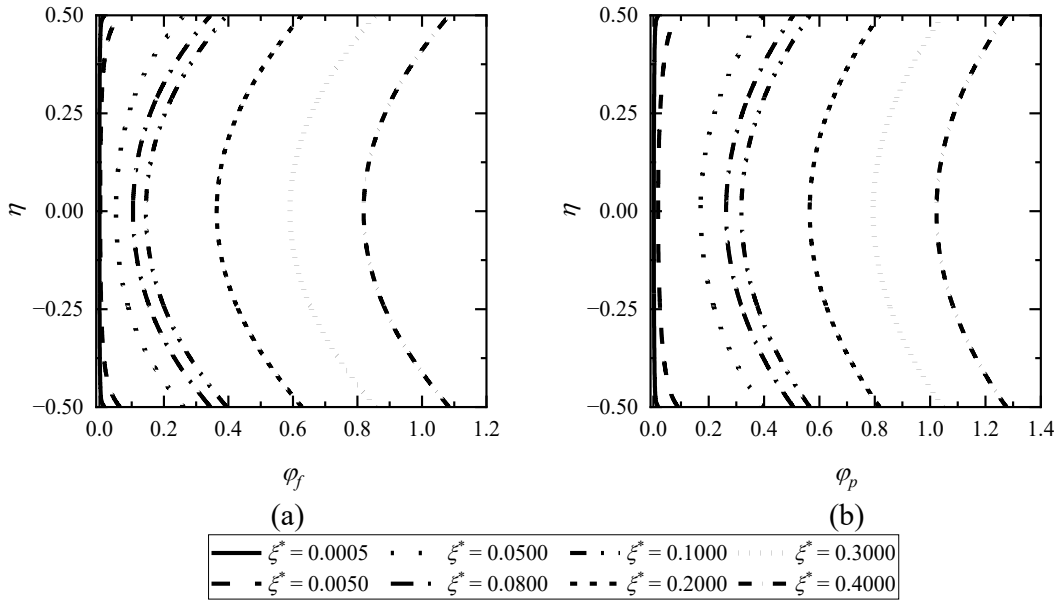

Fig. 5.1: Impact of (a) φ_f and (b) φ_p for distinct ξ^* values for $Bi = 10$, $Br = 0.8$, $Pe = 5$, and $\kappa = 0.1$ at $Da = 0.001$

Under the LTNE model, axial conduction significantly affects temperature distribution. In Fig. 5.1(a, b), plots are given for a low value of Peclet number, $Pe = 5$ at a given value of parameters, $Bi = 10$, $Br = 0.8$, $\kappa = 0.1$, and $Da = 0.001$. A similar type of plot is given for a large value of Pe, $Pe = 100$ in Fig. 5.2(a, b). Axial conduction refers to heat transfer occurring along the direction of fluid flow within the porous phase itself. Hence, this phenomenon becomes particularly important when Pe is relatively high, indicating that convective heat transfer dominates, and the fluid temperature evolves separately from the porous temperature due to finite thermal resistance between

them. Mathematically, from Eqs. (5.3) and (5.4), at $Br = 0$ and for large Pe, $Pe \to \infty$ (i.e. $A_c = 0$, axial conduction is absent).

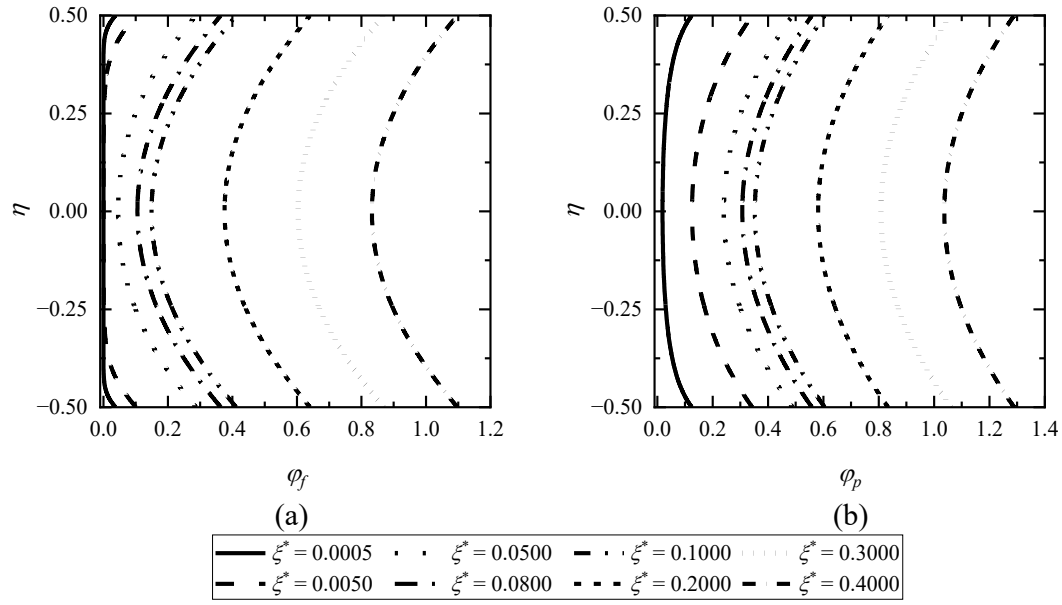

Fig. 5.2: Impact of (a) φ_f and (b) φ_p for distinct ξ^* values for $Bi = 10$, $Br = 0.8$, $Pe = 100$, and $\kappa = 0.1$ at $Da = 0.001$

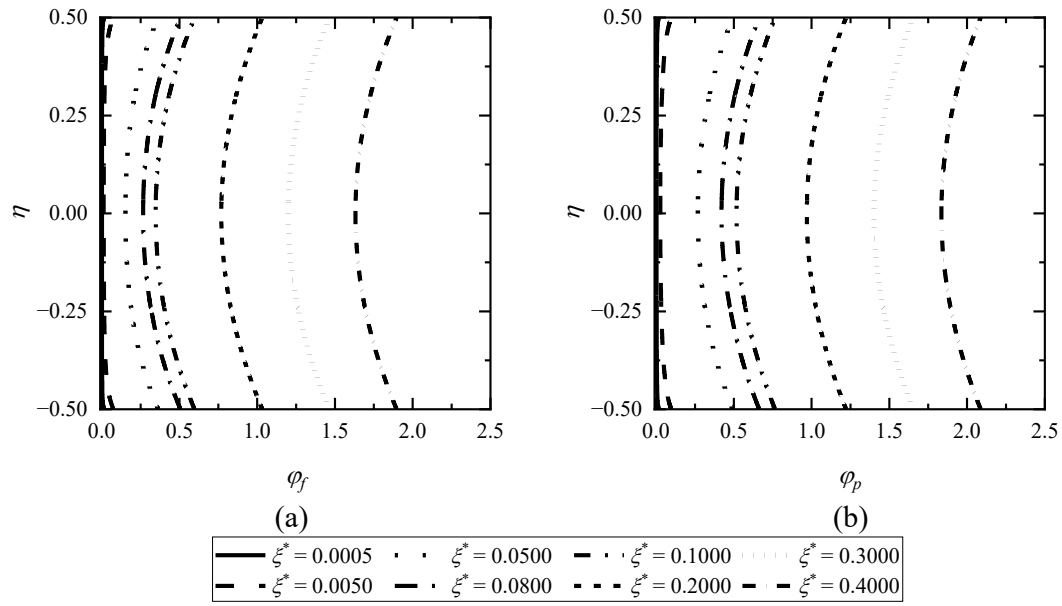

Fig. 5.3: Impact of (a) φ_f and (b) φ_p for distinct ξ^* values for $Bi = 10$, $Br = 20$, $Pe = 5$, and $\kappa = 0.1$ at $Da = 0.001$

A plot is given in Fig. 5.3(a, b) for an immense value of Br ($Br = 20$) at a given value of various parameters to analyse the effect of the Brinkman number, Br,. By

comparing Fig. 5.1(a, b) and Fig. 5.3(a, b), for each ξ^* value, as *Br* increases from *Br* = 0.8 to 20, φ_f and φ_p increase, this is because the two-phase interaction behaves as a heat source in the porous medium. At a significant value of *Br*, the temperature rise will be higher, and the heat conduction will be slower.

A large value of *Br* implies that viscous dissipation in the fluid dominates heat conduction within the porous matrix. The fluid phase may exhibit a significant temperature gradient due to viscous heating effects. Hence, it can also be seen from the figures that the porous phase, influenced by heat conduction, might have a more uniform temperature distribution than the fluid. In this model, it is observed that $\varphi_p > \varphi_f$ which indicates the presence of LTNE model effect when channel walls are subjected to constant wall heat flux.

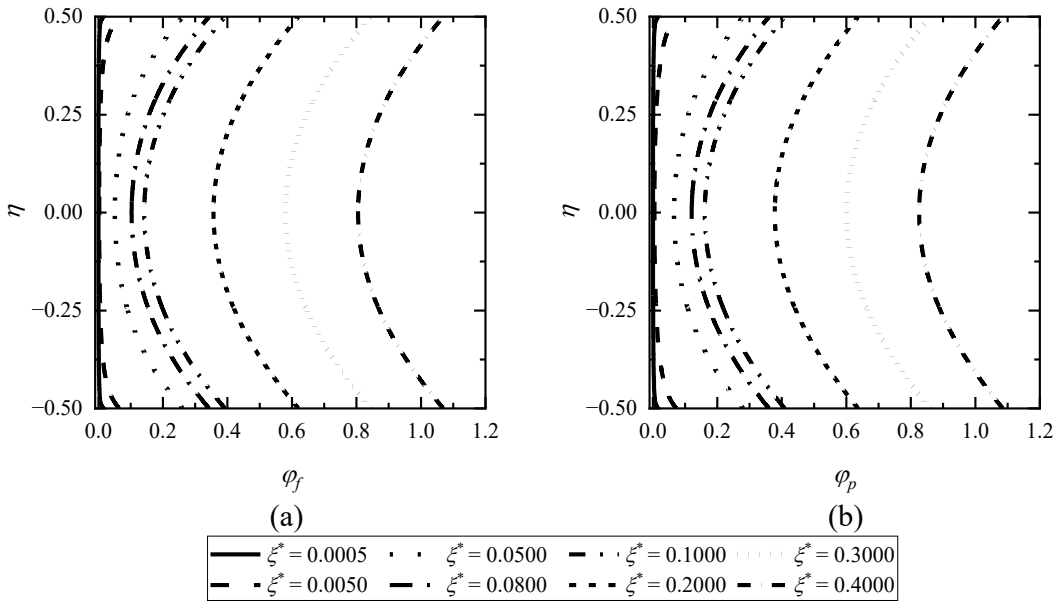

Fig. 5.4: Impact of (a) φ_f and (b) φ_p for distinct ξ^* values for *Bi* = 100, *Br* = 0.8, *Pe* = 5, and κ = 0.1 at *Da* = 0.001

The Biot number, *Bi,* influences the temperature distribution in the fluid and porous phases under the LTNE model. For the large value of *Bi*, *Bi* = 100, the plot is given in Fig. 5.4. By comparing Fig. 5.1 with Fig. 5.4, as *Bi* increases, φ_p decreases for all values of ξ^*, *Da*, and κ. It is because a higher Biot number implies a larger external

thermal resistance, hindering heat transfer from the fluid to the porous phase. As a result, the porous phase temperature decreases.

A significant value of *Bi* implies that the heat transfer rate inside the porous medium is much faster than the heat transfer rate between the porous and the surrounding fluid. In this situation, the porous phase will approach thermal equilibrium relatively quickly, and its temperature distribution will be nearly uniform. It means that for the significant value of *Bi*, LTNE tends to LTE. This fact is also discussed in Chapters 2, 3, and 4. The increased Biot number indicates a more intense internal heat exchange between the porous and fluid phases of the porous material, which reduces the temperature difference between the two phases (i.e., the LTE condition). Mathematically as $Bi \to \infty$, $\varphi_p \to \varphi_f$ (i.e., LTNE tends to LTE), from Eqs. (5.3) and (5.4). For a large value of *Pe* ($A_c = 0$) and in the absence of the dissipation term (*Br*) in the fluid phase energy equation, this phenomenon also holds in tubes with constant wall temperature boundary conditions, as stated in Khashan et al. [35].

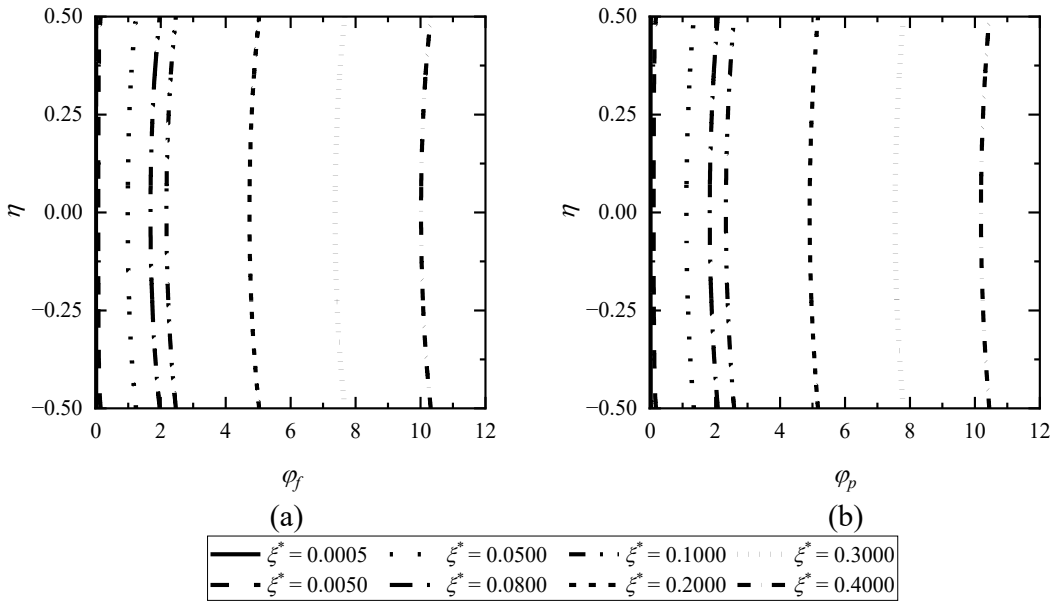

Fig. 5.5: Impact of (a) φ_f and (b) φ_p for distinct ξ^* values for *Bi* = 10, *Br* = 0.8, *Pe* = 5, and κ = 10 at *Da* = 0.001

To access the effect of ratio, κ, on φ_f and φ_p, the plot is given for a large value of κ, (κ = 10.0) for *Da* = 0.001, *Bi* = 10, *Pe* = 5, and *Br* = 0.8 for various ξ^* values in Fig. 5.5(a, b). By comparing Fig. 5.5 with Fig. 5.1 (low value of κ), as κ increases, φ_f and φ_p increase for all values of ξ^*. At a given value of *Bi* and *Pe*, κ>1 indicates that the porous phase has a much higher thermal conductivity than the fluid phase $\left(k_{pe} > k_{fe}\right)$, which can lead to an increase in both φ_f and φ_p. In this scenario, heat conduction within the porous dominates the heat transfer process, and the porous phase tends to have a relatively uniform temperature distribution with higher temperatures. However, the fluid phase, influenced by convective heat transfer (*Pe*) and heat transfer from the porous, can also have higher temperatures near the porous-fluid interface.

Dimensionless temperature based on bulk mean temperature in the fluid phase and porous phase:

To confirm the attainment of fully developed conditions in a porous-filled channel under LTNE, Fig. 5.6 illustrates the dimensionless temperature, which is based on the bulk mean temperature (φ_b), for the case with *Da* = 0.001, *Bi* = 10, and κ = 0.1 for (a) *Pe* = 5, and (b) *Pe* = 50 at *Br* = 0.2. A similar type of plot is given for *Br* = 10 at *Pe* = 5 in Fig. 5.7. Form the Figs. 5.6 and 5.7, it is clear that φ_b tends to zero for large $\xi^* \geq$ 0.35 for any *Pe*, *Br*, *Bi*, κ, and *Da*. It implies that φ_b remains constant with respect to ξ^* when ξ^* is sufficiently large, signifying a state of fully developed conditions. It is also true under LTNE circumstances without viscous dissipation and axial conduction. A similar validation (particularly for LTE) is shown in the work of Repaka and Satyamurty [73]. This result is also discussed in Chapters 2 and 3.

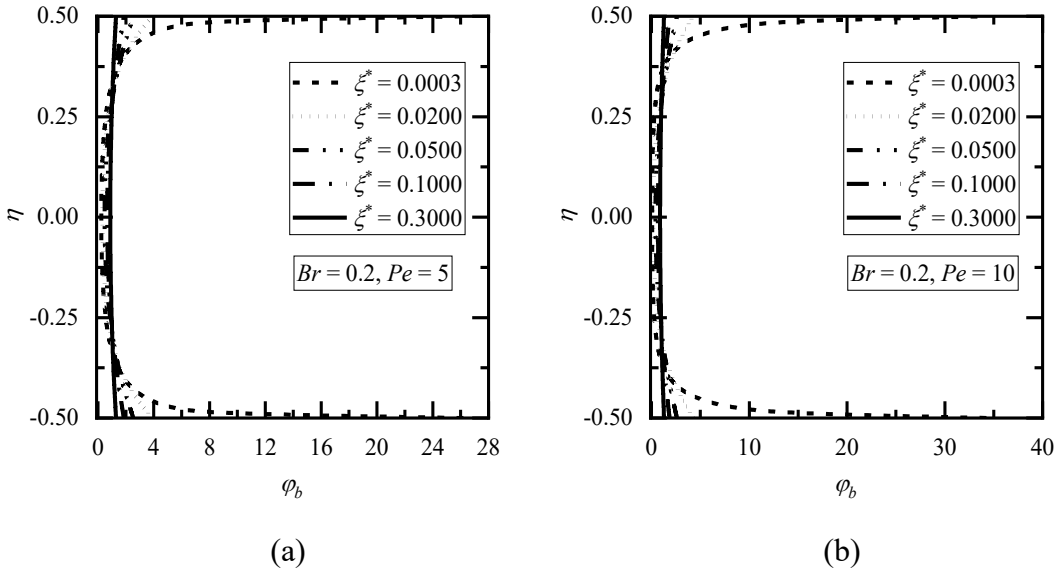

(a) (b)

Fig. 5.6: φ_b effect for distinct ξ^* values for (a) Pe = 5, and (b) Pe = 10 at Br = 0.2, Bi = 10, Da = 0.001, κ = 0.1

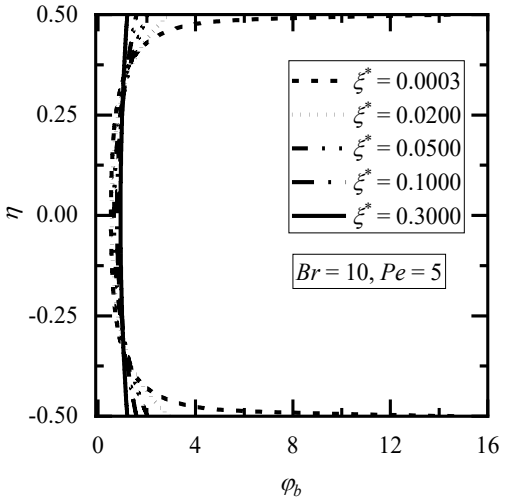

Fig. 5.7: φ_b effect for distinct ξ^* values at Pe = 5, Br = 10, Bi = 10, Da = 0.001, κ = 0.1

Local Nusselt number

In the context of local Nusselt number (Nu_ξ) profiles under the LTNE model, the dimensionless axial distance and dimensionless normalized axial distance, often denoted as ξ^* and ξ, represent the spatial coordinate along the porous medium in a dimensionless form. In this section, the discussion is given for Nu_ξ with respect to ξ^* for distinct values of various parameters, Pe, Br, Bi, Da, and κ. The plots which are

given in Figs. 5.8(a), 5.9(a) and Figs 5.10(a, b) and 5.11(a, b) show that raising ξ^* results in a drop in Nu_ξ. This is because as the fluid moves downstream in the channel, Nu_ξ decreases until it reaches a constant value. The same pattern can be seen with respect to ξ (Figs. 5.8(b) and 5.9(b)).

Effects of axial conduction on Nu_ξ profiles with respect to ξ^* (normalized dimensionless axial distance), and ξ (dimensionless axial distance) are given in Figs. 5.8(a, b) and Fig. 5.9(a, b) for various values of Peclet number, *Pe* (*Pe* = 5, 10, 25, 50, and 100) at *Br* = 0.8, κ = 0.1, *Bi* = 10 for *Da* = 0.005 and *Da* = 0.05, respectively. From Figs. 5.8(a, b) and 5.9(a, b), Nu_ξ increases as *Pe* decreases at fixed ξ^*, whereas, Nu_ξ increases as *Pe* decreases at a fixed ξ $\left(\xi^* \times Pe\right)$. This feature is also true for the LTE model for ducts, fully and partially filled with porous material and for clear fluid channels. Additionally, by comparing Figs. 5.8 and 5.9, one can see the effect of *Da*. As *Da* increases (*Da* = 0.005 to 0.05), Nu_ξ decreases for each value of ξ^* and ξ.

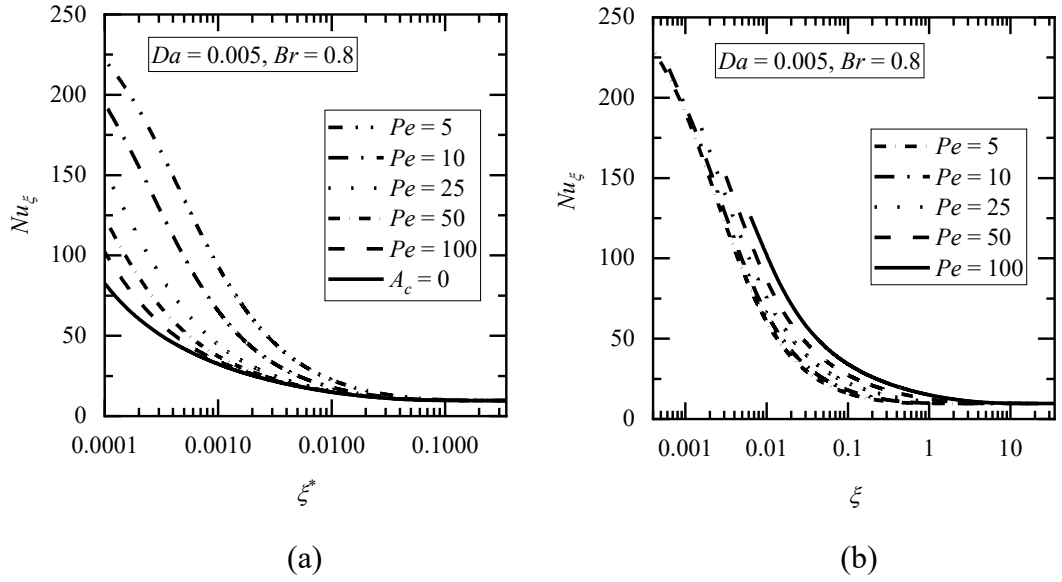

Fig. 5.8: Effect of local Nusselt numbers (Nu_ξ) with (a) ξ^* (normalized dimensionless axial distance), and with (b) ξ (dimensionless axial distance) for various values of *Pe* for κ = 0.1, *Bi* = 10, and *Da* = 0.005

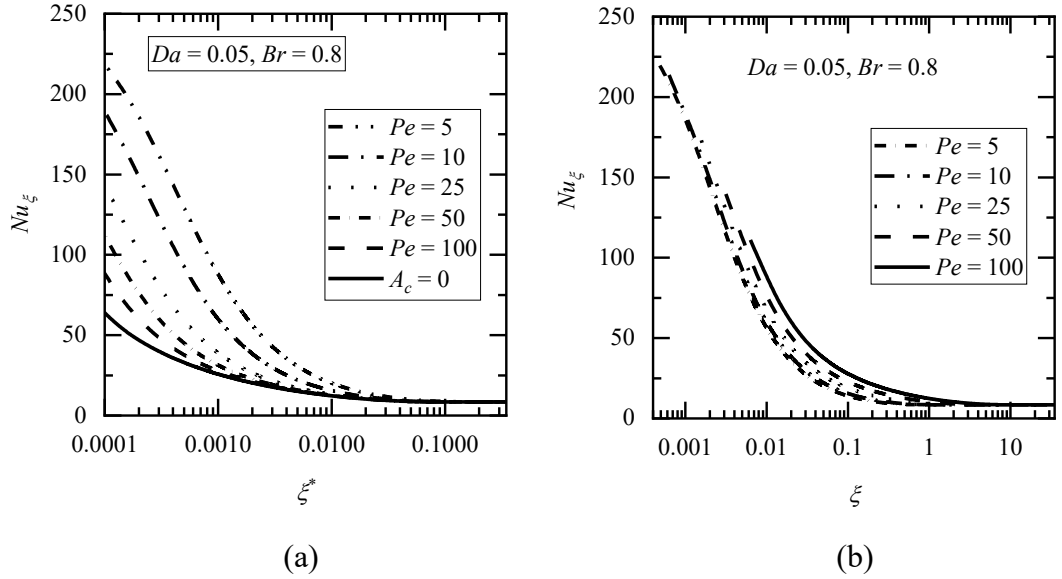

Fig. 5.9: Effect of local Nusselt numbers (Nu_ξ) with (a) ξ^* (normalized dimensionless axial distance), and with (b) ξ (dimensionless axial distance) for various values of *Pe* for κ = 0.1, *Bi* = 10, and *Da* = 0.05

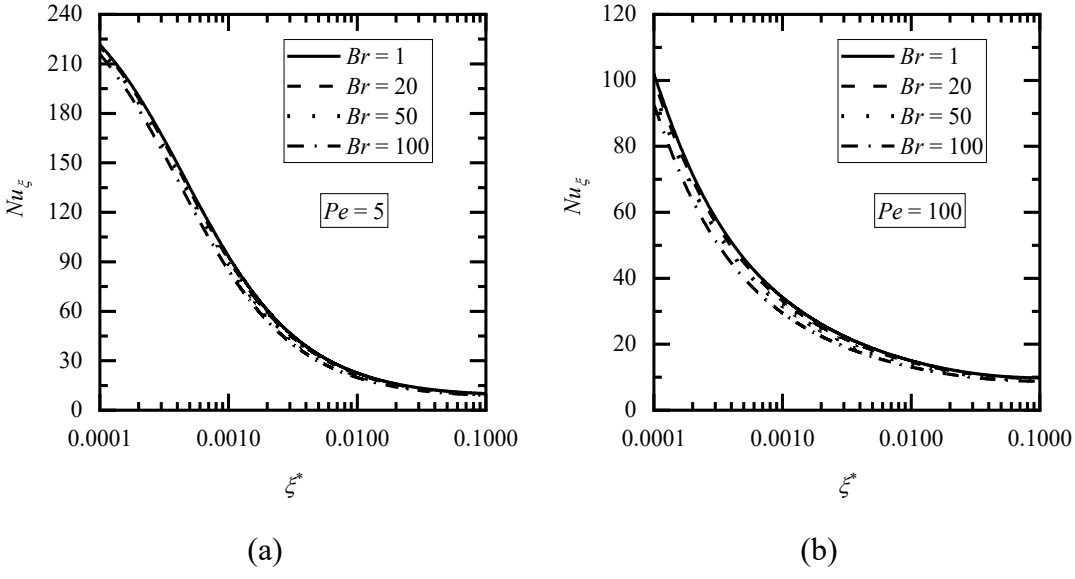

Fig. 5.10: Change in Nu_ξ with ξ^* for distinct values of *Br* at κ = 0.1, *Da* = 0.005, and *Bi* = 10 for (a) *Pe* = 5, and (b) *Pe* = 100

The effect of the Brinkman number, *Br*, on Nu_ξ profiles is given in Fig. 5.10 for (a) *Pe* = 5 and (b) *Pe* = 100. From the plot, as *Br* increases, it decreases and tends to shorten the thermal entry length due to low thermal diffusion via the fluid phase in the porous media. This observation holds for channels containing a partial porous medium filling, as established in the LTNE model by Baig et al. [144]. Similarly, this

finding remains consistent within the LTE model, as discussed by Arici and Aydin [162]. It's worth noting that this phenomenon is initially identified under conditions of constant wall temperature, as stated independently by Nield et al. [34].

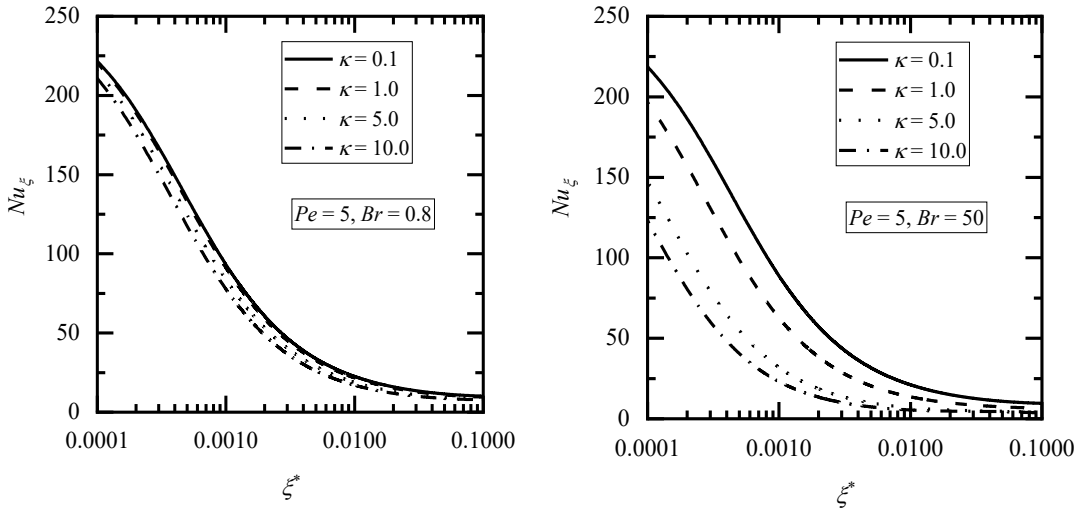

Fig. 5.11: Change in Nu_ξ with ξ^* for distinct values of κ at Pe = 5, Da = 0.005, and Bi = 10 for (a) Br = 0.8, and (b) Br = 50

The effect of the thermal conductivity ratio, κ on Nu_ξ is shown in Figs. 5.11 for (a) Br = 0.8, and (b) Br = 50 at distinct values of κ (κ = 0.1, 1.0, 5.0, 10.0) at Pe = 5, Da = 0.005, and Bi = 10. A similar type of plot is given for a large value of Pe, Pe = 100, in Fig. 5.12. From the plots, it can be seen that with respect to κ ($=k_{pe}/k_{fe}$), there has been a significant variation in Nu_ξ. It is clear that as the ratio κ, increases (from κ = 0.1 to 10), Nu_ξ decreases for each value of Da, Pe, Br, and Bi. This observation remains consistent in the context of channels partially filled with porous media, as modelled by Baig et al. [144]. The fluid phase plays a significant role in heat transmission. In other words, reducing the thermal conductivity ratio improves convective heat transmission, which is governed by the fluid phase. Without an axial conduction and viscous dissipation model, this variation (κ variation) can also be seen in Nield et al. [35] for constant wall temperature boundary conditions. The Nusselt number decreases in the case of the porous-filled duct since it is associated with convective heat transfer of the fluid phase. By comparing Figs. 5.11(a, b) and 5.12(a,

b), one can see the effect of *Pe* on Nu_ξ for various values of ratio, κ. As *Pe* increases, Nu_ξ decreases with respect to ξ^* (normalized dimensionless axial distance). It can also be represented in Figs. 5.8(a) and 5.9(a).

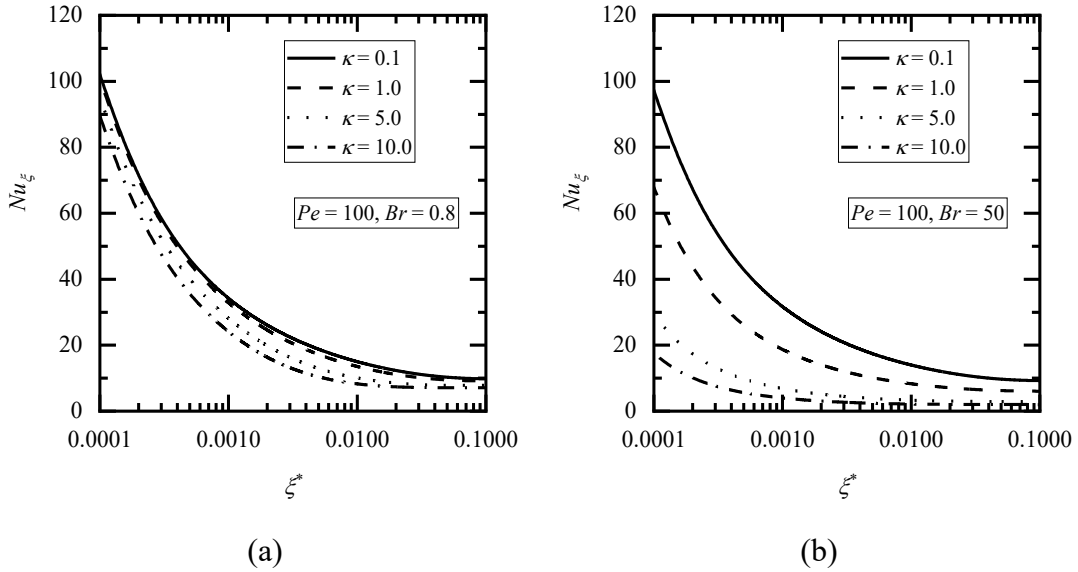

(a) (b)

Fig. 5.12: Change in Nu_ξ with ξ^* for distinct values of κ at *Pe* = 100, *Da* = 0.005, and *Bi* = 10 for (a) *Br* = 0.8, and (b) *Br* = 50

Table 5.1: Effect of *Bi* on Nu_ξ at *Br* = 0.8, *Da* = 0.005, and κ = 0.1

Nu_ξ				
	Pe = 5		*Pe* = 100	
ξ^*	*Bi* = 10	*Bi* = 100	*Bi* = 10	*Bi* = 100
0.0001	214.0329	214.0315	90.1557	89.8964
0.0010	92.5458	92.5446	34.0230	33.6872
0.0100	22.4736	22.4710	14.9736	14.7966
0.1000	10.1321	10.1141	9.7941	9.6267

5.6 Conclusions

Axial conduction and viscous dissipation have been quantitatively investigated in forced convection at the entrance area of a porous material-filled channel under LTNE. Numerical solutions for the thermal field have been devised. The LTNE area was mapped over a wide range of dimensionless characteristics due to the study's parametric

methodology. Examining the combined impact of axial conduction and viscous dissipation under LTNE is the main objective of this study. This model takes into account the CFC model for viscous dissipation.

The primary findings of the study are as follows:

i. The temperature rises with increasing values of the Peclet number (*Pe*), Brinkman number (*Br*), and thermal conductivity ratio (κ).

ii. In the presence of axial conduction and viscous dissipation, for large Biot number (*Bi*), LTNE tends to the LTE model. However, it is observed that $\varphi_p > \varphi_f$, which validates the LTNE effect.

iii. Validation of fully developed conditions for the thermal filed is done with Peclet number, *Pe* and Brinkman number, *Br*.

iv. Local Nusselt number, Nu_ξ depends on the values of the parameters, *Da*, *Pe*, *Br*, *Bi*, and κ. In the presence of Brinkman number (*Br*), the impact of axial conduction becomes negligible, i.e., $A_c = 0$, when the Peclet number (*Pe*) is sufficiently large (≥ 100) in the LTNE framework.

v. The local Nusselt number, Nu_ξ with ξ^* (normalized dimensionless axial distance), decreases as the Peclet number, Brinkman number, and thermal conductivities increase. However, as *Pe* increases, Nu_ξ increases with ξ (dimensionless axial distance, and this is because of the increase in the convective heat transfer rate.

Chapter 6
Summary, Conclusions and Scope for Future Work

Heat transfer is the mechanism for exchanging thermal energy between distinct zones within or among different systems. In heat transport through porous media, including a fluid phase and a porous matrix, modelling approaches can be based on either thermal equilibrium or thermal non-equilibrium assumptions. Consequently, two distinct modelling strategies have been employed: the LTE and the LTNE models in porous medium.

The LTNE model analyses heat transfer in systems where various components or regions undergo diverse thermal conditions. Unlike the assumption of thermal equilibrium, which implies a uniform temperature throughout a system, the LTNE model acknowledges that different parts may possess distinct temperatures and thermal states. This modelling approach finds applications in various fields where an accurate representation of heat transfer processes is crucial, particularly in scenarios where components or regions experience different thermal conditions. Examples include geological studies, thermal energy storage systems, electronics cooling, tissue heating and cooling, casting and solidification, microfluidics, and more.

These studies aim to provide hydrodynamic and thermal data for the laminar incompressible flow of a Newtonian fluid in channels containing porous material within the thermally developing region under the LTNE model. The research involves exploring the effects of axial conduction and viscous dissipation. The analysis establishes an improvement in heat transfer under LTNE, highlighting its correlation with axial position and various non-dimensional parameters such as the Darcy number, the Hatman number, the Biot number, the Peclet number, the Brinkman number, and the thermal conductivity ratio.

The illustration depicts the model and coordinate system of a parallel plate channel filled with a porous medium. The separation between the parallel plates is represented by H, and the fluid enters the channel at a uniform temperature. The channel walls are subject to a constant wall heat flux (q_w), and the fluid flow through the porous region is governed by the Darcy-Brinkman-Forchheimer model. A magnetic field (B_o) is applied perpendicular to the channel walls, and the flow is characterized by laminar, incompressible, steady, unidirectional flow and a developing thermal field. Both the porous and fluid regions are under the LTNE. The porous medium is uniform and possesses isotropic properties. The considerations encompass axial conduction and viscous dissipation, while the thermophysical properties remain constant throughout the system.

The subsequent summary outlines the findings and conclusions from the studies in Chapters 2 to 5. Specific essential points from Chapters 2 to 5 have been reiterated here for completeness.

Throughout this thesis, numerical solutions have been derived for the governing equations in Chapters 2 to 5 using the successive accelerated replacement (SAR) method, considering the following parameter values that characterize the various problems investigated. The ranges of the parameters Darcy number (Da), Forchheimer number (F), Hartmann number (M), Peclet number (Pe), Brinkman number (Br), Biot number (Bi), and thermal conductivity ratio (κ) are: $0.001 \le Da \le 0.1$, $1 \le F \le 100$, $0.5 \le M \le 65$, $5 \le Pe \le 100$, $0.8 \le Br \le 100$, $10 \le Bi \le 100$, and $0.1 \le \kappa \le 10$. Additionally, it is taken that $k_1 = k_f / k_{fe} = 1$, $k_2 = k_f / k_{se} = 1$ and, $\varepsilon = \mu / \mu_{eff} = 1$ for simplicity of the problem.

In Chapter 2, numerical investigations have been conducted for fluid flow and heat transfer within the thermally developing region of parallel plate channels filled with a porous material under the LTNE model. The parallel plates in this study are exposed to a constant wall heat flux. The conservation of the thermal energy equation excludes considerations of axial conduction and viscous dissipation effects. When

considered, the Biot number and thermal conductivity ratio offer a valuable framework for analyzing and comprehending the heat transfer within systems undergoing LTNE.

In the hydrodynamics case, the velocity profiles and skin friction coefficient for flow through a porous material-filled channel have been examined and are discussed in Chapter 2. The Forchheimer number exhibits a slight reduction in velocity as it increases, whereas an elevation in Hartmann's number corresponds to a decrease in velocity. Furthermore, an increase in the Darcy number (*Da*) results in a rise in velocity, reaching a notable magnitude where the velocity matches that in the fluid region. With an increase in the Forchheimer number (*F*), the product of skin friction coefficient and Reynolds number profiles (ReC_{fp}) experiences a rise at a constant Darcy number (*Da*). In the notable range of the Darcy number (significant value, $Da > 1.0$), ReC_{fp} approaches 6.0, a value characteristic of the fluid region. Similarly, at a given Darcy number, *Da*, ReC_{fp} increases as the Hartmann number, *M*, increases, and for the prominent *Da* (> 1.0), ReC_{fp} tends to 6.0. Apart from this, the effect of the Forchheimer number (*F*) on the temperature profiles is minimal in the thermal field. Also, as the Hartmann number increases, the temperature in the fluid phase (φ_f) and the porous phase (φ_p) decreases. However, as the Biot number (*Bi*) rises, the temperatures of the porous and fluid phases fall, approaching LTE for all Darcy numbers (*Da*) and Forchheimer numbers (*F*). It indicates that for large values of Biot number, LTNE leads to LTE. In the temperature profiles, the temperature in the porous phase is higher than in the fluid phase, which is evidence of the LTNE effect. A fully developed condition for the thermal field is validated for the LTNE model. Due to the imposition of consistent heat flux conditions on the walls, the temperatures of the walls will remain undisclosed. As the normalized axial distance, ξ^* rises, the wall temperature of the fluid and porous phases (φ_{wf} and φ_{wp}) progresses across all Biot numbers. Initially nonlinear, it transitions to a linear trend for $\xi^* > 0.005$, marking the initiation of a fully developed condition. A fully developed condition is evident even when applying the LTNE. It is the downstream boundary condition in axial conduction cases, particularly in elliptic partial differential equations. Moreover, $\varphi_{wp} > \varphi_{wf}$ because heat transmission from fluid to porous is greater at porous wall temperature than at fluid wall temperature. As the thermal conductivity ratio, κ and *Bi* grow, the local Nusselt number (Nu_ξ)

decreases. However, it increases with the increase of Hartmann's number. There is a low effect on Nu_{ξ} due to the Forchheimer number (F). Hence, as a result of the current research work, it is possible to deduce that small κ can improve heat transmission in the entry of the porous-filled channel. It is better to use LTNE conditions at the channel entrance.

In Chapter 3, the study examines the effect of axial conduction on the forced convective heat transfer characteristics in a channel filled with porous material that is thermally developing under LTNE. This Chapter aims to study the axial conduction effect under LTNE. The Darcy Brinkman model for the flow in porous media is employed since the Forchheimer number (F) minimally impacts the heat transfer coefficient.

Key findings of Chapter 3 are that an increase in the Hartmann number leads to a reduction in temperature for both the fluid and porous phases in the presence of axial conduction. Peclet number characterises the effect of axial conduction. The LTNE tends to converge towards LTE, mainly when dealing with high Biot numbers. Also, as the thermal conductivity ratio increases, temperature for both the fluid and porous phases increases for each value of normalised axial distance (ξ^*) and for a given value of Peclet number, Pe, Darcy number, Da, Hartmann number, M, and Biot number, Bi. Under LTNE, dimensionless temperature based on the bulk mean temperature in the fluid phase, $\varphi_{b,f}$ and for the porous phase $\varphi_{b,p}$ are invariant with respect to ξ^* for large ξ^*, which is an onset of the fully developed condition. Local Nusselt number Nu_{ξ} depends on the values of Pe, Bi, κ, and Da. The axial conduction effect is negligible, except near the entry, for a significant value of Peclet number, Pe ($\geq$ 100) in the LTNE. Local Nusselt number, Nu_{ξ} decreases as thermal conductivities and Biot numbers increase. In contrast, it increases with the increase of Hartmann's number. Nu_{ξ} decreases as ξ^* increases for all Da, Bi and κ and reaches the fully developed values for $\xi^* > 0.35$. However, a given ξ, Nu_{ξ} decreases as Peclet number, Pe decreases.

Chapter 4 discusses the impact of viscous dissipation on forced convective heat transfer properties within a porous material-filled channel undergoing thermal development under LTNE. The analysis utilizes the Darcy-Brinkman model to describe flow in porous media. The thermal energy conservation equation considers the viscous dissipation term, excluding the axial conduction term. The energy equation considers two viscous dissipation models: the clear fluid compatible (CFC) model and the form drag (FD) model. The investigation focuses on the effect of viscous dissipation on heat transfer enhancement. Brinkman number (*Br*) characterizes the viscous dissipation effect.

The critical findings of Chapter 4 are the effect of the Brinkman number, *Br,* on the temperatures and local Nusselt number for both the dissipation models, CFC and FD models. For each value of Darcy number (*Da*), Biot number (*Bi*), Brinkman number (*Br*) and thermal conductivity ratio (κ), the temperatures in both phases rise as normalized axial distance, ξ^* increases. The increase in *Br* and ratio, κ, enhances the temperature distribution for both models. For the large *Bi*, LTNE tends to LTE for each value of *Br* in both dissipation models. In CFC and FD models, temperatures are more than in the FD model for each value of ξ^* and for other parameters. The local Nusselt number strongly depends on the importance of parameters *Da*, *Br*, *Bi*, and κ for both models. The local Nusselt numbers of the CFC model and FD model ($Nu_{\xi,\,CFC}$ and $Nu_{\xi,\,FD}$) decrease with the increase of parameters *Br*, *Da*, *Bi*, and ratio, κ. The effect of these parameters is less in the FD model than in the CFC model. The CFC model has more increased convectional heat transmission than the FD model.

Chapter 5 discusses the effects of axial conduction and viscous dissipation on the forced convective heat transfer in a porous material-filled channel undergoing thermal development under LTNE. The study uses the Darcy-Brinkman model to represent flow in porous media. It has been shown in Chapter 4 that, as compared to the FD model, the CFC model has improved convectional heat transfer. As a result, the clear fluid compatible (CFC) model is employed as a viscous dissipation model in the energy equation.

The temperature increases by rising values of the Brinkman number (*Br*), thermal conductivity ratio (κ), and Peclet number (*Pe*). For a large Biot number (*Bi*), LTNE moves towards the LTE model in axial conduction and viscous dissipation terms. Local Nusselt number Nu_{ξ} depends on the values of the parameters, *Pe*, *Br*, *Bi*, κ, and *Da.* In the presence of Brinkman number (*Br*), the impact of axial conduction becomes negligible, i.e., $A_c = 0$, when the Peclet number (*Pe*) is sufficiently large (≥ 100) in the LTNE framework. The local Nusselt number decreases with normalized dimensionless axial distance as the Peclet number, Brinkman number, thermal conductivity ratio, and Biot number increase. On the other hand, the rise in the convective heat transfer rate increases with dimensionless axial distance as *Pe* increases.

Scope for Future Work

Future research endeavours aimed at expanding upon the current study may include the following inquiries:

i. When a process involving constant temperature, such as condensation or boiling, occurs, it is called the condition of constant wall temperature. Thus, under the LTNE model with a constant wall temperature boundary condition, research on laminar forced convection may be carried out inside the thermally growing area of parallel plate channels saturated with a porous material.

ii. Since there are many industrial applications of the LTNE model, with the constant wall temperature and constant heat flux boundary conditions, the same investigation may be undertaken with different geometries like cylinder channels, wavy-wall channels, lid-driven cavities, etc.

iii. For some of the more recent uses, research on flow and heat transfer via ducts partially filled with porous material is necessary, considering anisotropic and heterogeneous porous media.

iv. A bidisperse porous medium is a porous substance with two different particle sizes or components inside its structure. Permeability, porosity, and other transport characteristics of the porous medium can be impacted by its dispersity. Investigating the issue with the bidisperse porous medium is, therefore, necessary.

References

1. Shah, R.K., and London, A.L., 1980, “Laminar flow forced convection in ducts”, pp.256-257.

2. Kays, W. M., Crawford, M. E., and Weigand, B., 2012, “Convective Heat and Mass Transfer”, Fourth Edition.

3. Whitaker, S., 2013, “Fundamental principles of heat transfer”, Elsevier.

4. Nield, D. A., and Bejan, A., 2006, “Convection in porous media”, Vol. 3, pp. 629-982, Springer, New York.

5. Bejan, A., 2013, “Convection heat transfer”, John Wiley & Sons.

6. Kaviany, M., 2013, “Principles of convective heat transfer”, Springer.

7. Bejan, A., Kearney, D. W., and Kreith, F., 1981, “Second law analysis and synthesis of solar collector systems”.

8. Whitaker, S., 1986, “Local thermal equilibrium: an application to packed bed catalytic reactor design”, Chemical Engineering Science, 41(8), pp. 2029-2039.

9. Nayak, A. K., and Weigand, B., 2020, “Mixing and heat transfer in micro/nano-channel due to charged corrugated surfaces”, Applied Thermal Engineering, 170, p. 114979.

10. Wee, J. H., 2007, “Applications of proton exchange membrane fuel cell systems”, Renewable and Sustainable Energy Reviews, 11(8), pp. 1720-1738.

11. Griem, H. R., 1963, “Validity of local thermal equilibrium in plasma spectroscopy”, Physical Review, 131(3), p. 1170.

12. Von Backström, T. W., and Reuter, H. C., 2018, “Applicability of the local thermal equilibrium assumption in the performance modeling of CSP plant rock bed thermal energy storage systems”, Journal of Energy Storage, 15, pp. 39-56.

13. Sahoo, S. K., Das, M. K., and Rath, P., 2016, “Application of TCE-PCM based heat sinks for cooling of electronic components: A review”, Renewable and Sustainable Energy Reviews, 59, pp. 550-582.

14. Liang, S. Y., Lin, W. S., Chen, C. P., Liu, C. W., and Fan, C., 2021, “A review of geochemical modeling for the performance assessment of radioactive waste disposal in a subsurface system”, Applied sciences, 11(13), p. 5879.

15. Zhao, J., Jian, Q., and Huang, Z., 2020, “Experimental study on heat transfer performance of vapor chambers with potential applications in thermal management

of proton exchange membrane fuel cells", Applied Thermal Engineering, 180, p.115847.

16. Rout, K. R., Solsvik, J., Nayak, A. K., and Jakobsen, H. A., 2011, "A numerical study of multicomponent mass diffusion and convection in porous pellets for the sorption-enhanced steam methane reforming and desorption processes", Chemical engineering science, 66(18), pp. 4111-4126.

17. Hwang, J. J., 2005, "Thermal-electrochemical modeling of a proton exchange membrane fuel cell", Journal of the Electrochemical Society, 153(2), p. A216.

18. Ashwin, T. R., Narasimham, G. S. V. L., and Jacob, S., 2010, "CFD analysis of high frequency miniature pulse tube refrigerators for space applications with thermal non-equilibrium model", Applied Thermal Engineering, 30(2-3), pp. 152-166.

19. Kuznetsov, A. V., and Nield, D. A., 2010, "Effect of local thermal non-equilibrium on the onset of convection in a porous medium layer saturated by a nanofluid", Transport in Porous Media, 83, pp. 425-436.

20. Straughan, B., 2010, "Green–Naghdi fluid with non-thermal equilibrium effects", Proceedings of the Royal Society A: Mathematical, Physical and Engineering Sciences, 466(2119), pp. 2021-2032.

21. Damm, D. L., and Fedorov, A. G., 2006, "Local thermal non-equilibrium effects in porous electrodes of the hydrogen-fueled SOFC", Journal of Power Sources, 159(2), pp. 1153-1157.

22. Deléglise, M., Binétruy, C., Castaing, P., and Krawczak, P., 2007, "Use of non-local equilibrium theory to predict transient temperature during non-isothermal resin flow in a fibrous medium", International Journal of Heat and Mass Transfer, 50(11-12), pp. 2317-2324.

23. Hayes, A. M., Khan, J. A., Shaaban, A. H., and Spearing, I. G., 2008, "The thermal modelling of a matrix heat exchanger using a porous medium and the thermal non-equilibrium model", International Journal of Thermal Sciences, 47(10), pp. 1306-1315.

24. Kim, S., Kim, D., and Lee, D. Y., 2000, "On the local thermal equilibrium in microchannel heat sinks". International Journal of Heat and Mass Transfer, 43(10), pp. 1735-1748.

25. Lefebvre, L. P., Banhart, J., and Dunand, D. C., 2008, "Porous metals and metallic foams: current status and recent developments", Advanced engineering materials, 10(9), pp. 775-787.

26. Salas, K. I., and Waas, A. M., 2007, "Convective heat transfer in open-cell metal foams".

27. Ye, C., Li, B., and Sun, W., 2010, “Quasi-steady-state and steady-state models for heat and moisture transport in textile assemblies”, Proceedings of the Royal Society A: Mathematical, Physical and Engineering Sciences, 466(2122), pp. 2875-2896.

28. Straughan, B., 2015. Convection with local thermal non-equilibrium and microfluidic effects (Vol. 32). Springer.

29. Zhang, W., Yi, Y., Bai, X., and Nakayama, A., 2020, “A local thermal non-equilibrium analysis for convective and radiative heat transfer in gaseous transpiration cooling through a porous wall”, International Journal of Heat and Mass Transfer, 162, p. 120389.\

30. Vafai, K., 2015, “Handbook of porous media”, CRC Press.

31. Pati, S., Borah, A., Boruah, M. P., and Randive, P. R., 2022, “Critical review on local thermal equilibrium and local thermal non-equilibrium approaches for the analysis of forced convective flow through porous media”, International Communications in Heat and Mass Transfer, 132, p. 105889.

32. Amiri, A., and Vafai, K., 1994, “Analysis of dispersion effects and non-thermal equilibrium, non-Darcian, variable porosity incompressible flow through porous media”, International Journal of Heat and Mass Transfer, 37(6), pp. 939-954.

33. Bai, X., and Nakayama, A., 2019, “A local thermal non-equilibrium integral analysis for forced convective thermal boundary development in a channel filled with a fluid-saturated porous medium”, International Journal of Heat and Mass Transfer, 142, p. 118446.

34. Nield, D. A., Kuznetsov, A. V., and Xiong, M., 2002, “Effect of local thermal non-equilibrium on thermally developing forced convection in a porous medium”, International Journal of Heat and Mass Transfer, 45(25), pp. 4949-4955.

35. Khashan, S. A., Al-Amiri, A. M., and Al-Nimr, M. A., 2005, “Assessment of the local thermal non-equilibrium condition in developing forced convection flows through fluid-saturated porous tubes”, Applied Thermal Engineering, 25(10), pp. 1429-1445.

36. Dehghan, M., Valipour, M. S., Saedodin, S., and Mahmoudi, Y., 2016, “Thermally developing flow inside a porous-filled channel in the presence of internal heat generation under local thermal non-equilibrium condition: a perturbation analysis”, Applied Thermal Engineering, 98, pp. 827-834.

37. Yi, Y., Bai, X., Kuwahara, F., and Nakayama, A., 2021, “Analytical and numerical study on thermally developing forced convective flow in a channel filled with a highly porous medium under local thermal non-equilibrium”, Transport in Porous Media, 136, pp. 541-567.

38. Stanek, V., and Szekely, J., 1974, “Three-dimensional flow of fluids through nonuniform packed beds”, AIChE Journal, 20(5), pp. 974-980.

39. Catton, I., 1985, “Natural convection heat transfer in porous media”, Natural Convection: Fundamentals and Applications, pp. 514-547.

40. Givler, R. C., and Altobelli, S. A., 1994, “A determination of the effective viscosity for the Brinkman–Forchheimer flow model”, Journal of Fluid Mechanics, 258, pp. 355-370.

41. Nield, D. A., and Simmons, C. T., 2019, “A brief introduction to convection in porous media”, Transport in Porous Media, 130, pp. 237-250.

42. Banerjee, A., and Paul, D., 2021, “Developments and applications of porous medium combustion: A recent review”, Energy, 221, p. 119868.

43. Hematpur, H., Mahmood, S. M., Nasr, N. H., and Elraies, K. A., 2018, “Foam flow in porous media: Concepts, models, and challenges”, Journal of Natural Gas Science and Engineering, 53, pp. 163-180.

44. Mujeebu, M. A., Abdullah, M. Z., Bakar, M. A., Mohamad, A. A., Muhad, R. M. N., and Abdullah, M. K., 2009, “Combustion in porous media and its applications–A comprehensive survey”, Journal of Environmental Management, 90(8), pp. 2287-2312.

45. Sochi, T., 2010, “Non-newtonian flow in porous media”, Polymer, 51(22), pp. 5007-5023.

46. Greenkorn, R. A., 1981, “Steady flow through porous media”, AIChE Journal, 27(4), pp. 529-545.

47. Wang, C., Wang, R., Huo, Z., Xie, E., and Dahlke, H. E., 2020, “Colloid transport through soil and other porous media under transient flow conditions—A review”, Wiley Interdisciplinary Reviews: Water, 7(4), p. e1439.

48. Song, Y. Q., and Kausik, R., 2019, “NMR application in unconventional shale reservoirs–A new porous media research frontier”, Progress in Nuclear Magnetic Resonance Spectroscopy, 112, pp. 17-33.

49. Khanafer, K., and Vafai, K., 2019, “Applications of nanofluids in porous medium: A critical review”, Journal of Thermal Analysis and Calorimetry, 135, pp. 1479-1492.

50. Vafai, K., and Sozen, M., 1990, “Analysis of energy and momentum transport for fluid flow through a porous bed”, ASME Journal of Heat and Mass Transfer, 112, pp. 690-699.

51. Vadasz, P., 2007, “On the paradox of heat conduction in porous media subject to lack of local thermal equilibrium”, Journal of Heat and Mass Transfer, 50, pp. 4131-4140.

52. Stoner, R. J., and Maris, H. J., 1993, “Kapitza conductance and heat flow between solids at temperatures from 50 to 300 K”, Physical Review B, 48, p. 16373.

53. Intravaia, F., Behunin, R. O., Henkel, C., Busch, K., and Dalvit, D. A. R., 2016, “Failure of local thermal equilibrium in quantum friction”, Physical Review Letters, 117(10), p. 100402.

54. Minkowycz, W. J., Haji-Sheikh, A., and Vafai, K. F., 1999, “On departure from local thermal equilibrium in porous media due to a rapidly changing heat source: the Sparrow number”, Journal of Heat and Mass Transfer, 42, pp. 3373-3385.

55. Al-Sumaily, G. F., Al Ezzi, A., Dhahad, H. A., Thompson, M. C., and Yusaf, T., 2021, “Legitimacy of the local thermal equilibrium hypothesis in porous media: A comprehensive review”, Energies, 14(23), p. 8114.

56. Hwang, G. J., and Chao, C. H., 1994, “Heat transfer measurement and analysis for sintered porous channels”, Journal of Heat and Mass Transfer, 116, pp. 456-464.

57. Jiang, P. X., Li, M., Lu, T. J., Yu, L., and Ren, Z. P., 2004, “Experimental research on convection heat transfer in sintered porous plate channels”, Journal of Heat and Mass Transfer, 47, pp. 2085-2096.

58. Mahjoob, S., and Vafai, K., 2009, “Analytical characterization and production of an isothermal surface for biological and electronic applications”, ASME Journal of Heat and Mass Transfer, 131, p. 052604.

59. Hooman, K., and Merrikh, A. A., 2006, “Analytical solution of forced convection in a duct of rectangular cross-section saturated by a porous medium”, ASME Journal of Heat and Mass Transfer, 128, pp. 596-600.

60. Marafie, A., and Vafai, K., 2001, “Analysis of non-Darcian effects on temperature differentials in porous media”, Journal of Heat and Mass Transfer, 44, pp. 4401-4411.

61. Poulikakos, D., and Kazmierczak, M., 1987, “Forced convection in a duct partially filled with a porous material”, ASME Journal of Heat and Mass Transfer, 109, pp. 653-662.

62. Jang, J. Y., and Chen, J. L., 1992, “Forced convection in a parallel plate channel partially filled with a high porosity medium”, Journal of Heat and Mass Transfer, 19, pp. 263-273.

63. Vafai, K., and Thiyagaraja, R., 1987, “Analysis of flow and heat transfer at the interface region of a porous medium”, Journal of Heat and Mass Transfer, 30, pp. 1391-1405.

64. Mohamad, A. A., 2003, “Heat transfer enhancements in heat exchangers fitted with porous media Part I: constant wall temperature”, International Journal of Thermal Sciences, 42, pp. 385-395.

65. Huang, P. C., and Vafai, K., 1994, “Internal heat transfer augmentation in a channel using an alternate set of porous cavity-block obstacles”, Numerical Heat Transfer, Part A: Applications, 25, pp. 519-539.

66. Vafai, K., and Huang, P. C., 1994, “Analysis of heat transfer regulation and modification employing intermittently emplaced porous cavities”, ASME Journal of Heat and Mass Transfer, 116, pp. 604-613.

67. Alkam, M. K., Al-Nimr, M. A., and Hamdan, M. O., 2001, “Enhancing heat transfer in parallel-plate channels by using porous inserts”, Journal of Heat and Mass Transfer, 44, pp.931-938.

68. Chang, W. J., and Chang, W. L., 1996, “Mixed convection in a vertical parallel-plate channel partially filled with porous media of high permeability”, Journal of Heat and Mass Transfer, 39, pp. 1331-1342.

69. Shokouhmand, H., and Sayehvand, H. O., 2010, “Study of forced convection in a pipe partially filled with a porous medium”, Journal of Enhanced Heat Transfer, 17, pp. 205-221.

70. Mitrovic, J., and Maletic, B., 2007, “Heat transfer with laminar forced convection in a porous channel exposed to a thermal asymmetry”, Journal of Heat and Mass Transfer, 50, pp. 1106-1121.

71. Teamah, M. A., El-Maghlany, W. M., and Dawood, M. M. K., 2011, “Numerical simulation of laminar forced convection in horizontal pipe partially or completely filled with porous material”, International Journal of Thermal Sciences, 50, pp. 1512-1522.

72. Cekmer, O., Mobedi, M., Ozerdem, B., and Pop, I., 2012, “Fully developed forced convection in a parallel plate channel with a centered porous layer”, Transport in Porous Media, 93, pp. 179-201.

73. Repaka, R., and Satyamurty, V. V., 2010, “Local and average heat transfer in the thermally developing region of an asymmetrically heated channel”, Journal of Heat and Mass Transfer, 53, pp. 1654-1665.

74. Satyamurty, V. V., and Bhargavi, D., 2010, “Forced convection in thermally developing region of a channel partially filled with a porous material and optimal porous fraction”, International Journal of Thermal Sciences, 49, pp. 319-332.

75. Bhargavi, D., and Reddy, J. S. K., 2018, “Effect of heat transfer in the thermally developing region of the channel partially filled with a porous medium: constant wall heat flux”, International Journal of Thermal Sciences, 130, pp. 484-495.

76. Kuznetsov, A. V., 1996, “Analytical investigation of the fluid flow in the interface region between a porous medium and a clear fluid in channels partially filled with a porous medium”, Applied Scientific Research, 56, pp. 53-67.

77. Reddy, J. S. K., and Bhargavi, D., 2019, “Effect of axial conduction in the thermally developing region of the channel partially filled with a porous medium: constant wall heat flux”, International Journal of Advanced Trends in Computer Applications, 1, pp. 131-138.

78. Guo, Z., Kim, S. Y., and Sung, H. J., 1997, “Pulsating flow and heat transfer in a pipe partially filled with a porous medium”, Journal of Heat and Mass Transfer, 40, pp. 4209-4218.

79. Kuznetsov, A. V., and Xiong, M., 2000, “Numerical simulation of the effect of thermal dissipation on forced convection in a circular duct partially filled with Brinkman Forchheimer porous media”, International Journal for Numerical Methods in Fluids, 5, pp. 488-501.

80. Rudraiah, N., 1985, “Coupled parallel flows in a channel and a bounding porous medium of finite thickness”, Journal of Fluids Engineering, 107(3), pp. 322-329.

81. Phanikumar, M. S., and Mahajan, R. L., 2002, “Non-Darcy natural convection in high porosity metal foams”, Journal of Heat and Mass Transfer, 45, pp. 3781-3793.

82. Jiang, P. X., Ren, Z. P., Wang, B. X., and Wang, Z., 1996, “Forced convective heat transfer in a plate channel filled with solid particles”, Journal of Thermal Science, 5, pp. 43-53.

83. Alsabery, A. I., Mohebbi, R., Chamkha, A. J., and Hashim, I., 2019, “Effect of local thermal non-equilibrium model on natural convection in a nanofluid-filled wavy-walled porous cavity containing inner solid cylinder”, Chemical Engineering Science, 201, pp. 247-263.

84. Alhadhrami, A., Vishalakshi, C. S., Prasanna, B. M., Sreenivasa, B. R., Alzahrani, H. A., Gowda, R. P., and Kumar, R. N., 2021, “Numerical simulation of local thermal non-equilibrium effects on the flow and heat transfer of non-Newtonian Casson fluid in a porous media”, Case Studies in Thermal Engineering, 28, p. 101483.

85. Barman, P., and Srinivasa Rao, P., 2023, “Numerical analysis of local thermal non-equilibrium free convection in a porous enclosure with a wavy cold side wall”, Proceedings of the Institution of Mechanical Engineers, Part E: Journal of Process Mechanical Engineering, p. 09544089231154363.

86. Prasannakumara, B. C., 2022, “Assessment of the local thermal non-equilibrium condition for nanofluid flow through porous media: A comparative analysis”, Indian Journal of Physics, 96, pp. 2475-2483.

87. Xu, H., Xing, Z., and Vafai, K., 2019, “Analytical considerations of flow/thermal coupling of nanofluids in foam metals with local thermal non-equilibrium (LTNE) phenomena and inhomogeneous nanoparticle distribution”, Journal of Heat and Mass Transfer, 77, pp. 242-255.

88. Mansour, M. A., Ahmed, S. E., and Mahdy, A., 2023, “Entropy optimization and slant MHD mixed convection hybrid nanofluid flow within an oblique irregular lid-driven enclosure contains baffles: local thermal non-equilibrium model”, Arabian Journal for Science and Engineering, pp. 1-15.

89. Tayebi, T., and Chamkha, A. J., 2021, “Analysis of the effects of local thermal non-equilibrium (LTNE) on thermo-natural convection in an elliptical annular space separated by a nanofluid-saturated porous sleeve”, International Communications in Heat and Mass Transfer, 129, p. 105725.

90. Alsedais, N., Aly, A. M., and Mansour, M. A., 2022, “Local thermal non-equilibrium condition on mixed convection of a nanofluid-filled undulating cavity containing obstacle and saturated by porous media”, Ain Shams Engineering Journal, 13, p. 101562.

91. Rees, D. A. S., 2003, “Vertical free convective boundary-layer flow in a porous medium using a thermal non-equilibrium model: elliptical effects”, Journal of Applied Mathematics and Physics (ZAMP), 54, pp. 437-448.

92. Baytas, A. C., and Pop, I., 2002, “Free convection in a square porous cavity using a thermal non-equilibrium model”, International Journal of Thermal Sciences, 41, pp. 861-870.

93. Baytas, A. C., 2003, “Thermal non-equilibrium natural convection in a square enclosure filled with a heat-generating solid phase, non-Darcy porous medium”, International Journal of Energy Research, 27, pp. 975-988.

94. Saeid, N. H., 2004, “Analysis of mixed convection in a vertical porous layer using the non-equilibrium model”, Journal of Heat and Mass Transfer, 47, pp. 5619-5627.

95. Malashetty, M. S., Shivakumara, I. S., and Kulkarni, S., 2005, “The onset of Lapwood–Brinkman convection using a thermal non-equilibrium model”, Journal of Heat and Mass Transfer, 48, pp. 1155-1163.

96. Alazmi, B., and Vafai, K., 2002, “Constant wall heat flux boundary conditions in porous media under local thermal non-equilibrium conditions”, Journal of Heat and Mass Transfer, 45, pp. 3071-3087.

97. Yang, K., and Vafai, K., 2010, “Analysis of temperature gradient bifurcation in porous media–an exact solution”, Journal of Heat and Mass Transfer, 53, pp. 4316-4325.

98. Lee, D. Y., and Vafai, K., 1999, “Analytical characterization and conceptual assessment of solid and fluid temperature differentials in porous media”, Journal of Heat and Mass Transfer, 42, pp. 423-435.

99. Settar, A., Nebbali, R., Madani, B., and Abboudi, S., 2015, “Numerical investigation of convective heat transfer in a plane channel filled with metal foam under local thermal non-equilibrium”, Mechanics & Industry, 16, p. 504.

100. Haddad, O. M., Al-Nimr, M. A., and Al-Omary, J. S., 2007, “Forced convection of gaseous slip-flow in porous micro-channels under local thermal non-equilibrium conditions”, Transport in Porous Media, 67, pp. 453-471.

101. Buonomo, B., Manca, O., and Lauriat, G., 2014, “Forced convection in micro-channels filled with porous media in local thermal non-equilibrium conditions”, International Journal of Thermal Sciences, 77, pp. 206-222.

102. Buonomo, B., Cascetta, F., Lauriat, G., and Manca, O., 2018, “Convective heat transfer in thermally developing flow in micro-channels filled with porous media under local thermal non-equilibrium conditions”, Energy Procedia, 148, pp. 1058-1065.

103. Mahmoudi, Y., and Maerefat, M., 2011, “Analytical investigation of heat transfer enhancement in a channel partially filled with a porous material under local thermal non-equilibrium condition”, International Journal of Thermal Sciences, 50, pp. 2386-2401.

104. Karimi, N., Mahmoudi, Y., and Mazaheri, K., 2014, “Temperature fields in a channel partially filled with a porous material under local thermal non-equilibrium condition - An exact solution”, Proceedings of the Institution of Mechanical Engineers, Part C: Journal of Mechanical Engineering Science, 228, pp. 2778–2789.

105. Parhizi, M., Torabi, M., and Jain, A., 2021, “Local thermal non-equilibrium (LTNE) model for developed flow in porous media with spatially-varying Biot number”, Journal of Heat and Mass Transfer, 164, p. 120538.

106. Krishnan, G., Parhizi, M., Torabi, M., and Jain, A., 2022, “Local thermal non-equilibrium (LTNE) modeling of a partially porous channel with spatial variation in Biot number”, ASME Journal of Heat and Mass Transfer, 144, p. 062701.

107. Fathi-Kelestani, A., Nazari, M., and Mahmoudi, Y., 2021, “Pulsating flow in a channel filled with a porous medium under local thermal non-equilibrium condition: an exact solution”, Journal of Thermal Analysis and Calorimetry, 145, pp. 2753-2775.

108. Li, Q., Zhang, R., and Hu, P., 2021, “Effect of thermal boundary conditions on forced convection under LTNE model with no-slip porous-fluid interface condition”, Journal of Heat and Mass Transfer, 167, p. 120803.

109. Hu, P., and Li, Q., 2020, “Effect of heat source on forced convection in a partially-filled porous channel under LTNE condition”, International Communications in Heat and Mass Transfer, 114, p. 104578.

110. Ouyang, X. L., Vafai, K., and Jiang, P. X., 2013, “Analysis of thermally developing flow in porous media under local thermal non-equilibrium conditions”, Journal of Heat and Mass Transfer, 67, pp. 768-775.

111. Li, Q., and Hu, P., 2019, “Analytical solutions of fluid flow and heat transfer in a partial porous channel with stress jump and continuity interface conditions using LTNE model”, Journal of Heat and Mass Transfer, 128, pp. 1280-1295.

112. Dehghan, M., 2015, “Effects of heat generations on the thermal response of channels partially filled with non-Darcian porous materials”, Transport in Porous Media, 110, pp. 461-482.

113. Dehghan, M., Valipour, M. S., Keshmiri, A., Saedodin, S., and Shokri, N., 2016, “On the thermally developing forced convection through a porous material under the local thermal non-equilibrium condition: an analytical study”, Journal of Heat and Mass Transfer, 92, pp. 815-823.

114. Xu, H. J., Qu, Z. G., Lu, T. J., He, Y. L., and Tao, W. Q., 2011. “Thermal modeling of forced convection in a parallel-plate channel partially filled with metallic foams”, Journal of Heat Transfer, 133, p. 092603.

115. Yi, Y., Bai, X., Kuwahara, F., and Nakayama, A., 2021, “A local thermal non-equilibrium solution based on the Brinkman–Forchheimer-extended Darcy model for thermally and hydrodynamically fully developed flow in a channel filled with a porous medium. Transport in Porous Media, 139, pp. 67-88.

116. Mahmoudi, Y., 2014, “Effect of thermal radiation on temperature differential in a porous medium under local thermal non-equilibrium condition”, Journal of Heat and Mass Transfer, 76, pp. 105-121.

117. Torabi, M., Karimi, N., Zhang, K., and Peterson, G.P., 2016, “Generation of entropy and forced convection of heat in a conduit partially filled with porous media–local thermal non-equilibrium and exothermicity effects”, Applied Thermal Engineering, 106, pp. 518-536.

118. Dukhan, N., and Hooman, K., 2013, “Comments on two analyses of thermal non-equilibrium Darcy–Brinkman convection in cylindrical porous media”, Journal of Heat and Mass Transfer, 66, pp. 440-443.

119. Elliott, A., Torabi, M., Karimi, N., and Cunningham, S., 2016, “On the effects of internal heat sources upon forced convection in porous channels with asymmetric thick walls”, International Communications in Heat and Mass Transfer, 73, pp. 100-110.

120. Karimi, N., Agbo, D., Khan, A. T., and Younger, P. L., 2015, “On the effects of exothermicity and endothermicity upon the temperature fields in a partially-filled porous channel”, International Journal of Thermal Sciences, 96, pp. 128-148.

121. Dehghan, M., Valipour, M.S., Saedodin, S., and Mahmoudi, Y., 2016, “Investigation of forced convection through entrance region of a porous-filled microchannel: an analytical study based on the scale analysis”, Applied Thermal Engineering, 99, pp. 446-454.

122. Tajik Jamal-Abad, M., 2016, “Analytical investigation of forced convection in thermally developed region of a channel partially filled with an asymmetric porous material-LTNE model”, International Journal of Engineering, 29, pp. 975-984.

123. Forooghi, P., Abkar, M., and Saffar-Avval, M., 2011, “Steady and unsteady heat transfer in a channel partially filled with porous media under thermal non-equilibrium condition”, Transport in Porous Media, 86, pp. 177-198.

124. Abkar, M., Forooghi, P., and Abbassi, A., 2011, “Assessment of thermal non-equilibrium condition on heat transfer through a channel lined with porous media–constant wall temperature”, Defect and Diffusion Forum, 312, pp. 33-38.

125. Baig, M. F., Chen, G. M., Tso, C. P., and Kueh, T. C., 2023, “Effects of porous medium filling on thermally developing forced convection in a parallel plate channel” International Journal of Thermofluids, 20, p. 100430.

126. Dehghan, M., Valipour, M.S., and Saedodin, S., 2014, “Perturbation analysis of the local thermal non-equilibrium condition in a fluid-saturated porous medium bounded by an iso-thermal channel”, Transport in Porous Media, 102, pp. 139-152.

127. Yang, C., Ando, K., and Nakayama, A., 2011, “A local thermal non-equilibrium analysis of fully developed forced convective flow in a tube filled with a porous medium”, Transport in Porous Media, 89, pp. 237-249.

128. Abdedou, A., and Bouhadef, K., 2015, “Comparison between two local thermal non-equilibrium criteria in forced convection through a porous channel”, Journal of Applied Fluid Mechanics, 8, pp. 491-498.

129. Dehghan, M., Jamal-Abad, M. T., and Rashidi, S., 2014, “Analytical interpretation of the local thermal non-equilibrium condition of porous media imbedded in tube heat exchangers”, Energy Conversion and Management, 85, pp. 264-271.

130. Seetharamu, K. N., Leela, V., and Kotloni, N., 2017, “Numerical investigation of heat transfer in a micro-porous-channel under variable wall heat flux and variable wall temperature boundary conditions using local thermal non-equilibrium model with internal heat generation”, Journal of Heat and Mass Transfer, 112, pp. 201-215.

131. Mahmoudi, Y., and Karimi, N., 2014, “Numerical investigation of heat transfer enhancement in a pipe partially filled with a porous material under local thermal non-equilibrium condition”, Journal of Heat and Mass Transfer, 68, pp. 161-173.

132. Yang, C., Kuwahara, F., Liu, W., and Nakayama, A., 2011, “Thermal non-equilibrium forced convective flow in an annulus filled with a porous medium”, Open Transport Phenomena Journal, 3, pp. 31-39.

133. Xu, H. J., Qu, Z. G., and Tao, W. Q., 2011, “Analytical solution of forced convective heat transfer in tubes partially filled with metallic foam using the two-equation model”, Journal of Heat and Mass Transfer, 54, pp. 3846-3855.

134. Xu, Z. G., Qin, J., Zhou, X., and Xu, H. J., 2018, “Forced convective heat transfer of tubes sintered with partially-filled gradient metal foams (GMFs) considering local thermal non-equilibrium effect”, Applied Thermal Engineering, 137, pp. 101-111.

135. Xu, H. J., Zhao, C. Y., and Xu, Z. G., 2016, “Analytical considerations of slip flow and heat transfer through micro foams in mini/microchannels with asymmetric wall heat fluxes”, Applied Thermal Engineering, 93, pp. 15-26.

136. Yang, K., Huang, W., Li, X., and Wang, J., 2020, “Analytical analysis of heat transfer and entropy generation in a tube filled with double-layer porous media”, Entropy, 22, p. 1214.

137. Schlichting, H., and Gersten, K., 2007, “Boundary layer theory”, Springer-Verlag.

138. Al-Hadhrami, A. K., Elliott, L., and Ingham, D. B., 2002, “Combined free and forced convection channels of porous media”, Transp. Porous Med, 49, pp. 265-289.

139. Al-Hadhrami, A. K., Elliott, L., and Ingham, D. B., 2003, “A new model for viscous dissipation in porous media across a range of permeability values”, Transp. Porous Med, 53, pp. 117-122.

140. Nield, D. A., 2006, “A note on a Brinkman-Brinkman forced convection problem,” Trans. Porous Media, 64, pp. 185-188.

141. Nield, D. A., Barletta, A., and Celli, M., 2011, “The effect of viscous dissipation on the onset of convection in an inclined porous layer”, Journal of Fluid Mechanics, 679, pp. 544-558.

142. Tso, C. P., Sheela-Francisca, J., and Hung, Y. M., 2010, “Viscous dissipation effects of power-law fluid flow within parallel plates with constant heat fluxes”, Journal of Non-Newtonian Fluid Mechanics, 165(11-12), pp. 625-630.

143. Nakayama, A., and Shenoy, A. V., 1993, “Non-darcy forced convective heat transfer in a channel embedded in a non-Newtonian inelastic fluid-saturated porous medium”, The Canadian Journal of Chemical Engineering, 71(1), pp. 168-173.

144. Baig, M. F., Chen, G. M., and Tso, C. P., 2022, “Viscous dissipative forced convection in a channel partially filled with porous medium”, Journal of Thermophysics and Heat Transfer, 36(2), pp. 276-290.

145. Buonomo, B., Manca, O., and Lauriat, G., 2016, “Forced convection in porous microchannels with viscous dissipation in local thermal non-equilibrium conditions”, International Communications in Heat and Mass Transfer, 76, pp. 46-54.

146. Hooman, K., and Gurgenci, H., 2007, “Effects of viscous dissipation and boundary conditions on forced convection in a channel occupied by a saturated porous medium”, Transport in Porous Media, 68, pp. 301-319.

147. Nield, D. A., Kuznetsov, A. V., and Xiong, M., 2004, “Effects of viscous dissipation and flow work on forced convection in a channel filled by a saturated porous medium”, Transport in Porous Media, 56, pp. 351-367.

148. Mahmud, S., and Fraser, R. A., 2005, “Flow, thermal, and entropy generation characteristics inside a porous channel with viscous dissipation”, International Journal of Thermal Sciences, 44(1), pp. 21-32.

149. Hung, Y. M., and Tso, C. P., 2009, “Effects of viscous dissipation on fully developed forced convection in porous media”, International Communications in Heat and Mass Transfer, 36(6), pp. 597-603.

150. Bhargavi, D., and Reddy, J. S. K., 2019, “Analytical investigation of laminar forced convection with viscous dissipation in parallel plate channels partially filled with porous material: constant wall heat flux”, Journal of Nanofluids, 8(1), pp. 238-251.

151. Repaka, R., and Satyamurty, V. V., 2013, “Effect of viscous dissipation on forced convection heat transfer in parallel plate channels with asymmetric boundary conditions”, In ASME International Mechanical Engineering Congress and Exposition (Vol. 56369, p. V08CT09A047). American Society of Mechanical Engineers.

152. Murthy, P. V. S. N., 1998, “Thermal dispersion and viscous dissipation effects on non-Darcy mixed convection in a fluid saturated porous medium”, Heat and Mass Transfer, 33(4), pp. 295-300.

153. Rees, D. A. S., Magyari, E., and Keller, B., 2003, “The development of the asymptotic viscous dissipation profile in a vertical free convective boundary layer flow in a porous medium”, Transport in Porous Media, 53, pp. 347-355.

154. Ingham, D. B., Pop, I., and Cheng, P., 1990, “Combined free and forced convection in a porous medium between two vertical walls with viscous dissipation”, Transport in porous media, 5, pp. 381-398.

155. Tashtoush, B., 2000, “Analytical solution for the effect of viscous dissipation on mixed convection in saturated porous media”, Transport in porous media, 41, pp. 197-209.

156. Ajibade, A. O., Jha, B. K., and Gambo, J. J., 2022, “Combined effects of viscous and Darcy dissipation on mixed convection flow in a composite vertical channel partially filled with a porous material: Analytical approach”, International Communications in Heat and Mass Transfer, 136, p. 106197.

157. Ajibade, A. O., Gambo, J. J., and Jha, B. K., 2023, “Effects of viscous and darcy dissipation on fully developed natural convection flow in a composite channel partially filled with porous material: Homotopy perturbation method (HPM)”, ZAMM-Journal of Applied Mathematics and Mechanics/Zeitschrift für Angewandte Mathematik und Mechanik, p. e202100583.

158. Nield, D. A., Kuznetsov, A. V., and Xiong, M., 2003, “Thermally developing forced convection in a porous medium: parallel plate channel with walls at uniform temperature, with axial conduction and viscous dissipation effects”, International Journal of Heat and Mass Transfer, 46(4), pp. 643-651.

159. Hooman, K., Pourshaghaghy, A. and Ejlali, A., 2006, “Effects of viscous dissipation on thermally developing forced convection in a porous saturated circular tube with an isoflux wall”, Applied Mathematics and Mechanics, 27, pp. 617-626.

160. Barletta, A., 1998, “Laminar mixed convection with viscous dissipation in a vertical channel”, International Journal of Heat and Mass Transfer, 41(22), pp. 3501-3513.

161. Barletta, A., and Zanchini, E., 2001, “Mixed convection with viscous dissipation in an inclined channel with prescribed wall temperatures”, International journal of heat and mass transfer, 44(22), pp. 4267-4275.

162. Aydin, O., and Avic, M., 2006, “Laminar forced convection with viscous dissipation in a Couette–Poiseuille flow between parallel plates”, Applied energy, 83(8), pp. 856-867.

163. Chen, G. M., Lim, B. K., and Tso, C. P., 2019, “Thermal viscous dissipative Couette-Poiseuille flow in a porous medium saturated channel”, Symmetry, 11(7), p. 869.

164. Bhargavi, D., and Reddy, J. S. K., 2019, “Effect of viscous dissipation and axial conduction in thermally developing region of the channel partially filled with a porous material subjected to constant wall heat flux”, International Journal of Mechanical and Mechatronics Engineering, 13(12), pp. 761-772.

165. Chen, G. M., and Tso, C. P., 2011, “A two-equation model for thermally developing forced convection in porous medium with viscous dissipation”, International Journal of Heat and Mass Transfer, 54(25-26), pp. 5406-5414.

166. Chen, G. M., and Tso, C. P., 2011, “Forced convection with viscous dissipation using a two-equation model in a channel filled by a porous medium”, International Journal of Heat and Mass Transfer, 54(9-10), pp. 1791-1804.

167. Buonomo, B., Manca, O., and Lauriat, G., 2014, “Viscous dissipation on heat transfer in microchannels filled with porous media under local thermal non-equilibrium conditions”, In 4th European Conference on Microfluidics.

168. Torabi, M., Zhang, K., Yang, G., Wang, J., and Wu, P., 2015, “Heat transfer and entropy generation analyses in a channel partially filled with porous media using local thermal non-equilibrium model”, Energy, 82, pp. 922-938.

169. Yang, X., and Liu, X. M., 2006, “Temperature profiles of local thermal nonequilibrium for thermal developing forced convection in porous medium parallel plate channel”, Applied Mathematics and Mechanics, 27(8), pp. 1123-1131.

170. Torabi, M., and Peterson, G. P., 2016, “Effects of velocity slip and temperature jump on the heat transfer and entropy generation in micro porous channels under magnetic field”, International Journal of Heat and Mass Transfer, 102, pp. 585-595.

171. Chee, Y. S., Ting, T. W., and Hung, Y. M., 2015, “Entropy generation of viscous dissipative flow in thermal non-equilibrium porous media with thermal asymmetries”, Energy, 89, pp. 382-401.

172. Ting, T. W., Hung, Y. M., and Guo, N., 2015, “Entropy generation of viscous dissipative nanofluid flow in thermal non-equilibrium porous media embedded in microchannels”, International Journal of Heat and Mass Transfer, 81, pp. 862-877.

173. Hunt, G., Karimi, N., and Torabi, M., 2018, “Two-dimensional analytical investigation of coupled heat and mass transfer and entropy generation in a porous, catalytic microreactor”, International Journal of Heat and Mass Transfer, 119, pp. 372-391.

174. Chen, G. M., and Tso, C. P., 2021, “Viscous dissipation effect on CuO-Water nanofluid-cooled microchannel heat sinks”, Case Studies in Thermal Engineering, 26, p. 101159.

175. Loh, A. K. W., Chen, G. M., and Lim, B. K., 2022, “Viscous dissipation effect on forced convective transport of nanofluids in an asymmetrically heated parallel-plate microchannel”, Case Studies in Thermal Engineering, 35, p. 102056.

176. Leela, V., Seetharamu, K. N., Kotloni, N., and Reddy, R. G., 2020, “Effect of asymmetrical wall heat flux and wall temperature ratio on mixed convection in a vertical micro-porous-channel with internal heat generation”, Propulsion and Power Research, 9(4), pp. 394-407.

177. Torabi, M., and Zhang, K., 2015, “Temperature distribution, local and total entropy generation analyses in MHD porous channels with thick walls”, Energy, 87, pp.540-554.

178. Jiang, P. X., Ren, Z. P., and Wang, B. X., 1999, "Numerical simulation of forced convection heat transfer in porous plate channels using thermal equilibrium and nonthermal equilibrium models", Numerical Heat Transfer. Part A, Applications, 35(1), pp. 99-113.

179. Raju, K. V. S., Sudhakar Reddy, T., Raju, M. C., Satya Narayana, P. V., and Venkataramana, S., 2014, "MHD convective flow through porous medium in a horizontal channel with insulated and impermeable bottom wall in the presence of viscous dissipation and joule heating", Ain Shams Engineering Journal, 5, pp.543–551.

180. Sharmilla, K., and Saranya, S., 2017, "Effect of magnetic field in a forced convective saturated porous duct", International Journal for Research in Emerging Science and Technology, 4.

181. Kurzweg, U. H., 1963, "The stability of Couette flow in the presence of an axial magnetic field", Journal of Fluid Mechanics, vol 17, pp. 52–60.

182. Gulab, R., and Mishra, R., 1977, "Unsteady flow through magnetohydrodynamic porous media", Indian Journal of Pure and Applied Mathematics, vol 8, pp.637, 1977.

183. Raptis, A. A., and Kafousias, N., 1982, "Heat transfer in flow through a porous medium bounded by on an infinite vertical plate under the action of a magnetic field", International Journal of Energy Research, 6, pp. 241–245.

184. Raptis, A. A., and Perdikis, C. P., 1988, "Combined free and forced convection flow through a porous medium", International Journal of Energy Research, 12, pp. 557–560.

185. Agarwal, M., Joseph, V., Yadav, R., and Saxena, P., 2016, "Investigation of magneto hydrodynamic flow in a channel with porous bounding wall", Special Topics & Reviews in Porous Media-An International Journal, 7, pp. 281-291.

186. Verma, V. K., and Gupta, A.K., 2017, "Analytical solution of the flow in a composite cylindrical channel partially filled with porous medium in the effect of magnetic field", Special Topics & Reviews in Porous Media-An International Journal, 8, pp. 39-48.

187. Baoku, I. G., Cookey, C. I., and Olajuwon, B.I., 2010, "Magnetic field and thermal radiation effects on steady hydromagnetic Couette flow through a porous channel", Surveys in Mathematics and its Applications, 5, pp. 215-228.

188. Ashish, T., Satya, D. and Filippov, A., 2012, "Effect of the magnetic field on the hydrodynamic permeability of a membrane", Colloid Journal, 74, pp. 515– 522.

189. Ghofrani, A., Dibaei M. H., Hakim Sima A., and Shafii M. B., 2013, "Experimental investigation on laminar forced convection heat transfer of ferro fluids under an

alternating magnetic field", Experimental Thermal and Fluid Science, 49, pp.193–200.

190. Sheikholeslami, M., Rashidi, M. M. and Ganji, D. D., 2015, "Numerical investigation of magnetic nano fluid forced convective heat transfer in existence of variable magnetic field using two phase model", Journal of Molecular Liquids, 212, pp.117–126.

191. Takhar, H. S., and Beg, O. A., 1997, "Effects of transverse magnetic field, Prandtl number and Reynolds number on non-Darcy mixed convective flow of an incompressible viscous fluid past a porous vertical flat plate in a saturated porous medium", International Journal of Energy Research, 21, pp. 87-100.

192. Barletta, A., Lazzari, S., Magyari, E., and Pop, I., 2008, "Mixed convection with heating effects in a vertical porous annulus with radially varying magnetic field", International Journal of Heat and Mass Transfer, 51, pp. 5777-5784.

193. Komurgoz, G., Arikoglu, A., and Ozkol, I., 2012, "Analysis of the magnetic effect on entropy generation in an inclined channel partially filled with a porous medium", Numerical Heat Transfer, Part A: Applications, 61, pp. 786-799.

194. Abdel-Gaied, S.M., 2013, "Effect of magnetic field on flow in a porous medium over a permeable stretching wall in the presence of thermal radiation and suction/injection", IOSR Journal of Mathematics (IOSR-JM), 7, pp. 68-73.

195. Srivastava, B. G., and Satya Deo., 2013, "Effect of magnetic field on the viscous fluid flow in a channel filled with porous medium of variable permeability", Applied Mathematics and Computation, 219, pp. 8959–8964.

196. Jhankal, A. K., Jat, R. N., and Deepak Kumar., 2017, "Magnetohydrodynamics (MHD) forced convective flow and heat transfer over a porous plate in a Darcy-Forchheimer porous medium in presence of radiation", International Journal of Current Research, 9, pp. 16- 23.

197. Habchi, S., and Acharya, S., 1986, "Laminar mixed convection in a symmetrically or asymmetrically heated vertical channel", Numerical Heat Transfer, 9, pp. 605-618.

198. Naito, E., and Nagano, Y., 1989, "Combined forced and free upward-flow convection in the entrance region between inclined parallel plates", ASME Journal of Heat Transfer, 111, pp. 675-682.

199. Nguyen, T. V., 1992, "Laminar heat transfer for thermally developing flow inducts", International Journal of Heat and Mass Transfer, 35, No. 7, pp. 1733-1741.

200. Peaceman, D. W., and Rachford, H. H., 1955, "The numerical solution of parabolic and elliptic differential equations", Journal of the Society for Industrial and Applied Mathematics, 3, pp. 28-41.

201. Douglas Jr. J., 1955, "On the numerical integration of $\partial^2u/\partial x^2 + \partial^2u/\partial y^2 = \partial u/\partial t$ by implicit methods", Journal of the Society for Industrial and Applied Mathematics, 3, pp. 42-65.

202. Leonard, B. P., 1979, "A stable and accurate modeling procedure based on quadratic interpolation", Computer Methods in Applied Mechanics and Engineering, 19, pp. 58-98.

203. Jeng, Y. N., Chen, J. L., and Aung, W., 1992, "On the Reynolds-number independence of mixed convection in a vertical channel subjected to asymmetric wall temperatures with and without flow reversal", International Journal of Heat and Fluid Flow," 13, pp. 329-339.

204. Krishnan, K. N., and Sastri, V. M. K., 1978, "Numerical solution of thermal entry length problem with variable viscosities and viscous dissipation", Heat and Mass Transfer, 11, pp. 73-79.

205. Min, T., Choi, H. Y., Yoo, J. Y., and Choi, H., 1997, "Laminar convective heat transfer of a Bingham plastic in a circular pipe-ii: numerical approach-hydrodynamically developing flow and simultaneously developing flow", International Journal of Heat and Mass Transfer, 40, pp. 3689-3701.

206. Lew, H. C., 1968, "Method of accelerated successive replacement applied to boundary layer equations", AIAA Journal, 6, pp. 929-931.

207. Lieberstain, H. M., 1968, A Course in Numerical Analysis, Harper and Row, New York.

208. Dellinger, T. C., 1971, "Computations on non-equilibrium merged shock layer by successive accelerated replacement scheme", AIAA Journal, 9, pp. 262-269.

209. Satyamurty, V. V., 1984, "Successive accelerated replacement scheme applied to study of natural convection heat transfer in porous cryogenic insulations", ASME pp. 85-WA/HT-37.

210. Satyamurty, V. V. and Marpu, D. R., 1988 "Relative effects of variable fluid properties and non-Darcy flow on convection in porous media", ASME HTD-96, pp. 613-621.

211. Marpu, D. R., and Satyamurty, V. V., 1989, "Influence of variable fluid density on free convection in rectangular porous media", ASME Journal of Energy Resources Technology, 111, pp. 214-220.

212. Satyamurty, V. V., and Marpu, D. R., 1989, "Influence of linear and non-linear variation of viscosity on free convection in liquid filled rectangular porous slabs", Chemical Engineering Communications, 88, pp. 173-185.

213. Marpu, D. R., and Satyamurty, V. V., 1991, "Investigation on the validity of boussinesq approximation on free convection in vertical porous annulus", Warme- und Stoffubertragung, 26, pp. 141-147.

214. Marpu, D. R., 1990, “Studies on fluid property variation and non-darcy flow on free and forced convection in porous media”, Ph.D. Thesis, IIT Kharagpur, India.

215. Sharma, R. V., 1998, “Studies on influence of fluid density variation and non-Darcy flow on natural convection in a porous box”, Ph.D. Thesis, IIT Kharagpur, India.

216. Prakash Chandra, 2004, “Studies on convection heat transfer in fluid filled saturated anisotropic rectangular porous slab”, Ph.D. Thesis, IIT Kharagpur, India.

217. Reddy, J. S. K., and Bhargavi, D., 2018, “Numerical study of fluid flow in a channel partially filled with porous medium with Darcy− Brinkman− Forchheimer equation”, Special Topics & Reviews in Porous Media: An International Journal, 9(4), pp. 301-312.

218. Jagadeesh Kumar, M., and Satyamurty, V. V., 2015, “Effect of entry temperature on forced convection heat transfer with viscous dissipation in thermally developing region of concentric annuli”, ASME Journal of Heat Transfer, 137, pp. 121001(1-8).

219. Jiang, P. X., Xu, R., and Li, M., 2004, “Experimental investigation of convection heat transfer in mini-fin structures and sintered porous media”, Journal of Enhanced Heat Transfer, 11(4), pp. 391-406.

Appendix

$$A_1 = 1 + DaM^2$$

$$A_2 = \sqrt{\varepsilon A_1 / Da}$$

$$A_3 = 1 + \mathrm{e}^{\sqrt{2\kappa Bi}}$$

$$A_4 = \left(\kappa Bi - A_2{}^2\right)$$

$$A_5 = Sech\left[\frac{A_2}{2}\right]$$

$$A_6 = 1 + \cosh\left[A_2\right]$$

$$A_7 = \left(A_2 - 2A_{10}\right)$$

$$A_8 = \cosh\left[\sqrt{\frac{\kappa Bi}{2}}\right]$$

$$A_9 = \sinh\left[\sqrt{\frac{\kappa Bi}{2}}\right]$$

$$A_{10} = A_3 \tanh\left[\frac{A_2}{2}\right]$$

$$A_{11} = -\left(2\kappa BiDa - \varepsilon A_1\right)$$

$$A_{12} = -\left(2\kappa BiDa - 3\varepsilon A_1\right)$$

$$A_{13} = \sqrt{2}\varepsilon A_1 A_9 + \sqrt{\kappa Bi}\, A_8 A_{11}$$

$$A_{14} = -96\left(\kappa BiDa\right)^3 + 4\left(\kappa BiDa\right)^2\left(30 + \kappa Bi\right)A_1\varepsilon$$

$$A_{15} = 10\left(\kappa BiDa\right)^2 - 13\kappa\varepsilon BiDaA_1 + 5\varepsilon^2 A_1{}^2$$

$$A_{16} = \frac{2e^{\sqrt{\frac{\kappa Bi}{2}}}\sqrt{\kappa A_1}A_{13}}{Da^{3/2}}$$

$$A_{17} = \left(6 + \kappa Bi\right)A_1\varepsilon - 24\kappa BiDa$$

$$A_{18} = \kappa Bi\sqrt{\varepsilon DaA_1}\left(2e^{\sqrt{2\kappa Bi}} + A_6 A_5^2\right)$$

List of Published Papers

1. N. Gupta, and D. Bhargavi, “Study of influence of local thermal non-equilibrium in developing thermal field in a porous-filled duct: constant wall heat flux”, Special Topics and Reviews in Porous Media: International Journal - Begell house, 13(5), pp. 49-81, 2023.
2. N. Gupta, and D. Bhargavi, “Effect of magnetic field on the developing thermal field in a duct filled with porous media under local thermal non-equilibrium with a nonlinear flow model”, Journal of Advance Research in Fluid Mechanics and Thermal Sciences, 103(1), pp.87-104, 2023.
3. D. Bhargavi, N. Gupta, and O. D. Makinde, “A numerical study of axial conduction in a fluid-saturated porous-filled duct under a local thermal non-equilibrium model”, Special Topics and Reviews in Porous Media: International Journal - Begell house, 14(3), pp. 73–89, 2023.
4. N. Gupta, and D. Bhargavi, “Effect of magnetic field on Couette flow in a fluid-saturated porous-filled duct under the local thermal non-equilibrium with viscous dissipation”, Advances in Mechanical Engineering and Material Science, Publisher: Springer, pp 57–68, 2023.

List of Communicated Papers

5. N. Gupta, and D. Bhargavi, “Computational study of viscous dissipation effect on the developing thermal field under the local thermal non-equilibrium (LTNE) model in a fluid-saturated porous-filled duct”, Journal of Porous Media
6. N. Gupta and D. Bhargavi, “Synergistic impact of axial conduction and viscous dissipation at the entrance region under the local thermal non-equilibrium (LTNE) framework in a duct packed with saturated porous medium”, Numerical Heat Transfer, Part B: Fundamentals.
7. D. Bhargavi, N. Gupta, and P. A. L. Narayana, “A numerical study of the effect of magnetic field in the entrance region of a Couette flow in a duct filled with porous material under the local thermal non-equilibrium”, Journal of Engineering Mathematics.

Note: 4 and 7 are not part of the thesis.